Luminescence Properties of Ce^{3+}, Pr^{3+} and Nd^{3+} Activated Scintillators for Positron Emission Tomography (PET)

Luminescence Properties of Ce^{3+}, Pr^{3+} and Nd^{3+} Activated Scintillators for Positron Emission Tomography (PET)

Luminescentie-eigenschappen van Ce^{3+}, Pr^{3+} en Nd^{3+} geactiveerde scintillatoren voor Positron Emissie Tomografie (PET)

(met een samenvatting in het Nederlands)

Własności luminescencyjne scyntylatorów aktywowanych Ce^{3+}, Pr^{3+} i Nd^{3+} do zastosowania w Pozytonowej Tomografii Komputerowj (PET)

(ze streszczeniem po polsku)

Proefschrift

ter verkrijging van de graad van doctor aan de Universiteit Utrecht op gezag van de rector magnificus, prof.dr. G.J. van der Zwaan, ingevolge het besluit van het college voor promoties in het openbaar te verdedigen op woensdag 16 november 2011 des ochtends te 10.30 uur

door

Aleksander Karol Zych

geboren op 13 maart 1983, te *Wrocław, Polen*

Promotor: Prof. dr. A. Meijerink

Co-promotor: Dr. C. de Mello Donegá

Work presented in this thesis was made possible by the financial support from the EU String project (NMP3-CT-2006-032636).

Cover design by: Aleksander Karol Zych. $Gd_2O_2S:Pr^{3+}$ ($GOS:Pr^{3+}$) ceramic scintillators uder a 366 nm excitation.

ISBN 978-90-393-5602-9

Aan onze Kinderen

Table of Contents

1

Introduction

ABSTRACT

In this chapter an introduction is given to the fascinating world of scintillation and scintillator materials used in medical imaging. A short history of medical imaging and the role of scintillator materials in various techniques are presented as background and motivation for the research described in this thesis. The technique of Positron Emission Tomography (PET) is explained in more detail, since scintillator materials for this medical imaging technique are the focus of this work. Most scintillator materials rely on luminescence from lanthanide ions. A background on lanthanide ions is provided, including the history of their discovery and an introduction to the basics of the luminescence properties of lanthanides. The last part of the introduction gives insight into the experimental station at the DESY synchrotron which was crucial for the work described in this thesis. Finally a short overview of the main results and conclusions of the various chapters of this thesis is given.

1.1 A BRIEF HISTORY OF MEDICAL IMAGING

Since the early days of humanity the desire to improve the quality of life has been an important driving force behind efforts to obtain a better understanding through exploration, i.e. research. An important part of a better life has always been a longer life. The desire to lengthen the life span is closely connected to research in the field of health care. Already in ancient times when the concept of disease was introduced by the Greek physician Hippocrates around 400 B.C., knowledge of medicine was impressive. The understanding of the causes of disease was however limited as was the ability to detect disease in an early stage when cure can be more effective. Nowadays the understanding of diseases has improved dramatically, but still the further development of techniques for the early detection of diseases is very important. Especially in the present society with an aging population due to the better living conditions and improved health care, the longer life expectancy poses new challenges on health care and diagnostics. Health issues related to cancer and cardiovascular diseases have become more important and require new schemes for early detection and cure as well as strategies to prevent these diseases.

FIG. 1.1. Wilhelm Conrad Röntgen. After his discovery of X-rays he is considered the father of medical radiography.

Early diagnosis of disease became possible with the development of medical imaging techniques. The most important imaging techniques rely on high energy radiation and use the phenomenon of scintillation, i.e. the generation of light under irradiation with ionizing radiation or particles. A landmark in the history of imaging with radiation is discovery of X-rays in 1895 by Wilhelm Conrad Röntgen (FIG. 1.1). For his discovery of a new type of radiation, which he called X-radiation or X-rays and is known *Röntgenstraling* in Dutch, he received the Nobel Prize in physics in 1901. He published his findings in a series of papers between 1895 and 1897 [1]. He observed that a barium platinocyanide screen glowed when exposed to X-rays and that a dense object (zinc foil) between the chemical and the X-ray source casted a shadow on the screen. It took only three weeks after the remarkable discovery before it was applied for medical imaging of broken bones of patients. Röntgen himself proudly presented in one his papers the well-known X-ray photograph of the hand of his wife in which the bone structure and wedding ring can be discerned (FIG. 1.2) [2].

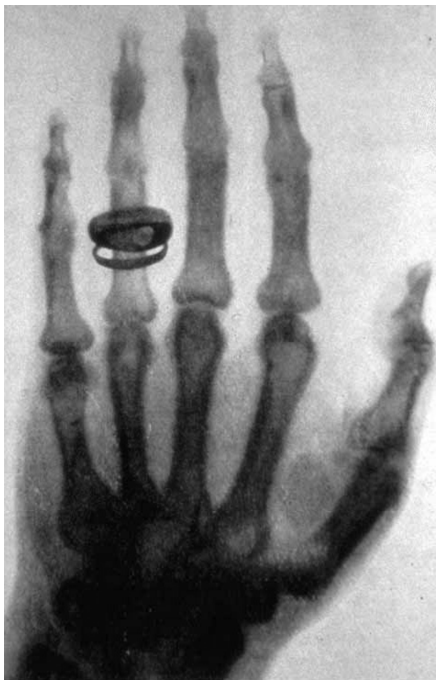

FIG. 1.2. One of the first X-ray photographs of the hand of the wife of Röntgen, Anna Bertha Ludwig.

Since the start of medical imaging using ionizing radiation or radiography in 1895, research in this area has intensified and it continues until today. In the early days of radiography there was no knowledge on the harmful effects of ionizing radiation on living organisms. This led to overexposure to X-rays of both patients and doctors leading to post-radiation diseases. FIGURE 1.3 shows a typical example of an early radiography practice where no precautions were taken to limit exposure to the harmful X-rays.

The discovery of the new radiation with high penetration depth through soft tissue led to the development of non-medical applications as well. In the US special underwear was sold to people who were concerned about what the new machines might see through clothing [1]. The new radiation was also used in shoe stores in specially designed fitting machines [3]. The picture of the foot in the contours of the shoe could be studied using the shoe fitting fluoroscope to help select the best fitting shoes (FIG. 1.4). The harmful effects of X-ray irradiation were not recognized and shoe fitting fluoroscopes were in use as late as the 1950´s [3].

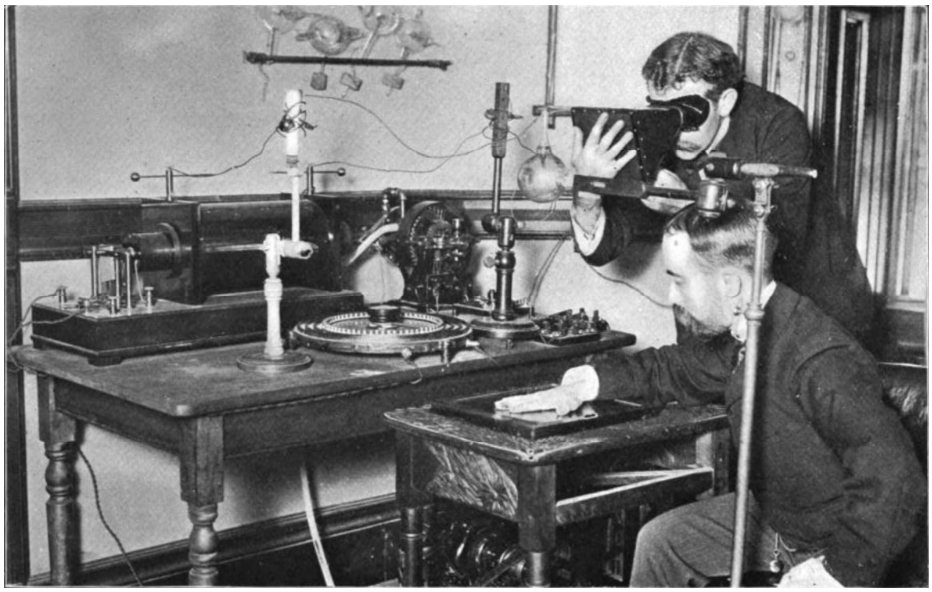

FIG. 1.3. An example of early-days radiography using X-rays. No precautions were taken, since the harmful effects of ionizing radiation were not yet known.

FIG. 1.4. Shoe fitting fluoroscope. Machines like the one shown were used until 1950s in the United States in order to attract customers to stores, promising the best fit possible for their new shoes.

It was soon recognized that X-ray irradiation is not efficiently absorbed by photographic film. In order to improve the image quality (by reducing exposure time) a material can be used that transforms ionizing radiation into light that is efficiently absorbed by photographic film. Immediately after the discovery of X-rays research on such materials began and only one year later, in 1896, Pupin found that $CaWO_4$ efficiently converts X-rays into violet light [4,5]. A material that converts invisible radiation into visible light is called a phosphor. When the invisible radiation is ionizing radiation, the material is called a scintillator. $CaWO_4$ was the first X-ray phosphor and was applied in so-called intensifying screens that were placed behind the patient in direct contact with the photographic film. The light emitted by the phosphor in the X-ray intensifying screen illuminates the film behind the screen giving rise to an X-ray image in the film. The use of an X-ray phosphor allows for a 1000-fold reduction of the X-ray dose. $CaWO_4$ was very successful and dominated the market for more than 80 years as phosphor in X-ray intensifying screens. It is still in use today because of the low production cost.

In the past century research was aimed at finding more efficient materials for the conversion of ionizing radiation into light. At the same time new techniques, different from classical X-ray photography, were developed in which ionizing radiation is used for medical imaging. A variety of new scintillators has been developed over the years. One of the most famous and widely applied scintillator materials is NaI:Tl. It was discovered by Hofstadter in 1948 and is one of the most efficient scintillator materials [6]. The response time is however long. In 1971 it was discovered that cross luminescence in BaF_2 had a very fast decay time, below 1 ns [7], but the light yield for this fast emission was very low. In 1973 $Bi_4Ge_3O_{12}$ (BGO) was introduced by Weber [8]. The material combines a high density, reasonably high light yield and sufficiently fast response time for many applications and has been widely studied. Today BGO serves as a standard material for comparison for newly developed scintillators. For PET-scanners (*vide infra)* a fast response time is crucial and the response time of BGO is too slow although it has been used in PET scanners. The most widely used scintillator in PET scanners is nowadays $Lu_2SiO_5:Ce^{3+}$ (LSO:Ce) which has been developed by Melcher in 1992 [9]. The scintillation properties are very good. The lifetime of the Ce^{3+} emission is 40 ns, which is fast but leaves room for improvement in case of fast timing applications. A breakthrough in combining very high light yield, high energy resolution and fast response time was achieved in 2002 when Dorenbos et al. reported the scintillation properties of $LaCl_3:Ce^{3+}$ [10]. In the years following other Ce-doped lanthanide halides were shown to also give high light yields, e.g. $LaBr_3$:Ce and LuI_3:Ce. Especially the record high light yield of LuI_3:Ce of 115 000 ph/MeV is worth mentioning. The class of LnX_3:Ce (Ln=La, Lu; X=Cl, Br, I) compounds is presently considered as outstanding scintillators [10-16]. Only the hygroscopic nature of the materials poses a problem in application. The relatively low density and response time need to be improved in order for these materials to be called "ultimate and ideal" scintillators. The work on this class of materials has triggered a more widespread attention to halide scintillators doped with Ce or Pr.

Since the development of planar X-ray photography using intensifying screens, many other techniques have been developed for medical imaging, not all relying on ionizing radiation. Ultrasound and Magnetic Resonance Imaging (MRI) are two widespread techniques that do not use harmful X-rays. Computed Tomography (CT), Single Photon Emission Computed Tomography (SPECT) and Positron Emission Tomography (PET) are examples of new imaging techniques relying on ionizing radiation. The different techniques have specific characteristics that make them suitable for diagnosis of specific health problems. Sometimes combinations of different techniques are required, e.g. CT-MRI. Planar X-ray photography is commonly used for imaging of simple bone fractures. New developments in this old area include digital X-ray photography, where film is no longer required and images can be digitally enhanced. Ultrasound relies on detecting reflected ultrasound waves and is widely used for checking the status of a fetus in the

womb. MRI is capable of imaging soft tissue. In a strong magnetic field the magnetic moments of hydrogen nuclei are aligned and a 3D image can be constructed from the detection of the density of hydrogen nuclei (water) in the body while additional information can be obtained by the use of magnetic probes which specifically bind to e.g. tumors. CT, SPECT and PET are modern X-ray and γ-ray imaging techniques. CT images are obtained by scanning an X-ray source and (scintillator) detector ring around a patient. A 3D image is constructed from the varying patterns of transmitted X-rays for different angles (the principle of tomography). The 3D-image gives information that cannot be obtained from planar X-ray images as it shows the 3D structure and depth of the abnormality in the body. The X-ray dose delivered to the patient is however significantly higher. SPECT and PET are techniques where γ-rays are used. The ionizing radiation is emitted by a radioactive isotope that is injected in the patient. In the case of SPECT γ-rays are emitted by a radioactive isotope in a specific label that accumulates in an organ (e.g. for detection of tumors) or the blood stream (to image the blood flow through the heart or brain). Similar to CT, a ring of scintillators detectors around the patient detects the emitted γ-rays and a 3D image is reconstructed (tomography) of the position and movement of the radioactive labels from the pattern of the detected γ-rays.

1.2 POSITRON EMISSION TOMOGRAPHY (PET)

FIG. 1.5. Positron Emission Tomography (PET) scanner.

From the different medical imaging techniques relying on ionizing radiation, PET is the most sophisticated. It also imposes the most stringent requirements on the scintillator material. As a result, it was introduced in 1985, at the University of California, and is the most recent of the imaging techniques based on ionizing radiation. It allows for the tracking of metabolic processes in the body and places with abnormal metabolic activity can be located (e.g. tumors or brain activity can be visualized in 3D).

In order to diagnose a patient a radioactive label is injected. The choice of the label as well as the type of radioactive isotope depends on the part or process in the body that needs to be imaged. The radioactive isotope is however always a positron emitter. An illustrative example is monitoring brain activity. The patient is injected with chemically modified sugar (glucose) where one of the hydroxyl (OH^-) groups is replaced the radioactive fluorine-18 isotope ($^{18}F^-$). Chemically, this modified glucose is similar to regular glucose and it travels in body to places with an increased need for energy, for example to the brain. Brain activity has glucose as the prime energy source. The $^{18}F^-$ isotope decays in the part of the body where it accumulates. Decay involves the emission of a positron (e^+). A positron, being the anti-particle of an electron (e^-), will rapidly find an electron in its surroundings leading to positron-electron annihilation. The mass of the electron and positron is converted into energy (according to the famous relation of Einstein: $E=m\cdot c^2$) and released in the form of two high energy γ-rays of equal energy (511 keV) travelling in opposite direction to satisfy the law of conservation of momentum. Due to the very high energy of the γ-rays they are hardly absorbed or scattered in the body. The patient in the PET-scanner is surrounded by a ring of scintillator detectors (FIG. 1.5). In modern machines as many as 17 000 scintillator crystals are present in the detection ring, which contributes to the high price of the system. The scintillator crystals absorb the 511 keV γ-photons and convert the energy to very short UV or visible light pulses. These pulses are detected by photo-detectors combined with every scintillator crystal. A crucial aspect is the simultaneous detection of γ-photons. This implies that the γ-rays were emitted at the same time and thus result from a positron-electron annihilation event. Since the γ-photons are emitted under an 180^o angle (opposite directions) the systems registers that such an event results from a positron being released somewhere on a straight line between the two scintillator crystals (Line of Response, LOR). In FIG. 1.6 a schematic picture is shown to illustrate the process. By registering numerous events, the intersections of all the LORs give an image of the distribution of the labeled glucose [17, 18]. A more recent development is to not only construct images from the LORs but to detect small differences in arrival times at the scintillator for two γ-rays that originate from a single positron-electron annihilation event. This technique is called Time-of-Flight PET (TOF-PET). The difference in arrival time gives information on where on the LOR the annihilation has taken place and improves the accuracy of the technique and results in higher spatial resolution images and a more precise diagnosis. Given the travelling velocity of γ-rays (speed of

light) a crucial condition for TOF-PET is a very fast time response of the detection system and ns or even sub-ns differences in rise times of the signal need to be detected. After initial interest in the 1980s, the lack of sufficiently fast scintillators reduced activities on TOF-PET. Recently, a renewed interest has been triggered by the development of faster scintillators. In the next section several aspects of scintillator performance, including the response time, will be addressed in more detail.

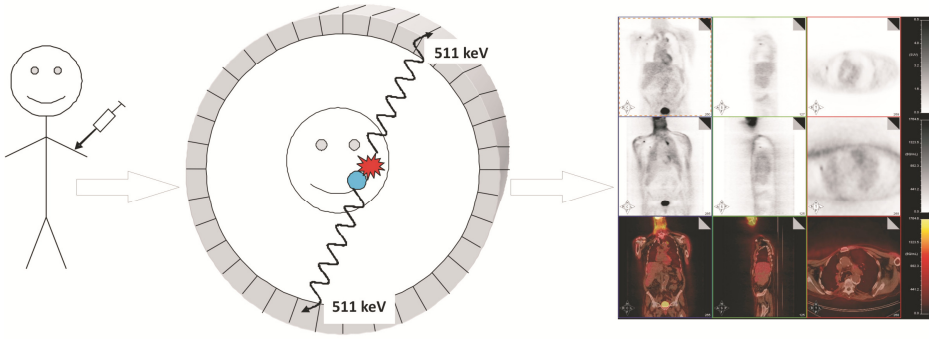

FIG. 1.6. Schematic depiction of the procedure undertaken in order to diagnose a patient using a PET scanner.

1.3 SCINTILLATORS AND SCINTILLATION

Planar X-ray Photography, CT, SPECT and PET are all medical imaging techniques where a crucial part of the machine is the scintillator material. Depending on the specific technique, the scintillator can be in the form of a microcrystalline powder (a phosphor) or a single crystal or ceramic of mm-cm dimensions. Depending on the application, the specific properties of the scintillator material varies. All scintillators have in common that they are capable of efficiently absorbing high energy electromagnetic radiation (X-rays or γ-rays) or energetic particles (α- or β-radiation) and transforming the energy into photons in the UV-VIS part of the spectrum which can be detected by a photomultiplier tube (PMT) or charge coupled device (CCD) detector. The process of absorption of the ionizing radiation, energy transfer to the activator and emission of light are all part of the scintillation process. Scintillators are used in a wide range of applications, including medical imaging, nuclear medicine, high energy physics, well-

logging, space exploration and homeland security. The following aspects are important in the evaluation of the performance of a scintillator material [17-20]:

High light output –The number of photons emitted by a scintillator after absorption of the incoming high energy radiation must be as high as possible. The more light is generated, the higher the sensitivity will be. The light output is typically given as the number of photons emitted per MeV of energy of the incoming radiation (ph/MeV). Typical numbers for scintillators for PET-scanners are above 25 000 ph/MeV.

Short emission lifetime / rise time – A short response time of the emission is especially important in PET-scanners since coincident detection of γ-rays is crucial. Emission lifetimes and rise times below 100 ns are required. For CT scanners and planar X-ray photography response times in the μs and even ms time regime are acceptable.

Afterglow – Persistent emission or afterglow is emission that continues for seconds, minutes or even hours after excitation has ended. It is caused by the slow thermally activated release of trapped charge carriers that have been created under high energy excitation. It lowers the direct light output and leads to ghost images and should be avoided in scintillator materials. The afterglow properties do not only depend on the scintillator material but are strongly influenced by the synthesis as it involves defects. Afterglow can be reduced by optimizing the synthesis procedure. Also, some correction for afterglow is possible by software.

Efficient energy transfer – Closely related with the overall light output of the scintillator is the energy transfer efficiency. If the emission of light originates from activator ions which are incorporated in a crystalline host, efficient energy transfer from the host lattice to the activator is required. Initially the ionizing radiation results in the generation of free electrons and holes in the host material. Efficient trapping of the charge carriers by the activator ions or energy transfer from excitonic states to the emitting state of the activator will yield a high light output. The energy transfer efficiency depends on the spectral overlap between host lattice emission and activator absorption bands. Not all scintillators rely on emission from an activator. For scintillators which show intrinsic emission, e.g. $CaWO_4$ and BGO, energy transfer to the emitting state of the host lattice determines the efficiency.

Radiation hardness – Since a scintillator is irradiated with high energy radiation it is important that the material is stable under high energy radiation. Many materials degrade under high energy radiation as a result of the formation of radiation induced defects (e.g. F-centers). The formation of defects is caused by radiation induced changes in the structure of the material due to bond breaking or atom/ion displacement. Color centers and defects reduce the efficiency of the scintillator by competitive trapping of the charge carriers and radiative or non-radiative energy/light trapping by defect states. For the long term

performance of scintillators it is crucial that defect formation under ionizing radiation is minimized.

Chemical stability – The chemical composition of a scintillator should not change over time due to exposure to the environment or high energy radiation. Changes due to absorption of water (for hygroscopic scintillators) or the change in valence states of activator ions in an oxidizing environment are examples of undesired chemical changes. If scintillator materials are sensitive to chemical changes in an ambient environment, encapsulation can be used to protect the material and improve the stability.

High total absorption coefficient (Stopping power) – To be capable of absorbing all the high energy radiation a scintillator needs to have a high density. It is important that all the energy of the high energy X-ray is deposited in the scintillator crystal and converted to light, not only for detection efficiency but also to determine the energy of γ-rays. The absorption coefficient for X-ray and γ-rays depends on the composition and the energy of the radiation. The process of absorbing the energy of incoming radiation involves interaction between the radiation and electrons in the scintillator. Elements with a high atomic number (Z) have higher electron densities and thus a higher absorption cross-section for X-rays and γ-rays. In Fig. 1.7 the importance for high atomic numbers Z to realize high stopping power is illustrated. In PET scanners it is crucial to absorb all energy in mm sized crystals. A smaller size reduces material cost and allows for better spatial resolution. Still, the crystal has to be thick enough to ensure almost complete absorption of the energy of the γ-photon. The total light intensity is a measure of the energy of the γ-photon and it is important to measure the energy and to discriminate against photons with energies lower than 511 keV. If γ-rays are scattered in the body they lose part of their energy. Scattered photons should not be considered since the LOR between scintillators detecting a scattered γ-photon no longer contains the point of the electron-positron annihilation.

Detection efficiency / emission wavelength – The emission of the scintillator has to be detected with the highest possible sensitivity. This depends on the wavelength of the emission and the type of detector used. If the emission is detected with a PMT, the best signal to noise ratio is obtained in the UV-blue part of the spectrum. On the other hand, if the detector is a CCD camera or a Si-photodiode, the emission should be in the red spectral region to obtain the best sensitivity. If the emission of the scintillator is not within this spectral range, a wavelength shifter may used to increase the sensitivity. It is important that the wavelength shifter does not lead to a significant increase of the response time of the entire system.

The criteria discussed above constitute the general requirements for judging the performance of scintillator materials. Of course also the price is an aspect that needs to be considered. The ideal scintillator does not exist and one needs to make a choice based on the importance of certain requirements for a specific application. For planar X-ray

photography the requirements are the least strict. The material used is a microcrystalline powder of a scintillator material. A dense layer is bound in a matrix, e.g. a polymer, to form an intensifying screen. The screen is placed in front of photographic film in a cassette to record the image of the transmitted X-rays. The light output should be high, to reduce the X-ray dose. A response time of ms is not a problem, although afterglow should be avoided to prevent ghost images. The requirements for CT are more stringent. The uniformity and stability of the light output is very important to allow for reliable computed tomography. Afterglow is detrimental as many images are recorded in time and afterglow effects interfere with image reconstruction. The response time is not crucial and can be as long as ms.

PET is by far the most demanding of the techniques discussed. A short response time is one of the challenges. Since the technique relies on the coincident detection of two γ-rays, a shorter response time improves the resolution and sensitivity. The spatial resolution is presently ~ 5 mm and can be improved by a factor of 2-3 when TOF-PET is used. A high light output and high stopping power are important for a good energy resolution to allow for discrimination against scattered γ-photons of energies lower than 511 keV. Radiation hardness is also important since the energy of γ-photons (511 keV) is very high, much higher than the energies used in X-ray imaging. The presently used PET-scintillators have Ce^{3+} as activator with emission lifetimes of typically 30-40 ns. Improving this lifetime is one of the challenges in finding better scintillators for PET-scanners. Also the rise time of the emission (the rising edge of the emission intensity after impact of γ-photon) is important. The most accurate way to determine differences in arrival time in the case of TOF-PET is to monitor the off-set in time between the rising edges. Rise times well below 1 ns are possible.

The overall light yield of a scintillator depends on several processes. After absorbing the high energy radiation, the energy is converted into high energy ('hot') charge carriers which generate multiple electron-hole pairs. The energy of the electron-hole pairs is transferred to activator ions followed by emission from the activator. The overall efficiency depends on the different processes and is given by [19, 20]:

$$LY = 10^6/(\beta \cdot E_g) \cdot S \cdot Q \qquad (1.1)$$

where LY is the overall light yield (in photons/MeV), β is constant, E_g is the bandgap of the host material (in eV), S is the transfer efficiency of electron-hole pairs to the activator and Q is the quantum efficiency of the activator emission. The value for β is typically 2-3. It indicates that the energy required to generate one electron-hole pair is typically 2-3 times the band gap energy of the host material. If the transfer efficiency S and quantum efficiency Q are taken as unity (which is not unrealistic) the maximum light yield of a scintillator can be estimated. Note that a higher LY can be achieved in smaller bandgap materials.

The most widely used activator ions in scintillator materials are lanthanide ions. Especially trivalent cerium (Ce^{3+}) has been the ion of choice due to the relatively fast emission and high efficiency. Also trivalent praseodymium (Pr^{3+}) and neodymium (Nd^{3+}) have gained interest because of the potential to have even shorter emission lifetimes. In the next sections the history and optical properties of the lanthanide ions will be discussed.

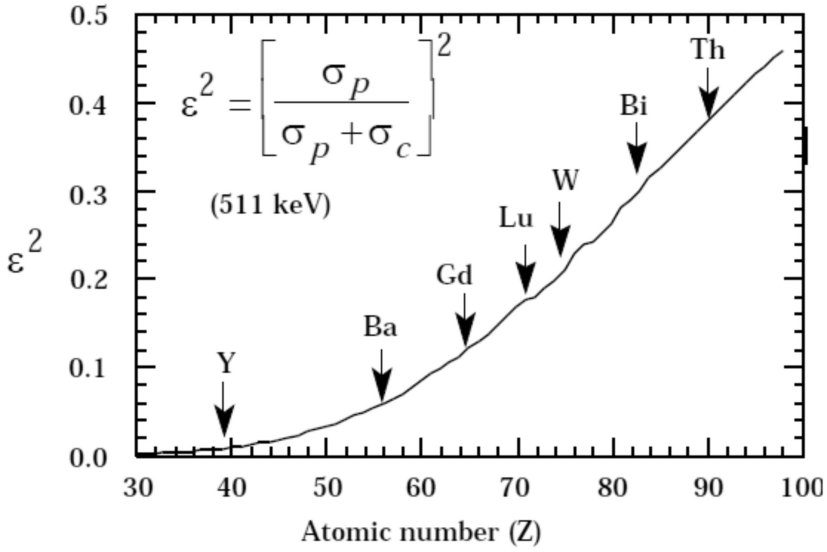

FIG. 1.7. Double photoelectric interaction probability. The probability that both annihilation photons of 511 keV will interact with the scintillator via a photoelectric effect as a function of the atomic number of the elements comprising the scintillator. Graph taken from REF. 17.

1.4 LANTHANIDES

The lanthanides are the group of elements with an incompletely filled *4f* inner shell. In the periodic table the lanthanides can be found after the element La. The lanthanides (Ln) comprise lanthanum (La), cerium (Ce), praseodymium (Pr), neodymium (Nd), promethium (Pm), samarium (Sm), europium (Eu), gadolinium (Gd), terbium (Tb), dysprosium (Dy), holmium (Ho), erbium (Er), thulium (Tm), ytterbium (Yb) and lutetium (Lu). The name comes from the Greek word *λανθανειν* which means 'to lie hidden'. This name was given because of the fact that when La was discovered in 1839, it was an

impurity 'hiding' in a sample of cerium nitrate. Accidentally, the lanthanides are also hidden in the periodic table along with the actinides (the group of elements where the *5f* inner shell is partially filled with electrons). The two rows of *f*-block elements are positioned at the bottom of the periodic table. The lanthanides are sometimes called rare earth elements or simply rare earths (RE). The correct definition of the rare earth elements includes, in addition to the lanthanides, also the elements yttrium (Y) and scandium (Sc). The lanthanides are found as mixtures in minerals like monazite. The common oxidation state is the trivalent state (Ln^{3+}) but some lanthanides also exist in the divalent or tetravalent state, e.g. Eu^{2+}, Sm^{2+}, Yb^{2+}, Ce^{4+}, Pr^{4+} and Tb^{4+}.

The history of the lanthanides starts in the year 1787 near the small village Ytterby in Sweden when Arrhenius found a black stone which he called Yttria [21]. In 1803 Klaproth found another mineral which was given the name of Ceria. Decades later it was realized that these minerals contained a mixture of a number of new chemical elements. Efforts were made to separate these new elements from the minerals. The light lanthanides were isolated from Ceria [22] and included lanthanum, cerium, didymium, samarium, europium and gadolinium. Later it was realized that didymium was not a single element and it was separated into praseodymium and neodymium. The heavy lanthanides were isolated from Yttria [22] and included terbium, dysprosium, holmium, erbium, thulium, ytterbium and lastly lutetium.

It took a considerable amount of time and effort to isolate all the different lanthanides in their pure form. The reason is the fact that the lanthanides have very similar chemical properties and separation of these elements cannot be done by methods based on chemical differences. The difference between the lanthanides is the number of electrons in the inner *4f* shell. The valence orbitals (*5s*, *5p* and *6s*) are the same for all the lanthanides and as a result the chemical properties are very similar. New techniques were developed to purify the lanthanides. Initially re-crystallization was used to purify lanthanides. Later the technique of choice became ion exchange chromatography which uses long columns and small differences in affinity of lanthanide ions for the resins in the columns to separate the lanthanides. Presently also exchange techniques using differences in complex formation of lanthanide ions are used. With these new separation techniques rare earth oxides can be obtained with purities as high 99.9999% (6N) [23]. Also the analysis of the purity of the samples posed challenges and promoted the development of new analysis techniques like inductively coupled plasma atomic emission spectroscopy (ICP-AES). To appreciate the difficulties in separation and purification of lanthanides it is insightful to mention that in order to obtain the first pure sample of Dy, 58 re-crystallization steps were necessary. The first pure Tm sample required 11 000 re-crystallizations [24].

It is often assumed that the rare earths (and thus the lanthanides) are rare elements. In discussions on scarcity of elements people often think of the rare earths. However, their

name from the point of view of their abundance is outdated. Initially they were considered to be rare but based on new insights it has become clear that the rare earths are relatively abundant. The rarest of the rare earths (apart from Pm, which has no stable isotope) is thulium. The abundance in the earth's crust of thulium is 0.2 ppm which is comparable to silver (0.08 ppm) or cadmium (0.15 ppm) and much higher than for example gold (0.003 ppm). The most abundant of the rare earths is cerium (65 ppm), very similar to zinc or copper. On the other hand, mining of rare earths is a complex process and presently 97% of the production comes from China [25]. Recent export limitations imposed by China will cause a shortage of rare earths in the near future. Based on the increasing importance of rare earths in modern technology this is especially important for Europe where, apart from a limited production in Estonia, there is no mining of rare earths. Following the export limitations by China new production sites are explored (e.g. in Canada) and old mines are re-opened (e.g. the Mountain Pass in California and in Western Australia). There is also a chance that the recently discovered deposits of rare earth minerals found in the Pacific Ocean floor could be mined [26]. The problem with mining, however, is the depth, since the minerals have been found at dephs reaching 3500-6000 meters. This might prevent the mining to be worthwhile from an economic point of view.

The strategic importance of lanthanides is based on the unique optical and magnetic properties arising from the partly filled *4f* shell. This has resulted in the widespread use of lanthanides in industrial and military applications. The optical properties are responsible for applications of lanthanides in lighting (fluorescent tubes, white light LEDs), displays (CRT, PDP), lasers, telecommunication (fiber amplifiers) and medical imaging (bio-labels, PET, CT). The magnetic properties are used in Nd, Tb and Sm based magnets with superior magnetic moments which find application in e.g. wind turbines, hybrid cars and headsets. Other applications of lanthanides include catalysis (La, Ce), batteries (La), polishing agent (CeO_2), in metallurgy as additive to strengthen steel (mixture of lanthanides) and in glass to realize a higher refractive index.

1.5 $4f^{n-1}5d \leftrightarrow 4f^{n}$ LUMINESCENCE

The optical properties of lanthanides can be ascribed to different types of transitions, both *intra*configurational and *inter*configurational. The intraconfigurational transitions within the $4f^{n}$ shell (n=1-13) are well-known and are responsible for the characteristic luminescence of lanthanides. The partly filled *4f* shell gives rise to a large number of energy levels related to different distributions of the n *4f* electrons over the 14 possible *4f* orbitals (7 orbitals, one electron with spin up and one with spin down). The different distributions have different energies due to interaction between the *4f* electrons

(electrostatic interactions and spin-orbit coupling). The different energy levels are labeled by term symbols. Transitions between the different energy levels within the $4f^n$ configuration ($4f^n \rightarrow 4f^n$ transitions or *f-f* transitions) are characterized by sharp atomic-like lines, weak oscillator strengths and the transition energies are independent of the surroundings. This is due to the fact that the 4*f* electrons are shielded from the surrounding ligands by the filled *5s* and *5p* orbitals which make the energy level structure insensitive to the environment. Intraconfigurational transitions are parity forbidden which explains the low oscillator strengths and long (ms) emission lifetimes for *f-f* transitions. It is only through the admixture of opposite parity states that the transitions become partly allowed as electric dipole transitions. *f-f* transitions are situated in the NIR, VIS and UV part of the electromagnetic spectrum. Efficient emission due to *f-f* transition is used in many applications. However, the long emission lifetime (ms) makes *f-f* emission unsuitable for scintillator materials for PET scanners.

At higher energies, typically in the UV, interconfigurational transitions are observed for lanthanide ions. Two types of interconfigurational transitions can occur: $4f^n \rightarrow 4f^{n-1}5d$ (or simply *fd*) transitions and charge transfer (CT) transitions. In case of *fd* transitions a *4f* electron is excited to the *5d* orbital. Charge transfer transitions involve the excitation of an electron in an orbital with predominant ligand character (e.g. O (*2p*)) to a *4f* orbital. Both types of transitions are parity allowed, giving rise to high oscillator strengths and strong absorption bands. The emission is characterized by short lifetimes. The observation of broad bands for these transitions can be understood from the configurational coordinate diagram. The transition involves a change in the bond strength between the lanthanide ion and the ligands. As a result the equilibrium distance (bond length) changes upon excitation and there is a strong coupling with vibrations, leading to strong vibronic transitions both in absorption and emission. Typical bandwidths (full width at half maximum, FWHM) are 1000 to 4000 cm^{-1}.

In case of *fd* transitions for the heavy lanthanides (n>7) both spin-allowed and spin-forbidden *fd* transitions have been observed since the lowest energy $4f^{n-1}5d$ state has a higher spin multiplicity than the $4f^n$ ground state. Up to n=7 all electron spins are parallel in the ground state of the lanthanide ions, giving maximum spin-multiplicity, which does not change when one of the electrons is promoted to the *5d* orbital. For n>7 the extra electrons (over 7) have to pair the electron spin since two electrons occupy the same *4f* orbital (Pauli principle). Excitation of one of the *4f* electrons to the *5d* orbital results in a $4f^{n-1}5d$ excited state for which the spin multiplicity can be higher than for the ground state: changing the orientation of the *5d* electron to be parallel to unpaired electron spins of the $4f^{n-1}$ electrons is possible since the electrons now occupy different orbitals. The high spin state is lower in energy (Hund's rule). Transitions from the ground state to the high spin state involve the change in electron spin orientation (spin flip) and the transitions have a low oscillator strength due to the spin-forbidden character.

The parity allowed interconfigurational transitions have high oscillator strengths and emission from these states will be characterized by short lifetimes. Charge transfer emission from a trivalent lanthanide has only been observed for Yb^{3+} but the radiative lifetime (~200 ns) is not fast enough for application in scintillators. Efficient emission from $4f^{n-1}5d$ states has been observed for a limited number of lanthanide ions: Ce^{3+}, Pr^{3+}, Nd^{3+}, Er^{3+} and Tm^{3+}. For the other lanthanides fast relaxation to $4f^{n}$ levels close in energy prevent the observation of *d-f* emission or lowers the efficiency. For Er^{3+} ($4f^{11}$) and Tm^{3+} ($4f^{12}$) the dominant *d-f* emission is from the high spin state. The lifetime for these emissions is long (~ µs) due to the spin selection rule. This leaves Ce^{3+}, Pr^{3+}, Nd^{3+} as ions for which efficient and fast spin-allowed *d-f* emission can be observed. In this thesis we will focus on fast *d-f* emission from these ions. A more complete discussion of spin-allowed and spin-forbidden *d-f* emission from lanthanides can be found in a series of papers by van Pieterson et al. [27-30].

Contrary to the *4f* orbitals, the *5d* orbitals of lanthanides have a strong interaction with the surrounding ligands. The energy of the 5*d* levels is influenced by covalency and the crystal-field induced by the ligands. Covalency effects cause a shift to lower energies of the *5d* level which is known as the nephelauxetic (Greek for 'cloud expanding') effect. As a result of covalent bonding between the *5d* and the ligand orbitals, the *5d* orbital expands by partial delocalization over the ligands and the energy is lowered. For more covalent ligands the energy of the *5d* level shifts to lower energies. The crystal-field is responsible for a splitting of the *5d* level. For the free ion the five *5d* orbitals have the same energy. The presence of ligands induces a splitting into a maximum of five crystal-field levels due to the differences in orientation of the *d*-orbitals with respect to the negatively charged ligands. The splitting depends on the type of ligands, the distance to the ligands and the symmetry. Higher formal charges and smaller distances give a larger crystal-field splitting. In high symmetry (octahedral or tetrahedral) the *5d* levels split into two groups while lowering the symmetry leads to splitting into more crystal-field components, up to five for the lowest symmetries. As a result, $4f^{n} \rightarrow 4f^{n-1}5d$ absorption bands spread over a large spectral region and strongly depend on the type of lanthanide ion and the host lattice. Emission is observed from the lowest energy *5d* state. The *d-f* emission shifts to lower energies with increasing covalency and crystal-field splitting. As a result, for the same lanthanide ion the *d-f* emission can vary strongly, depending on the host lattice. An illustrative example is Ce^{3+}. The Ce^{3+} ion has a single *4f* electron and the $4f^{1}$ ground state is split by spin-orbit coupling into a $^{2}F_{5/2}$ and a $^{2}F_{7/2}$ level, separated by 2000 cm^{-1}. The *d-f* emission shows a characteristic doublet structure of two emission bands separated by 2000 cm^{-1} which is in the UV for Ce in ionic fluorides and shifts to the orange/red spectral region for Ce in covalent sulphides. Even though there is a wide spread in the positions of *fd* levels of lanthanides, there are clear trends in the positions. Following pioneering work of Blasse, systematic work by Dorenbos revealed that there is a strong correlation between

the positions of *fd* levels for different lanthanides. In a series of papers Dorenbos showed that there is constant energy difference between the *fd* absorption and emission bands for different lanthanides in the same host lattice [31-34]. For example, the lowest *fd* state of Pr^{3+} is always 12 240 cm^{-1} higher in energy than the lowest *d*-state of Ce^{3+}. All the energy differences have been tabulated and with the Dorenbos relation the energy of the *d-f* emission and *f-d* absorption bands can be calculated for all lanthanides, when the energies are known for one lanthanide ion in a specific host lattice.

The *f-d* transitions have been widely studied in the past for divalent lanthanides since the transitions are situated at lower energies than for trivalent lanthanides. For trivalent lanthanides *f-d* bands are typically found in the UV and VUV (Vacuum Ultra Violet) spectral region, which is not easily accessible experimentally. In the past 20 years however measurements using synchrotron radiation have been used to systematically explore the *f-d* transitions for trivalent lanthanides and this has resulted in theoretical models explaining the $4f^{n-1}5d$ energy level structure. The study of *d-f* emission in scintillator materials also benefits from the use of VUV radiation. In this thesis synchrotron radiation is used for UV and VUV excitation into $4f^{n-1}5d$ levels and over the bandgap of the host lattice to investigate the *fd* luminescence and transfer efficiency from host lattice to the emitting *d*-state. The short (ps) synchrotron pulse duration in combination with fast detectors makes it possible to follow the dynamics of the transfer and emission processes on a sub-ns time scale. In the next section the synchrotron VUV beamline is described in more detail. A typical example of excitation and emission spectra and time resolved measurements is shown in FIG. 1.8 for $Y_3Al_5O_{12}:Pr^{3+}$ (YAG:Pr). In the emission spectrum under 180 nm excitation (over the bandgap of the host lattice) both *d-f* emission from Pr^{3+} (between 290 and 450 nm) and host lattice emission (around 260 nm) are observed. The excitation spectrum of the *d-f* emission shows *f-d* excitation bands (240 and 280 nm) and host lattice excitation (below 200 nm). The inset shows the decay curve for the *d-f* emission from which the decay time of 23 ns can be determined. Using this type of measurements new insights can be obtained that help the design and understanding of processes in new scintillator materials.

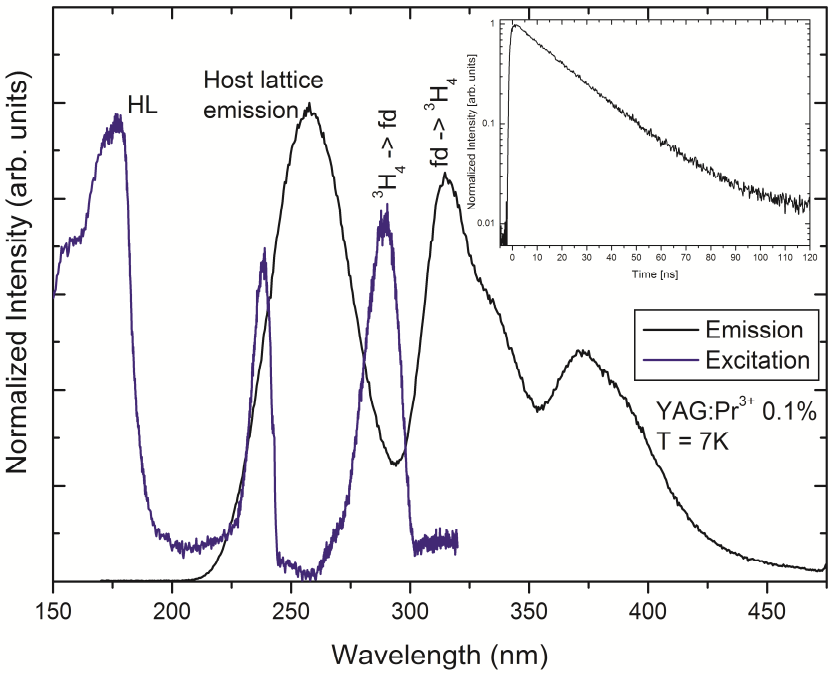

FIG. 1.8. Emission (λ_{exc}=180 nm) and excitation (λ_{em}=325 nm) spectra of $Y_3Al_5O_{12}:Pr^{3+}$ at 7 K measured at the Superlumi station of the DESY synchrotron. The inset shows an emission decay curve of YAG:Pr^{3+} at 7 K (λ_{exc}=290nm, λ_{em}=320 nm).

1.6 SYNCHROTRON (DESY) MEASUREMENTS

DESY (**D**eutsches **E**lektronen **Sy**nchrotron) is a renowned synchrotron facility in Hamburg, Germany. It was established on 18 December 1959. The measurements presented in this thesis were performed at the HASYLAB (**Ha**mburger **Sy**nchrotronstrahlungs**lab**or) laboratory at the Superlumi (I) station, using the radiation from the DORIS (**Do**ppel-**Ri**ng-**S**peicher) III storage ring. DORIS III is a positron storage ring, where positrons are accelerated using a series of linear accelerators (linac), bending magnets and wigglers. The Superlumi station (FIG. 1.9) is the beamline of choice when it comes to VUV luminescence measurements with very good spectral resolution in the excitation mode (~ 0.02 nm) and a very good timing resolution of the emission decay measurements (320 ps). The description of the entire setup can be found in the paper by

Zimmerer [35]. The accessible spectral range, depending on the monochromator-detector combination, is 115-750 nm for emission and 50-335 nm for excitation spectra. Using a liquid-nitrogen-cooled CCD camera one can extend the range of the emission measured to some 1050 nm. Reflectance spectra can also be measured at Superlumi station.

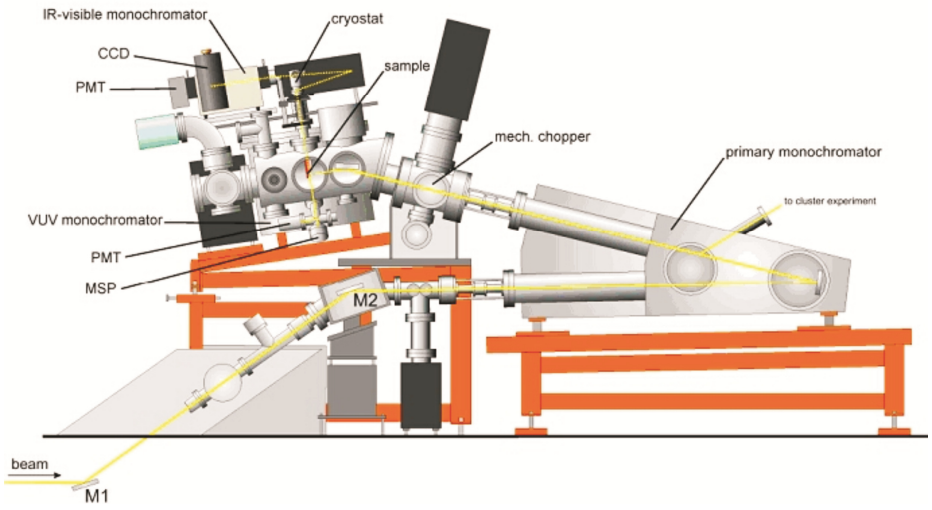

FIG. 1.9. Schematic representation of the Superlumi beamline at the DESY synchrotron in Hamburg. The excitation beam from the DORIS storage ring passes through a high resolution primary monochromator. Different emission monochromators and detectors are shown.

The excitation source is pulsed and the typical number of bunches in the ring (number of positron packages traveling in the ring at the same time) can be either 2 or 5, depending on the settings. The time interval between the incoming bunches is 480 ns or 192 ns, respectively. These also correspond to the maximum timescale for the decay measurements in the two bunches modes used. These time intervals are a result of the positron traveling with a speed very close to the speed of light (300 000 km/s) in a storage ring of circumfarance of 289.2 m. This means that it takes 0.964 μs for a single bunch of positrons to travel around the ring. The maximum initial current in the ring is about 150 mA. The current translates to the intensity of the incidence beam of synchrotron radiation and decreases linearly in time with the intensity.

The excitation spectra are corrected for the change in the ring current and by the excitation spectrum of sodium salicylate (NaSal), which allows for correcting for the spectral distribution of the excitation light.

The luminescence spectra can be measured in three time windows (integrated, fast and slow) making it possible to distinguish between fast and slow emissions. In case of the 5 bunch mode, the fast time window is delayed by about 2 ns from the start of the excitation pulse in order to suppress any scattered excitation light. The fast time window extends to about 14 ns, while the slow time window is set to record signal between about 100 and 200 ns after the excitation pulse. When the 2 bunch mode is used, the time windows are extended. The set-up also allows to measure reflection spectra of the samples.

Luminescence decay curves are recorded using time correlated photon counting with a time resolution of ~ 300 ps with a pulse length of about 130 ps. Time to Amplitude Conversion (TAC) is used for signal detection. TAC relies on ramping up a voltage linear in time after a trigger, simultaneously with the excitation pulse (the start pulse). When the detector measures a photon, a stop pulse is generated and the ramping of the voltage stops. The voltage is now a measure of the time elapsed between the excitation pulse and the emission of a photon. By measuring the voltage for many pulses and plotting the frequency for a voltage interval versus the voltage, a decay curve is obtained.

The measurements are performed in ultra high vacuum (UHV). The pressure in the sample chamber is in the order of 10^{-10}-10^{-9} mbar. The sample temperature can be varied between ~ 8 K and 320 K in a cold finger helium cryostat.

1.7 THESIS SUMMARY

The thesis introduces the reader to the exciting world of luminescence, scintillation and scintillator materials used in medical imaging. A number of imaging techniques are presented with emphasis on the crucial properties of materials used in those. The process of luminescence is the emission of light of various wavelengths, thus colors, which follows after a material, called a phosphor, is stimulated. The stimulation may have different origins.

The motivation for the research presented in this thesis was the need for improved materials for application in the Positron Emission Tomography technique, where the emission of light by the scintillator needs to be very fast (in the order of a few nanoseconds). Also a fundamental understanding of the scintillation process is necessary in order to improve the materials.

Since lanthanide ions are usually used as the activators for scintillators, their properties and the history of their discovery are given to familiarize the reader with the properties and benefits of these elements. Different kinds of emission that may take place on the lanthanide ions are described in relation to the fast timing application of materials activated with lanthanides. The state-of-the-art synchrotron facility of HASYLAB at DESY in Hamburg, Germany, is described in detail. The facility has been used in order to obtain the luminescence spectra and emission kinetics data presented in this thesis.

Chapter 2 shows how a very simple material could be used in order to achieve very fast luminescence. In this chapter the *f-f* and *d-f* luminescence of Ce^{3+}, Pr^{3+} and Nd^{3+} in NaCl is reported. The samples were prepared by rapid quenching of a NaCl-melt doped with lanthanides. Such procedure was required due to the fact of charge mismatch of the Na^{+} ions and the lanthanide (Ln^{3+}) ions. It is shown that both *f-f* and *d-f* emission from lanthanide ions can be observed in sodium chloride. Excitation and emission spectra are discussed. The emission of Ce^{3+} activated NaCl is centered at 360 nm and decays with a constant of about 21 ns. In case of Pr^{3+} activated material there is no *d-f* emission present due to the energy transfer to defect states present in the material. Doping of NaCl with Nd^{3+} does not lead to the emission characteristic of neodymium in the spectral region investigated. In addition to being interesting from a fundamental point of view, it is shown how the simple alkali halides doped with trivalent lanthanides may be used as hosts for new scintillator materials.

In the search for new scintillator materials, Ce^{3+} doped chlorides are a promising class of materials, combining a high efficiency and fast response time. Even shorter response times may be achieved by replacing Ce^{3+} by Pr^{3+} or Nd^{3+} as the lifetime of the *d-f* emission is substantially shorter for these ions. Chapter 3 reports on the luminescence properties of Ce^{3+}, Pr^{3+} and Nd^{3+} in RbCl. The potential of this simple chemical composition as a scintillator material is discussed. Under UV excitation Ce^{3+} shows *d-f* emission between 325 and 425 nm. The emission originates from multiple (differently charge compensated) Ce^{3+} sites. The luminescence lifetime varies with wavelength and is ~ 40 ns for the longer wavelength emission. For RbCl:Pr^{3+} three *d-f* emission bands are observed between 250 and 350 nm which can be assigned to transitions from the lowest energy *fd* state to different $^{3}H_{J}$ (J=4-6) states within the $4f^{2}$ configuration of Pr^{3+}. The decay time is ~ 17 ns. For the Nd^{3+} activated sample a weak emission band around 220 nm is observed only at 8 K which may be due to *d-f* emission. The very short lifetime (4 ns) is faster than the radiative lifetime, indicating that the *d-f* emission is quenched by relaxation to lower lying $4f^{3}$ states or by the process of photoionization. Under VUV excitation at wavelengths below 175 nm (the bandgap of RbCl) the *d-f* emission is very weak for Ce^{3+}, Pr^{3+} and Nd^{3+} doped RbCl and the emission spectra are dominated by defect related emission. This indicates that energy transfer from the host lattice to the *fd* states is inefficient which prevents application as a scintillator material.

The photoluminescence and radioluminescence of Ce^{3+}, Pr^{3+} and Nd^{3+} in $SrCl_2$ and $BaCl_2$ are reported and discussed in chapter 4 in relation to application as a (fast) scintillator material. The Ce^{3+} doped materials exhibit the typical fast cerium *d-f* emission (358, 382 nm in $SrCl_2$ and 350, 375 nm in $BaCl_2$) both under synchrotron and ionizing radiation excitations. A weak afterglow is observed. For Pr^{3+} a very fast *d-f* emission is observed in $SrCl_2$ (250, 263, 300 and 328 nm, τ=13 ns) and $BaCl_2$ (260, 288, 315 nm, τ=10 ns), but only under direct *f-d* excitation. No *d-f* luminescence is observed for Pr^{3+} under X-ray excitation. The absence of *d-f* emission is explained by the energy of the host lattice emission which is too low for energy transfer to the high energy *fd* states of Pr^{3+} (230 nm in $SrCl_2$ and 235 nm in $BaCl_2$). The neodymium doped chlorides do not show *d-f* luminescence.

In chapter 5 the luminescence properties of $Lu_3Al_5O_{12}$ (LuAG) doped with trivalent Ce and Tb ions are discussed. (LuAG) doped with Ce^{3+} is a promising scintillator material with a high density and a fast response time. The light output under X-ray or γ-ray excitation is, however, well below the theoretical limit. In this chapter the influence of co-doping with Tb^{3+} is investigated with the aim to increase the light output. High resolution spectra of singly doped LuAG (with Ce^{3+} or Tb^{3+}) are reported and provide insight into the energy level structure of the two ions in LuAG. For Ce^{3+} zero-phonon lines and vibronic structure are observed for the two lowest energy *5d* bands and the Stokes shift (2350 cm^{-1}) and Huang-Rhys coupling parameter (S=9) have been determined. Tb^{3+} *4f-5d* transitions to the high spin (HS) and low spin (LS) states are observed (including a zero-phonon line and vibrational structure for the high spin state). The HS - LS splitting of 5400 cm^{-1} is smaller than usually observed and is explained by a reduction of the *5d-4f* exchange coupling parameter J by covalency. Upon replacing the smaller Lu^{3+} ion with the larger Tb^{3+} ion, the crystal-field splitting for the lowest *5d* states increases causing the lowest *5d* state to shift below the $^5D_4$ state of Tb^{3+} and allowing for efficient energy transfer from Tb^{3+} to Ce^{3+} down to the lowest temperatures. Luminescence decay measurements confirm efficient energy transfer from Tb^{3+} to Ce^{3+} and provide a qualitative understanding of the energy transfer process. Co-doping with Tb^{3+} does not result in the desired increase in light output and an explanation based on electron trapping in defects is discussed.

Chapter 6 describes the relation between the radiative lifetime of an emission and the emission wavelength. The lifetime of the *d-f* emission of lanthanides in a host lattice is governed by Fermi's Golden Rule, which predicts a shortening of the emission lifetime with increasing energy. The knowledge of the radiative lifetime of a particular emission is of great importance in designing materials for specific applications, such as scintillating materials, where very fast decaying emission is required. Due to the increased interest in the investigation of scintillators based on the Pr^{3+} *d-f* emission, it is important, both from a theoretical and application point of view, to know the radiative lifetime of the Pr^{3+} *d-f* emission. No quantitative analysis of experimental data and comparison with that for Ce^{3+}

and Eu^{2+} *d-f* emission has been conducted so far. Here, an effort is made to compare the experimental data obtained on the Pr^{3+} *d-f* luminescence lifetimes in a large number of host lattices. The experimental data points have been fitted using different local-field correction models and for both the squared and cubic wavelength dependencies. The trend observed is best described using a full cavity model to correct for the local-field effects and a λ^3 factor to account for the energy of the transition. Still, there is a considerable scatter of the experimental data around the best fit to these data. The variation is explained by uncertainties in the refractive indices and a variation in the transition dipole moment of the *d-f* transition for Pr^{3+}. Based on the results, the shortest radiative lifetime that can be achieved for Pr^{3+} *d-f* emission is predicted to be about 6 ns.

Chapter 7 introduces the Dorenbos relation. The Dorenbos relation is an empirical model that correlates the position of the lowest *fd* level of any lanthanide ion with that of the Ce^{3+} ion in the same host lattice. This relation is therefore useful to estimate the position of the *fd* levels of trivalent lanthanide ions in any given host lattice, provided the peak position of the lowest *fd* band of at least one of the lanthanide ions in this host is known. In this work we investigate whether the Dorenbos relation is also applicable when zero-phonon lines (ZPLs) are used instead of the *fd* band maxima. To this end, the ZPL positions of the *fd* bands of all trivalent lanthanide ions in four different host lattices (CaF_2, $Y_3Al_5O_{12}$, $LiYF_4$, and YPO_4) were obtained and used as input in the Dorenbos relation. The results are compared to those obtained through the standard procedure using the band maxima. The data support the conclusion that the ZPL approach gives more accurate estimates for the position of the lowest *fd* level, particularly in wide band gap host lattices. This can be attributed to the fact that the position of the ZPL gives a more accurate determination of the energy of the *fd* states.

REFERENCES

[1] L.N. Cooper, "An Introduction to the Meaning and Structure of Physics" Harper & Row, New York, Evanston, London (1968)

[2] W.C. Roentgen, *Ann. Phys. Chem.* **64** (1898) 64

[3] L. Lewis, P.E. Caplan, *Calif Med.* **72**(1) (1950) 26

[4] S.C. Bushong, "Radiologic Science for Technologists" C.V. Mosby, St. Louis, MO, 1975

[5] L.H. Brixner, *Mater. Chem. Phys.* **16** (1987) 253

[6] R. Hofstadter, *Phys. Rev.* **74** (1948) 100

[7] M.R. Farukhi, C.F. Swinehart, *IEEE Trans. Nucl. Sci.* **NS-18** (1971) 200

[8] M.J. Weber, R.R. Monchamp, *J. Appl. Phys.* **44** (1973) 5495

[9] C.L. Melcher, J.S. Schweitzer, *IEEE Trans. Nucl. Sci.* **NS-39** (1992) 502
[10] E.V.D. van Loef, P. Dorenbos, C.W.E. van Eijk, K.W. Krämer, H.U. Güdel, *Appl. Phys. Lett.* **77** (2000) 1467
[11] K.S. Shah, J. Glodo, M. Klugerman, W.W. Moses, S.E. Derenzo, M.J. Weber, *IEEE Trans. Nucl. Sci.* **NS-50** (2003) 2410
[12] K.S. Shah, J. Glodo, M. Klugerman, L. Cirignano, W.W. Moses, S.E. Derenzo, M.J. Weber, *Nucl. Instrum. Methods A*. **505** (2003) 76
[13] E.V.D. van Loef, P. Dorenbos, C.W.E. van Eijk, K.W. Krämer, H.U. Güdel, *Nucl. Instrum. Methods A* **486** (2002) 254
[14] A. Bessiere, P. Dorenbos, C.W.E. van Eijk, K.W. Krämer, H.U. Güdel, C. de Mello Donegá, A. Meijerink, *Nucl. Instrum. Methods A* **537** (2005) 22
[15] E.V.D. van Loef, P. Dorenbos, C.W.E. van Eijk, K.W. Krämer, H.U. Güdel, *Nucl. Instrum. Methods A* **496** (2003) 138
[16] M.D. Birowosuto, P. Dorenbos, J.T.M. de Haas, C.W.E. van Eijk, K.W. Krämer, H.U. Güdel, *J. Lumin.* **118** (2006) 308
[17] W.W. Moses, S.E. Derenzo, *Proceedings of SCINT '95 (Edited by P. Dorenbos and C. W. E. v. Eijk), Delft, The Netherlands*, pp. 9-16, 1996
[18] W.W. Moses, *Proceedings of The International Conference on Inorganic Scintillators and Their Applications: SCINT99 (Edited by V. Mikhailin), Moscow, Russia*, pp. 11-21, 1999
[19] E. Zych, "Luminescence and Scintillation of Inorganic Phosphor Materials" in: H. Singh Nalwa and L. Shea Rohwer (Eds.), "Handbook of Luminescence, Display Materials, and Devices vol. 2", American Scientific Publishers (2003) 251
[20] A. Lempicki, A.J. Wojtowicz, C. Brecher, in: S.R. Rotman (Ed.), "Wide-Gap Luminescent Materials: Theory and Applications", Kluwer, Norwell, MA (1966) 235
[21] B. Geijer, *Annalen fur die Freunde der Naturlehre* **9** (1788) 223
[22] W.H. Brock, The Norton History of Chemistry (1st ed. W.W. Norton & Company) 1993
[23] Introduction to the Lanthanides.
URL: http://media.wiley.com/product_data/excerpt/53/04700100/0470010053.pdf
[24] URL:
http://int.ch.liv.ac.uk/Lanthanide/Ln_Chemistry_folder/Miscellaneous%20folder/Miscellaneous.html
[25] Annex V to the Report of the Ad-hoc Working Group on defining critical raw materials, European Commission Enterprise and Industry (2010)
[26] URL: http://www.bbc.co.uk/news/world-asia-pacific-14009910
[27] L. van Pieterson, Charge Transfer and $4f^n \leftrightarrow 4f^{n-1}5d$ Luminescence of Lanthanide Ions, PhD thesis, Universiteit Utrecht (2001)
[28] M.F. Reid, L. van Pieterson, R.T. Wegh, A. Meijerink, *Phys. Rev. B* **62** (2000) 14744

[29] L. van Pieterson, M.F. Reid, R.T. Wegh, S. Soverna, A. Meijerink, *Phys. Rev. B* **65** (2002) 045113
[30] L. van Pieterson, M.F. Reid, G.W. Burdick, A. Meijerink, *Phys. Rev. B* **65** (2002) 045114
[31] P. Dorenbos, *J. Lumin.* **87-89** (2000) 970
[32] P. Dorenbos, *J. Lumin.* **91** (2000) 91
[33] P. Dorenbos, *J. Lumin.* **91** (2000) 155
[34] P. Dorenbos, *J. Lumin.* **108** (2004) 301
[35] G. Zimmerer, *Nucl. Instrum. Methods A* **308** (1991) 178

2

Luminescent salt

ABSTRACT

In this chapter *f-f* and *d-f* luminescence spectra of Ce^{3+}, Pr^{3+}, Nd^{3+} in NaCl are reported alongside the luminescence decay curves. The samples were prepared by rapid quenching of a NaCl-melt doped with lanthanides. It is shown that both *f-f* and *d-f* emission from lanthanide ions can be observed. Excitation and emission spectra are discussed. In addition to being interesting from a fundamental point of view, it will be argued how the simple alkali halides doped with trivalent lanthanides may be promising as hosts for new scintillator materials.

2.1 INTRODUCTION

Luminescence of lanthanide ions has been studied in a wide variety of host lattices. It is well-known that the trivalent lanthanides can show a bright and characteristic luminescence due to both *f-f* transitions and *d-f* transitions. In spite of the wide range of chemical compositions and crystal structures that have been investigated, the most simple and best known crystal has not been used as a host matrix for luminescent trivalent lanthanides: table salt or NaCl.

Sodium chloride, NaCl, is a very well-known inorganic salt, with a simple cubic structure. Besides applications in gastronomy, table salt might be of interest from a scientific point of view. Several aspects of sodium chloride luminescence have been investigated in the past [1,2], but no literature has been found on trivalent lanthanide luminescence in this host. One of the reasons for the lack of data on trivalent lanthanides in sodium chloride is the difficulty of incorporating a trivalent lanthanide on a monovalent sodium site.

For Ce^{3+}, Pr^{3+} and Nd^{3+} incorporated in NaCl fast *d-f* emission of these lanthanides may be observed, since the bandgap of sodium chloride is rather large (~ 8.5 eV) [3,4]. Our measurements confirm that the bandgap is of about 8.5 eV (about 145 nm). Here we report preliminary results on the luminescence of Ce^{3+}, Pr^{3+} and Nd^{3+} in NaCl. Fast cerium *d-f* emission has been observed, but no evidence for the *d-f* emission of praseodymium is found and only *f-f* emission from Pr^{3+} is observed. NaCl:Nd^{3+} did not show any Nd^{3+}-related emission in the investigated spectral range.

2.2 EXPERIMENTAL

2.2.1. Synthesis

The materials investigated have been obtained by melting sodium chloride and the appropriate rare-earth chloride using a high frequency furnace. The mixed chemicals have been dried at about 200°C overnight under a nitrogen flow. The temperature was then raised to 1100°C and kept constant for about 15 minutes. A rapid cooling followed resulting in a doped sodium chloride with no observable segregation of the lanthanide dopant.

2.2.2. Measurements

All the materials obtained have been characterized by XRD using a PW 1729 Philips diffractometer, equipped in a Cu K_α X-ray source (λ=1.5418Å). The luminescence spectra have been measured using a Spex Fluorolog spectrofluorometer. Samples doped with trivalent Ce^{3+}, Pr^{3+} and Nd^{3+} have also been measured using synchrotron radiation at SUPERLUMI station (DESY), described in more detail in section 1.6 of this thesis and extensively elsewhere [5].

2.3 RESULTS AND DISCUSSION

2.3.1. XRD

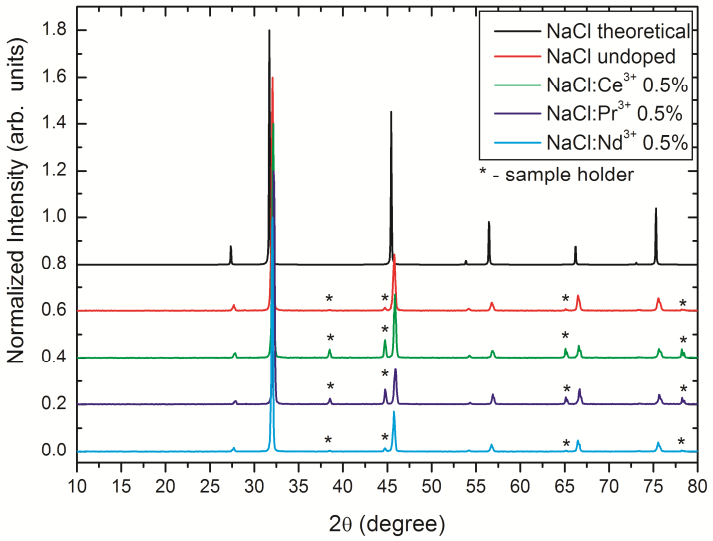

FIG. 2.1. XRD patterns of the undoped and Ce^{3+}, Pr^{3+} Nd^{3+} doped NaCl.

The XRD patterns of the undoped host lattice as well as the cerium, praseodymium and neodymium doped compounds together with the theoretical diffractogram (for

comparison) are shown in FIG. 2.1. The analysis of the obtained patterns shows, that there is a high degree of crystallization. All the peaks can be assigned to sodium chloride. No peaks coming from cerium, praseodymium or neodymium chlorides are present even at dopant concentrations as high as 2%. For comparison, we also measured diffractograms of mixtures of NaCl and $LnCl_3$ prior to melting (not shown) and were able to clearly observe the diffraction peaks of the $LnCl_3$ phase. The disappearance of these peaks after melting indicates that the Ln^{3+} ions are indeed incorporated in the NaCl matrix.

2.3.2 Luminescence

2.3.2.1 NaCl:Ce^{3+}

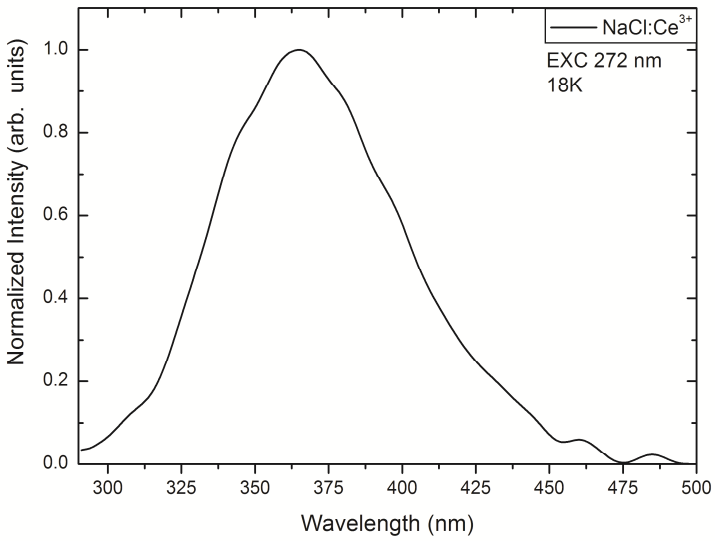

FIG. 2.2. Cerium *d-f* emission under direct cerium excitation at 18 K.

In FIG. 2.2 the emission spectrum of NaCl doped with Ce^{3+} is shown. The spectrum shows a broad band around 365 nm which is assigned to Ce^{3+} *d-f* emission. The band should consist of two bands, which are related to transitions from the lowest crystal-field component of the *5d* level of Ce^{3+} to the two $4f^1$ states, $^2F_{5/2}$ and $^2F_{7/2}$, separated by about 2000 cm^{-1}. The unusual shape of the emission band is due to the fact that there are

multiple sites present. This is due to the need for charge compensation. The typical doublet structure disappears due to overlap of these bands, forming just one broad spectral feature. Decay time measurements (FIG. 2.3) confirm the assignment of the 365 nm emission band to the Ce^{3+} *d-f* emission. The lifetime of the emission is 21 ns, which is close to the expected value for Ce^{3+} *d-f* emission in the UV range, which is typically between 20 and 30 ns [6]. The position of the Ce^{3+} emission band is almost the same as the position of a slower decaying emission, which is located around 360 nm and was observed for sodium chloride doped with Pr^{3+} and Nd^{3+} (vide infra). This emission is quenched at room temperature. Lifetime measurements help in distinguishing between the two. The luminescence decay time for the 360 nm emission (under a 120 nm excitation, above the bandgap) is a long decay (τ>1μs) (compare FIG. 2.3 with FIG. 2.6). Based on these observations, the 360 nm emission band , observed for the Pr^{3+} and Nd^{3+} doped NaCl, is assigned to a defect related emission, while the 365 nm emission in the Ce^{3+} doped sample is due to *d-f* emission from cerium.

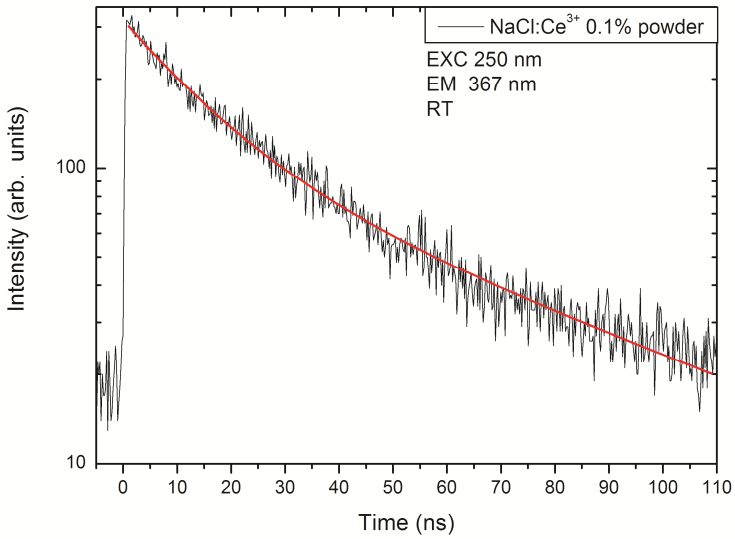

FIG. 2.3. Lifetime of the cerium *d-f* emission at RT under cerium excitation.

2.3.2.2. *NaCl:Pr^{3+}*

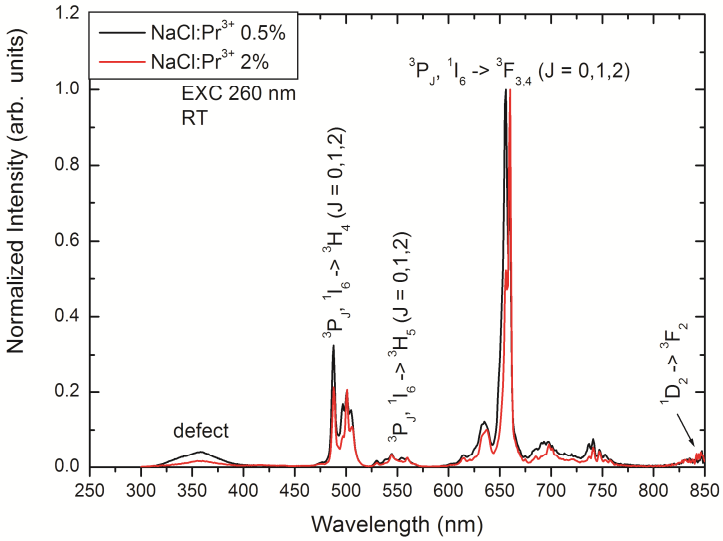

FIG. 2.4. Emission spectra of NaCl:Pr^{3+}.

Based on the data of the Ce^{3+} luminescence, a prediction of the position of the lowest crystal-field component of the 4*f5d* band can be made using the so-called Dorenbos relation [7]. The lowest praseodymium *f-d* excitation band in NaCl is expected around 210 nm. In FIG. 2.4 the excitation and emission spectra for NaCl:Pr^{3+} are shown. Upon excitation at 120 nm (supra-bandgap) a broad band at 240 nm is observed in the emission spectrum. This band is well-known for undoped NaCl and has been assigned to an STE emission [8]. There are also the intraconfigurational transitions of praseodymium present in the emission spectrum. These are located in the green and red spectral region ($\lambda \sim 500$ nm and $\lambda \sim 660$ nm, respectively). Under optical excitation at 260 nm the spectrum consists of the same narrow lines resulting from the transitions within the $4f^2$ configuration of praseodymium (FIG. 2.4), as well as a broad band around 360 nm. The broad band is assigned to a host lattice related emission. In the excitation spectrum of the intraconfigurational $4f^2$ emission, several bands are observed which can be assigned to *4f5d* excitation bands, as indicated in FIG. 2.5. It can however not be ruled out that (some of) the bands are related to host lattice (defect) absorption bands. There is no evidence for *d-f* luminescence which is expected between 230 and 300 nm based on the position of the *d-f* emission from Ce^{3+}. To explain this we consider the excitation spectrum of the

praseodymium doped material (FIG. 2.5). In addition to the bands assigned to *4f5d* transitions, there are also some broad absorption bands at longer wavelengths which are assigned to defect related absorption. The presence of these lower energy bands can explain the quenching of the *d-f* emission from Pr^{3+} by energy transfer to these defects. Sharp excitonic features are observed around 155 nm. Finally it is interesting to note that the intensity of the defect emission band around 360 nm depends on the Pr^{3+} concentration. It is stronger at lower Pr concentrations (see FIG. 2.4). Upon raising the Pr concentration, energy transfer to the $4f^2$ states of Pr^{3+} quenches the 360 nm emission.

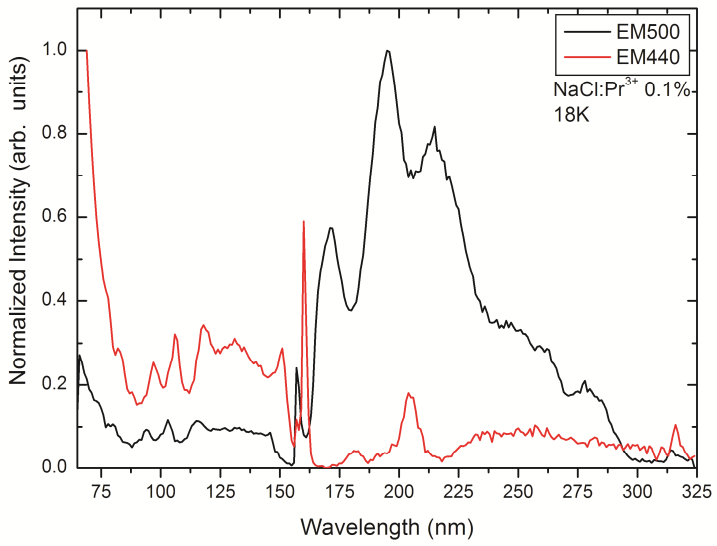

FIG. 2.5. Comparison of the excitation spectra of praseodymium and defect emissions at 18 K.

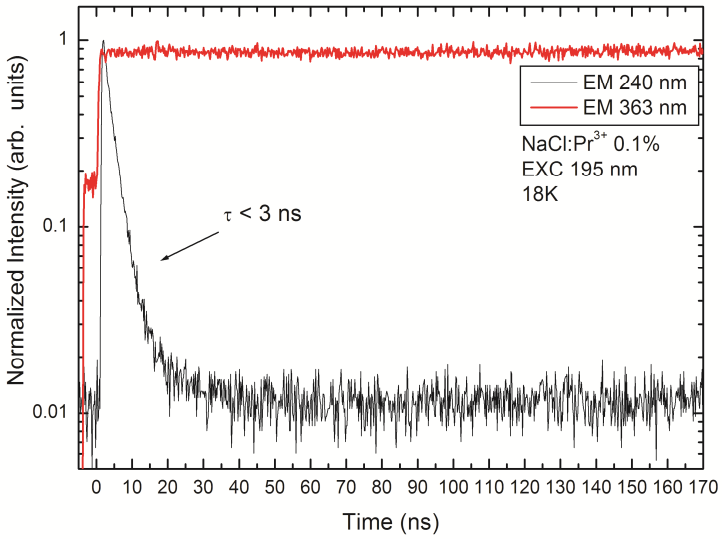

FIG. 2.6. Comparison of different time profiles of two different host lattice related emission in NaCl.

Lifetime measurements for the various emission bands observed in the praseodymium doped material are shown in FIG. 2.6. The STE emission (240 nm) is extremely fast (τ<3 ns) and the defect emission (360 nm) is very long lived and cannot be determined due to the high (MHz) repetition rate of excitation at the DESY synchrotron and can be estimated to be longer than τ>1μs. These results are consistent with the literature data [8].

2.3.2.3 NaCl:Nd^{3+}

The sample doped with neodymium did not show any luminescence related to either the intraconfigurational or interconfigurational transitions of Nd^{3+} in the investigated spectral range (180-700 nm) and only host lattice related luminescence is observed.

2.4 CONCLUSIONS

It has been shown that the trivalent lanthanides can be incorporated into ordinary table salt with no visible segregation of the dopant. There is evidence of efficient luminescence for Ce^{3+} (*d-f*) and Pr^{3+} (*f-f*), while no luminescence was observed for Nd^{3+} in NaCl. Further work on lanthanide luminescence in other (heavier) alkali halides may be interesting for scintillator applications.

REFERENCES

[1] B.P. Chandra, *Nucl. Tracks* **10** (1984) 225
[2] T. Tsuboi, H. Witzke, D.S. McClure, *J. Lumin.* **24/25** (1981) 305
[3] R.T. Poole, J. Liesegang, R.C.G. Leckey, J.G. Jenkin, *Phys. Rev. B* **11** (1975) 5190
[4] A.R. West in: "Solid State Chemistry and its Applications" (1995) Wiley & Sons
[5] G. Zimmerer, *Nucl. Instum. Methods A* **308** (1991) 178
[6] C.K. Duan, M.F. Reid, *Curr. Appl Phys.* **6** (2006) 348
[7] P. Dorendos, *J. Lumin.* **91** (2000) 155
[8] R.T. Williams, K.S. Song, *J. Phys. Chem. Solids* **51** (1990) 679

3

Fast *d-f* emission in Ce^{3+}, Pr^{3+} and Nd^{3+} activated RbCl

ABSTRACT

In the search for new scintillator materials, Ce^{3+} doped chlorides are a promising class of materials, combining a high efficiency and fast response time. Even shorter response times may be achieved by replacing Ce^{3+} by Pr^{3+} or Nd^{3+} as the lifetime of the *d-f* emission is substantially shorter for these ions. Here we report on the luminescence properties of Ce^{3+}, Pr^{3+} and Nd^{3+} in RbCl and investigate the potential as a scintillator material. Under UV excitation Ce^{3+} shows *d-f* emission between 325 and 425 nm. The emission originates from multiple (differently charge compensated) Ce^{3+} sites. The luminescence lifetime varies with wavelength and is ~ 40 ns for the longer wavelength emission. For RbCl:Pr^{3+} three *d-f* emission bands are observed between 250 and 350 nm which can be assigned to transitions from the lowest energy *fd* state to different ^3H_J (J=4-6) states within the $4f^2$ configuration of Pr^{3+}. The decay time is ~ 17 ns. For the Nd^{3+} activated sample a weak emission band around 220 nm is observed only at 8 K which may be due to *d-f* emission. The very short lifetime (4 ns) is faster than the radiative lifetime, indicating that the *d-f* emission is quenched by relaxation to lower lying $4f^3$ states or by the process of photoionization. Under VUV excitation at wavelengths below 175 nm (the bandgap of RbCl) the *d-f* emission is very weak for Ce^{3+}, Pr^{3+} and Nd^{3+} doped RbCl and the emission spectra are dominated by defect related emission. This indicates that energy transfer from the host lattice to the *fd* states is inefficient which prevents application as a scintillator material.

3.1 INTRODUCTION

Lanthanide (Ln) doped inorganic hosts have been intensively investigated in the past as possible scintillation materials and are presently used in multiple applications, such as medical imaging (positron emission tomography (PET), computed tomography (CT) or single photon emission tomography (SPECT)) and radiation detection for homeland security or high energy physics [1-3]. Many of the presently used scintillators are doped with Ce^{3+}, which exhibits efficient and relatively fast *d-f* emission. The typical radiative lifetime of Ce^{3+} emission is 30-70 ns, depending on the emission wavelength. The highest efficiencies have been reported for Ce^{3+} doped composition LnX_3 (X=Cl, Br, I; Ln=La, Lu) [4-7]. The exceptionally high scintillation efficiencies (up to 100 000 photons/MeV) and relatively short emission lifetimes (20-50 ns) result in an excellent energy resolution for these scintillator materials [4-10]. Also for other simple ionic halides *d-f* emission from Ln^{3+} has been investigated, viz. in NaCl [11], $SrCl_2$ and $BaCl_2$ [12-15]. It has been shown that incorporation of trivalent lanthanide ions is possible in these materials and fast *d-f* emission has been observed not only for cerium, but also for praseodymium and neodymium ions in these compounds.

The radiative lifetime decreases as the emission shifts to higher energies [1,16,17]. For the *d-f* emission from Ce^{3+} and Eu^{2+} the radiative decay rate has been demonstrated to be inversely proportional to λ^3 [16,17]. The higher energy of the *d-f* emission from Pr^{3+} and Nd^{3+} is responsible for the shorter decay times for *d-f* emission from these ions compared to Ce^{3+}. The higher energy position of the *fd* states might impose certain problems in case of luminescence originating from these states due to the proximity of the lowest *fd* level to the conduction band of the material, which might in turn lead to luminescence quenching via a process of photoionization. On the other hand, the scintillation light yield becomes lower in large bandgap materials, due to the smaller number of electron-hole (e-h) pairs that can be produced upon an excitation with high energy photons. This leads to an optimization of the combination of host lattice and lanthanide ion which will also depend on which property is more desired (response time or light yield) is more important for a specific application.

The relative positions of the *fd* levels of lanthanides are described by the Dorenbos relation [18]. For the Pr^{3+} the *fd* levels are located at about 12 240 cm^{-1} higher energies than for Ce^{3+} levels in the same host lattice [18]. As a result, the lifetime of the *d-f* emission is typically two times shorter for Pr^{3+} in comparison to Ce^{3+} [19,20]. In case of neodymium the lowest *fd* level is about 22 720 cm^{-1} higher than the cerium *fd* levels [18] and the decay of the *d-f* emission is even faster. Short emission lifetimes are especially important in applications such as PET which relies on the coincident detection of two

511 keV γ-quanta. A shorter lifetime results in an improved precision of detection and a higher resolution [21]. The very fast response time of scintillators based on Pr^{3+} *d-f* emission has triggered research on *d-f* emission from Pr^{3+} for application in scintillators.

Based on the high efficiency of the Ce^{3+} *d-f* emission in chlorides and the short lifetimes of *d-f* emission for Pr^{3+} and Nd^{3+}, it is worthwhile investigating *d-f* emission from these ions in chloride hosts. Here we investigate luminescence of trivalent Ce, Pr and Nd in RbCl. The density of RbCl is 2.83 g/cm^3 and it crystallizes in a simple cubic structure ($a = b = c = 6.57$ Å and $\alpha = \beta = \gamma = 90°$) [22]. RbCl is a well-known host for scintillator materials and has been doped with Tl^+ or Cs^+ to obtain efficient and fast scintillation [23,24]. However, incorporation of a trivalent lanthanide ion on the monovalent rubidium site is not trivial. Even though the monovalent rubidium site is large enough ($R_i = 1.61$ Å) to be replaced by a trivalent lanthanide ion ($R_i = 1.143$ Å, $R_i = 1.126$ Å and $R_i = 1.109$ Å for Ce^{3+}, Pr^{3+} and Nd^{3+}, respectively, in eight coordination [25]), there is still the problem of charge compensation, that leads to the creation of multiple sites and lattice defects. Successful incorporation of Sm^{3+} in RbCl has been reported, where RbCl:Sm^{3+} has exhibited afterglow and Sm^{3+} has been shown to act as an electron trap [26]. In this chapter we show that Ce^{3+}, Pr^{3+} and Nd^{3+} can be incorporated into RbCl. Short-lived *d-f* emission is observed. However, the efficiency of the *d-f* emission under host lattice excitation is very weak which limits the applicability as a scintillator material.

3.2 EXPERIMENTAL

3.2.1. Synthesis

To prepare doped rubidium chloride samples, anhydrous RbCl (99%, STREM CHEMICALS) and anhydrous $LnCl_3$ (Ln = Ce, Pr or Nd, 99.99%, ALDRICH) were used. A mixture of RbCl and approximately 0.5% molar of $LnCl_3$ was dried over night at 200°C under a constant nitrogen flow. The mixture was heated in a glassy carbon crucible to 300°C for 2 hours to remove traces of absorbed water or oxygen. Subsequently, the sample was molten by heating to about 1000°C and after 15 minutes the temperature was lowered within approximately one and a half hours to room temperature. The structure and phase purity of the materials obtained were checked by X-ray powder diffraction (XRD), using a PW 1729 Philips diffractometer, equipped in a Cu K_α X-ray source ($\lambda = 1.5418$Å), operating at 40 kV and 20 mA. The XRD patterns were found to be in good agreement with the theoretical patterns of cubic RbCl [27]. No additional peaks have been found that

could be assigned to a second crystalline phase. Also no peaks related to the starting materials were observed, indicating no segregation of the lanthanide dopants.

Due to hygroscopic nature of RbCl, samples were sealed in UV transparent plastic bags and were stored in a desiccator over a silica drying agent. During the measurements of the optical spectra, special care was taken in order not to expose the samples to air and moisture.

3.2.2. Optical Measurements

The luminescence spectra have been measured using synchrotron radiation at SUPERLUMI station (DESY, Hamburg). A detailed description of the set-up can be found in section 1.6 of this thesis as well as in REF. 28. The synchrotron spectra were measured in three time windows (integrated, fast and slow) making it possible to distinguish between fast and slow emissions. The fast time window was delayed by about 2 ns from the start of the excitation pulse and emissions falling within approximately the first 14 ns have been measured, while in the slow time window emissions present between about 100 and 200 ns were recorded. The time difference between the incoming bunches of excitation light was about 200 ns. Only in case of cerium activated material in case of the room temperature measurements the time difference between the incoming bunches was about 500 ns and the slow time window recorded emissions present in the range of about 350-500 ns. Luminescence decay curves were recorded using time correlated photon counting with a time resolution of ~ 200 ps. The excitation spectra were corrected for variation of the intensity as a function of wavelength using the excitation spectrum of sodium salicylate. The emission spectra were not corrected for detector response. The sample temperature could be varied between ~ 8 K and 320 K in a cold finger helium cryostat.

For luminescence lifetime measurements in the temperature range of 300-725 K a home-built heater was used to heat the sample and a picosecond pulsed diode exciting at 275 nm and a TimeHarp time correlated photon counting set-up were used for lifetime measurements. Simultaneously, high temperature emission spectra were recorded with Princeton Instruments CCD camera (cooled with liquid nitrogen) which was coupled to an Acton Research 0.25 m monochromator using an optical fiber. A grating blazed at 300 nm was used for the measurements.

3.3 RESULTS AND DISCUSSION

3.3.1. Undoped RbCl

To understand the luminescence properties of luminescent materials, it is important to investigate the optical properties of the undoped host lattice. Especially in the case of scintillator materials, where free electron-hole pairs are created under high energy excitation, it is well-known that recombination paths involving defect and trapped exciton states of the host lattice play an important role in the luminescence properties of doped materials. In order to investigate the host lattice as well as defect luminescence of RbCl, samples with two different morphologies have been investigated, namely as made, sintered material and a sample that has been crushed into a powder.

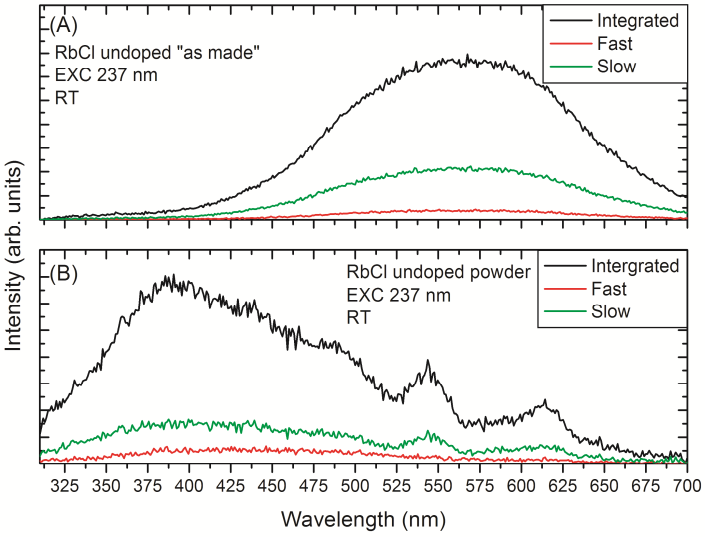

FIG. 3.1. Emission spectra of undoped RbCl at room temperature under 237 nm excitation. (A) shows the spectra for the "as made" sample, while (B) presents the spectra for the crushed powder sample.

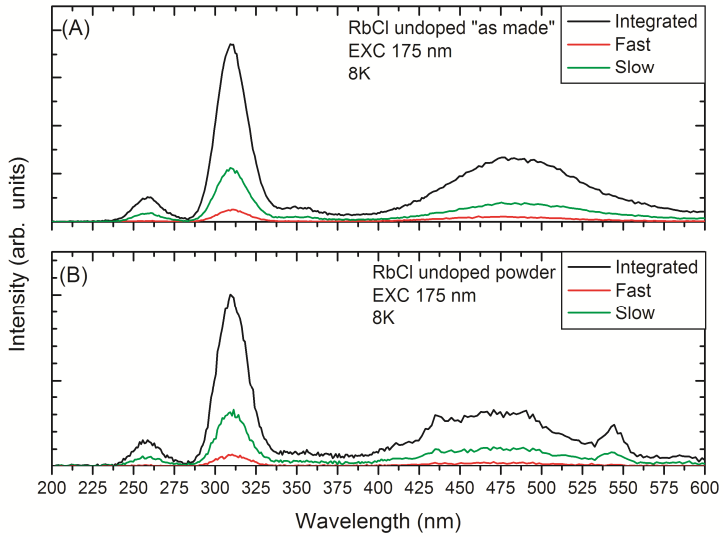

FIG. 3.2. Emission spectra of undoped RbCl at 8 K under 175 nm excitation. (A) shows the spectra for the "as made" sample, while (B) presents the spectra for the crushed powder sample.

Under sub-bandgap excitation in the UV, around 240 nm, the sample shows a broad emission around 560 nm in case of the as-made sample, and around 380 nm in case of the crushed powder material (FIG. 3.1). In the latter case there are also some sharper emission features present at about 545 nm and 620 nm. The bandgap of rubidium chloride is about 165 nm [29]. The observed emission for excitation at energies far below the band edge is related to defects or impurities. The strong change in the emission spectra after crushing the sample is further evidence that defects play a role in the emission process. Upon crushing, the surface to volume ratio increases and surface states will start to play a more prominent role in the emission process. When the rubidium chloride is excited at 175 nm (FIG. 3.2) (just below the bandgap, in the excitonic absorption peak), the emission spectra are dominated by three emission bands in the UV part of the spectrum, around 260 nm, 310 nm for both sample morphologies and around 480 nm and 460 nm in case of the as-made sample and the powdered sample, respectively. There is also a sharper emission peak present in the powder sample at about 545 nm.

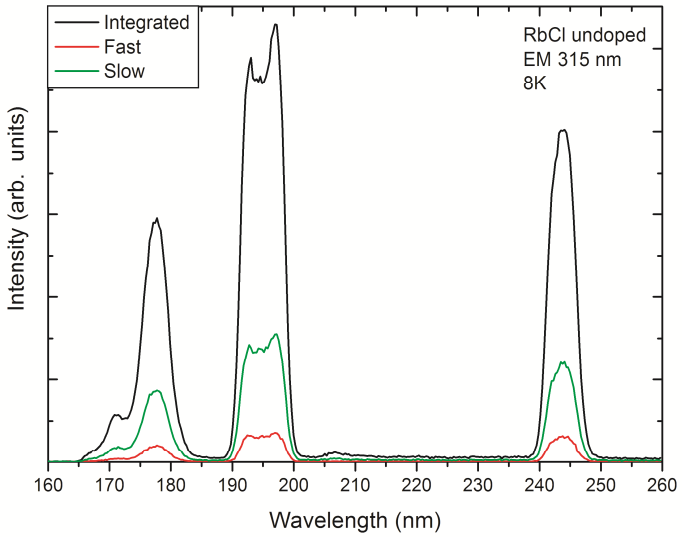

FIG. 3.3. Excitation spectra of undoped RbCl at 8 K recorded for the 315 nm emission.

In the excitation spectrum of the 315 nm emission (FIG. 3.3) three relatively narrow excitation bands are observed. These are located at 245 nm, 195 nm (with maxima at 192 nm and 197 nm) and 177 nm, with a shoulder at 170 nm. The peaks at 170 and 177 nm are attributed to excitonic absorptions as they are close to the band edge. The longer wavelength excitation and emission bands are related to defect structures in the lattice. Various V-centers have been identified in RbCl (and other alkali halides) with absorption bands in the UV and visible spectral region. The presently observed excitation bands around 195 and 245 nm are very sharp in comparison with V-center absorption bands observed at similar wavelengths in RbCl [30]. Broad emission bands in the UV and visible spectral region have been observed for RbCl, and also assigned to V-center recombination [30]. The nature of the various defect centers in RbCl and other alkali halides has been widely discussed. Since the analysis of the defect structure is not a scope of this study, no further analysis has been done on the undoped material. All the emissions discussed are observed in the slow time window, indicating that their decays are rather slow which makes it possible to distinguish them from fast *d-f* emission. Based on the results presented it is clear that the undoped RbCl shows interesting spectroscopic properties. Insight in the luminescence is important for understanding the luminescence of RbCl doped with Ce^{3+}, Pr^{3+} and Nd^{3+}.

3.3.2. *RbCl:Ce^{3+}*

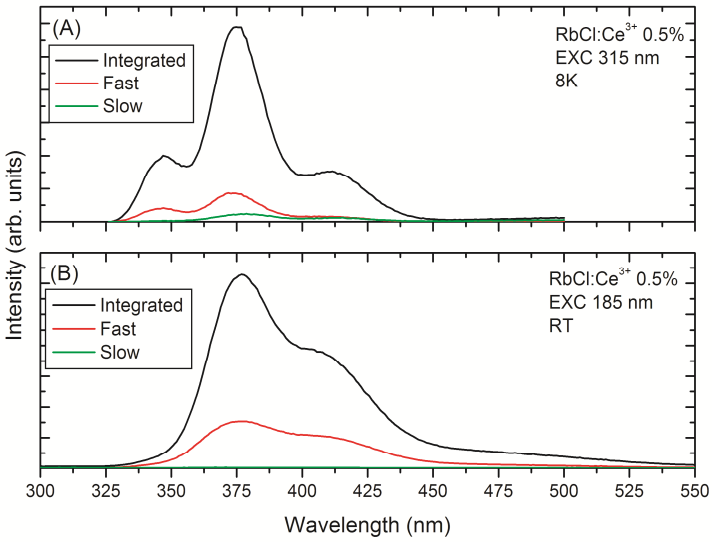

FIG. 3.4. Emission spectra of 0.5 % Ce^{3+} doped RbCl at 8 K under 315 nm excitation (A) and at room temperature under 185 nm excitation (B).

To incorporate Ce^{3+} on a Rb^{+} site in RbCl requires charge compensation due to the charge difference between Rb^{+} and Ce^{3+}. This will result in multiple Ce^{3+} sites with different luminescence properties due to variations in local charge compensation. In the emission spectrum more than the typical two emission bands (separated by about 2000 cm^{-1} due to the $^{2}F_{5/2}$-$^{2}F_{7/2}$ ground state splitting) commonly observed for Ce^{3+} on a single site can therefore be expected. In FIG. 3.4 emission spectra for RbCl:Ce^{3+} are shown for excitation at different wavelengths in the UV. For excitation at 315 nm three bands are observed in the emission spectrum, located at around 347, 375 and 412 nm at 8K (FIG. 3.4 A). The emission bands appear in the fast time window and are assigned to *d-f* emission from Ce^{3+}. Under 185 nm excitation (FIG. 3.4 B) emission bands are observed around 377 and 406 nm, the short wavelength emission is no longer observed. All emission bands are present in the fast time window. The wavelength of 185 nm is just below the bandgap of RbCl and is situated in the excitonic region. The observation of Ce^{3+} emission indicates that there is efficient energy transfer from the excitonic states to the Ce^{3+} *fd* states. The absence of the short wavelength emission band indicates that there is a preference of energy

transfer to the Ce^{3+} sites which give the lower energy emission. Alternatively, the short wavelength emission may be quenched at 300 K.

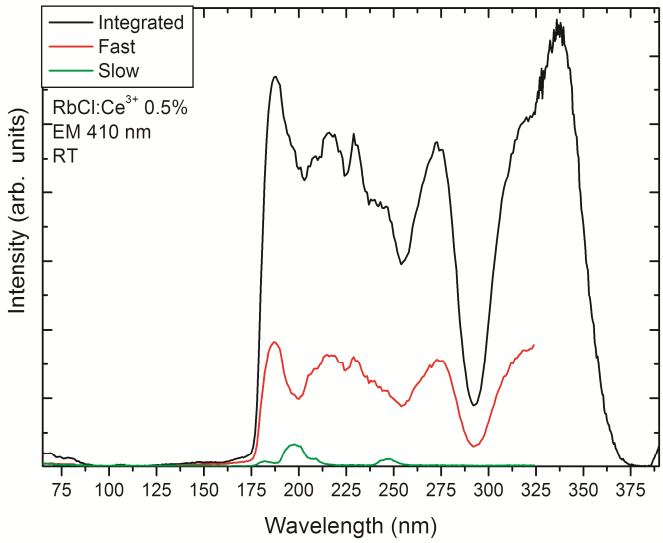

FIG. 3.5. Excitation spectra of 0.5 % Ce^{3+} doped RbCl at room temperature for the 410 nm emission.

In the excitation spectrum (FIG. 3.5), recorded for the Ce^{3+} emission at 410 nm, various broad bands can be observed between 175 nm and 375 nm. Since all the bands appear in the fast time window, it is concluded that they correspond to either *f-d* transitions on Ce^{3+} or excitonic transitions followed by fast energy transfer to Ce^{3+}. In the slow time window two weak bands at about 200 nm and 250 nm are observed. The wavelengths coincide with minima in the Ce^{3+} excitation spectrum. The features are assigned to host lattice excitation, probably related defect states. Observation in the slow time window indicates that energy transfer to Ce^{3+} is slow.

Under closer examination one can see a low intensity band at about 75 nm. This is assigned to the absorption due to transitions involving deeper lying core levels of the RbCl host lattice [24]. Core-level excitation (*5p* core-level→Valance Band (VB)) for RbCl has been observed before to occur below 85 nm in the excitation spectra of cross-luminescence in RbCl:Cs. In pure RbCl no cross-luminescence is observed due to quenching of the core-excitations through Auger recombination. The observation of the core-level excitation band in the excitation spectrum of the Ce^{3+} emission suggests that energy transfer to Ce^{3+}

can compete with Auger recombination, although the efficiency for energy transfer is low, as is clear from the low intensity of the core bands in the excitation spectrum.

Based on the positions of the *f-d* excitation bands and the corresponding *d-f* emission of the cerium ion, an estimate of the Stokes shift has been made. The lower energy excitation band has a maximum around 337 nm, while the corresponding emission from the lowest *5d* state to the $^2F_{5/2}$ ground state of Ce^{3+} is located around 375 nm. This gives a Stokes shift of about 3000 cm^{-1}. The presence of emission from multiple Ce^{3+} sites makes the estimate of the Stokes shift less accurate. The Stokes shift seems to fit in with the results for Ce^{3+} in alkaline metal chlorides series, where for the emission from Ce^{3+} in NaCl and KCl Stokes shifts of 6796 cm^{-1} and 2900 cm^{-1} have been reported, respectively [18]. Substitution on the much smaller cation site Na^+ results in a larger Stokes shift while for substitution of the large K^+ ion a similar Stokes shift is observed.

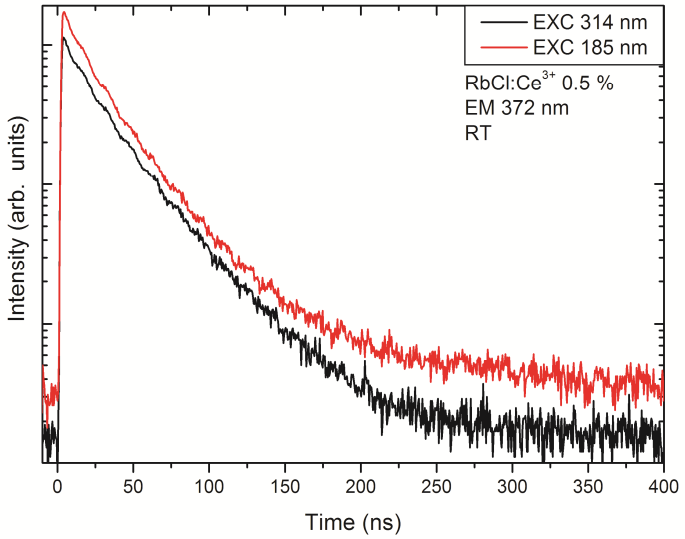

FIG. 3.6. Luminescence decay curves of the 0.5% Ce^{3+} doped RbCl, recorded for the 372 nm emission under 314 nm excitation (black curve) and 185 nm excitation (red curve) at room temperature.

The lifetime of the Ce^{3+} emission in RbCl has been measured under a direct *f-d* as well as under excitonic excitation (FIG. 3.6). The decay curves are close to single-exponential and the lifetimes observed under *f-d* and excitonic excitation are similar. For

the three emission bands observed at 8K, located at 347 nm, 377 nm and 411 nm, the lifetimes have been measured under a 315 nm excitation. For the short wavelength emission at 347 nm, the lifetime measured is 23 ns, while when the long wavelength emission at 411 nm is monitored, the lifetime is 41 ns. For the emission at 377 nm an intermediate lifetime of about 32 ns has been measured. The shorter lifetimes observed for the shorter wavelength emission bands are not only due to the higher energy of the emission (based on Fermi's Golden rule) but is probably also caused by energy transfer to Ce^{3+} sites emitting at lower energies. Based on these considerations, the longer wavelength emission is used to determine the radiative lifetime of Ce^{3+} emission in RbCl at 41 ns.

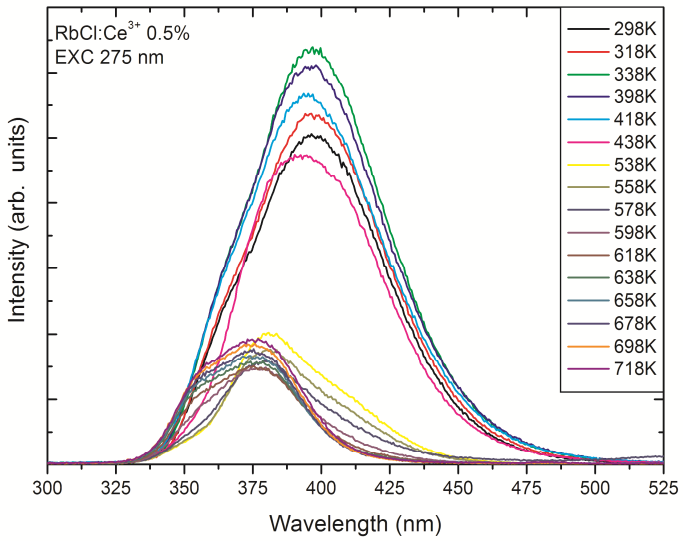

FIG. 3.7. Temperature dependent emission spectra of 0.5% Ce^{3+} doped RbCl under 275 nm excitation. Spectra recorded in the 298-718 K temperature range.

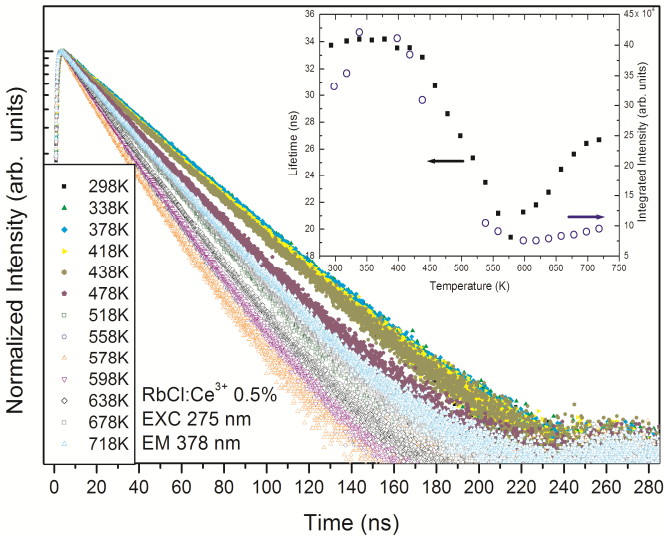

FIG. 3.8. Temperature dependent luminescence decay curves of 0.5% Ce^{3+} doped RbCl recorded for the 378 nm emission under 275 nm excitation. Luminescence decay curves were recorded in the 298-718 K temperature range. The inset shows a graphical representation of the change of the lifetime and the intensity of the emission with temperature.

The temperature dependent luminescence and lifetime measurements have been conducted in order to determine the quenching temperature of the Ce^{3+} luminescence in RbCl. Emission spectra measured between 298 and 725 K measured under identical circumstances are presented in FIG. 3.7. Luminescence decay curves for the same temperature range are shown in FIG. 3.8 close to the emission maximum (378 nm). In the inset in FIG. 3.8 the integrated luminescence intensity and the luminescence decay time (obtained from a single exponential fit) are plotted as a function of temperature. It should be noted that there is a gap in the data points for the luminescence spectra in FIG. 3.7 as well as the data points for the luminescence intensity in the inset of FIG. 3.8 around 47.5 K due to instrumental issues.

The luminescence spectra show that, after a small increase in intensity between 300 and 350 K, the luminescence intensity decreases and the longer wavelength emission is quenched when the temperature is raised above 400 K. Above 550 K only the emission at shorter wavelengths remains with maxima at ~ 355 nm and 380 nm. The luminescence lifetime measurements show a similar trend. The luminescence decay time decreases from 34 ns at 298 K to 20 ns at 550 K. Above 550 K the decay time increases again to 27 ns at

725 K. The results are consistent with the presence of multiple Ce^{3+} sites. The site(s) responsible for the longer wavelength emission show a clear temperature quenching with a $T_{1/2}$ of about 475 K. The site(s) giving the shorter wavelength emission do not show any quenching up to the highest temperatures investigated (725 K). The increase in the luminescence lifetime above 550 K is unexpected. It may be due to a contribution from a fast decay component from the partially quenched longer wavelength emission which is also present at 378 nm. When the longer wavelength emission is completely quenched, the decay curves reflect the radiative decay time of the emission from the shorter wavelength site. Alternatively, a higher crystal-field component of the *5d* state with a lower radiative decay rate may be thermally occupied at higher temperatures which can explain the lengthening of decay time. As the origin of the different Ce^{3+} sites is not known, it is not possible to explain the large difference in quenching temperature for the different Ce^{3+} sites in RbCl. For application as a scintillator material the temperature quenching above 400 K is not a problem since the operation temperature of scintillator crystals is below 400 K.

3.3.3. RbCl:Pr^{3+}

Faster *d-f* emission can be achieved by doping RbCl with Pr^{3+} instead of Ce^{3+}. The position of the *fd* excitation and emission bands can be estimated using the Dorenbos relation and the position of the lowest *fd* states of Ce^{3+} in RbCl. For Pr^{3+} the *fd* state is approximately 12 240 cm^{-1} higher in energy and thus the lowest *fd* band is expected around 240 nm in excitation and 260 nm in emission. In FIG. 3.9 mission spectra for RbCl:Pr^{3+} are shown for different excitation wavelengths. For excitation at 225 nm three broad bands are observed with maxima at about 269 nm, 283 nm and 307 nm. The bands are assigned to transitions from the lowest *fd* state to the $^3H_4$ ground level and the $^3H_5$ and $^3H_6$ levels, respectively (FIG. 3.9 A). There are weaker peaks at 487 nm, 544 nm and 586 nm which are assigned to intraconfigurational *f-f* transitions from the $^3P_0$ level to the $^3H_4$ ground level, $^3H_5$ and $^3H_6$ levels, respectively. For intraconfigurational *f-f* transitions one would expect sharp lines. The width of the lines is due to the poor instrumental resolution of the emission monochromator. The peak marked with an asterisk has not been assigned and may be due to an impurity. For excitation in the excitonic region at 175 nm (FIG. 3.9 B) the emission spectrum consists of four broad bands at about 269nm, 283 nm, 307 nm and 350 nm. The first three correspond to the transitions from the lowest *fd* state and appear in the fast time window. Stronger emissions around 310 and 350 nm that dominate the slow time window are assigned to excitonic or defect related emission. The band around 310 nm was also observed for undoped RbCl. Additionally weak emission peaks related to the transitions within the Pr $4f^2$ configuration are observed. The presence of the Pr^{3+} *d-f*

emission indicates that there is an energy transfer from the excitonic state to Pr^{3+} *fd* states. Alternatively, the *d-f* emission can be explained by direct excitation into a higher *fd* state of Pr^{3+} around 175 nm. In any case, the low relative intensity of the *d-f* emission shows that energy transfer from the excitonic states to the *fd* states of Pr^{3+} is not efficient.

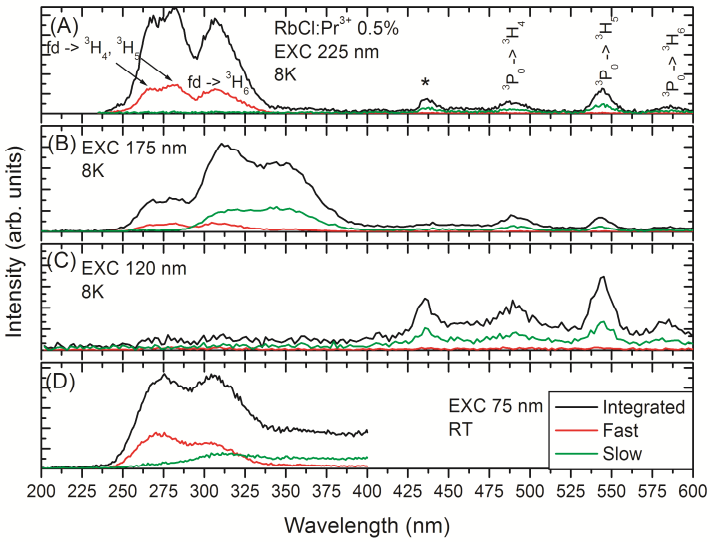

FIG. 3.9. Emission spectra of 0.5 % Pr^{3+} doped RbCl at 8 K under 225 nm excitation (A), 8 K under 175 nm excitation (B), 8 K under 120 nm excitation (C) and at room temperature under 75 nm excitation (D). Spectra were recorded in different time windows (integrated, fast and slow, see also text).

Under host lattice excitation at 120 nm (FIG. 3.9 C), no *d-f* emission of Pr^{3+} is observed. Only the *f-f* emissions are observed in the region from 475 nm to 575 nm as well as a very weak host lattice emission at around 300 nm. The lack of praseodymium *d-f* emission is explained by the absence of spectral overlap between the host lattice emission and the Pr^{3+} *f-d* absorption bands. Even shortest wavelength emission band observed in undoped RbCl around 260 nm (FIG. 3.2) is at too long wavelengths to overlap with the Pr^{3+} *f-d* absorption band. Excitation at even higher energies into core-level states around 75 nm does result in *d-f* emission from Pr^{3+}. The emission spectrum in FIG. 3.9 D shows emission bands between 250 and 330 nm that dominate in the fast time window and are similar to the *d-f* emission observed under direct excitation into the *fd* state (FIG. 3.9 A). In addition a broad and slow emission is observed between 300 and 400 nm which can be assigned to host lattice related emission.

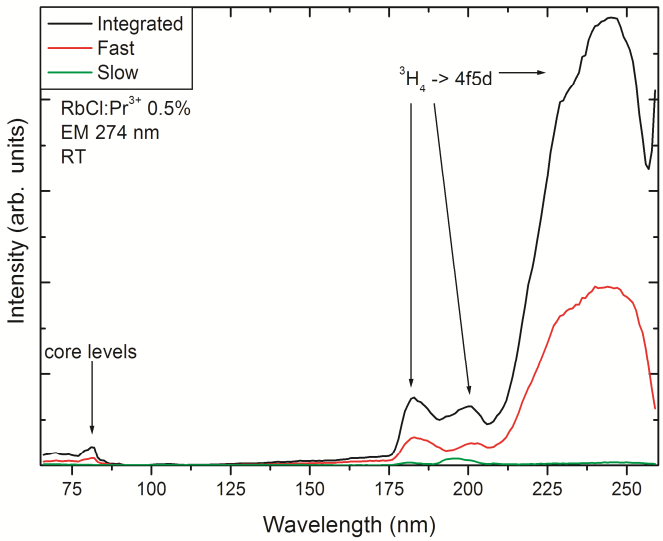

FIG. 3.10. Excitation spectra of 0.5 % Pr^{3+} doped RbCl at room temperature for the 274 nm emission.

The excitation spectrum of the Pr^{3+} *d-f* emission at 274 nm is shown in FIG. 3.10. The spectrum is characterized by a strong band with a maximum at 240 nm and a shoulder at 220 nm and two weaker bands at 200 nm and 185 nm. The bands are assigned to *f-d* transitions on Pr^{3+}. The position of the lowest energy band is in agreement with the position predicted based on the position of the lowest *f-d* excitation band for Ce^{3+} and the shift predicted by the Dorenbos model. The higher bands around 185 and 200 nm may also contain contributions from excitonic transitions in this spectral region. Excitation at energies higher than the bandgap (wavelengths shorter than 175 nm) does not result in *d-f* emission, in agreement with the emission spectrum shown in FIG. 3.9 C. This shows that energy transfer from the host lattice to the *fd* state of Pr^{3+} is not efficient in RbCl. Only upon excitation into the core levels (at wavelengths shorter than 85 nm) weak *d-f* emission can be observed. The absence of *d-f* emission for excitation over the bandgap is due to the inefficient energy transfer from the host lattice to the *fd* states of Pr^{3+}, as discussed above. For application as a fast and efficient scintillator material efficient feeding of the emitting *fd* state upon host lattice excitation is crucial. The presently observed low transfer efficiency makes RbCl:Pr^{3+} not a promising scintillator material.

For lower energy excitation, below the Pr^{3+} *fd* band, luminescence is still observed from RbCl:Pr^{3+} due to defect states in the material. Upon excitation at 358 nm there is a broad band defect emission present, located at 420 nm with a tail on the long wavelength

side up to about 560 nm. In the emission band three distinctive dips are observed at 449 nm, 473 nm and 485.5 nm (FIG. 3.11). These dips are explained by re-absorption of the emitted light by transitions within the *4f* shell of Pr^{3+} and are resonant with transitions from the $^3H_4$ ground state to the $^3P_2$, $^1I_6$ / $^3P_1$ and $^3P_0$ levels, respectively. The appearance of dips in the emission spectrum indicates that there is a radiative energy transfer from the defect to the praseodymium $4f^2$ levels.

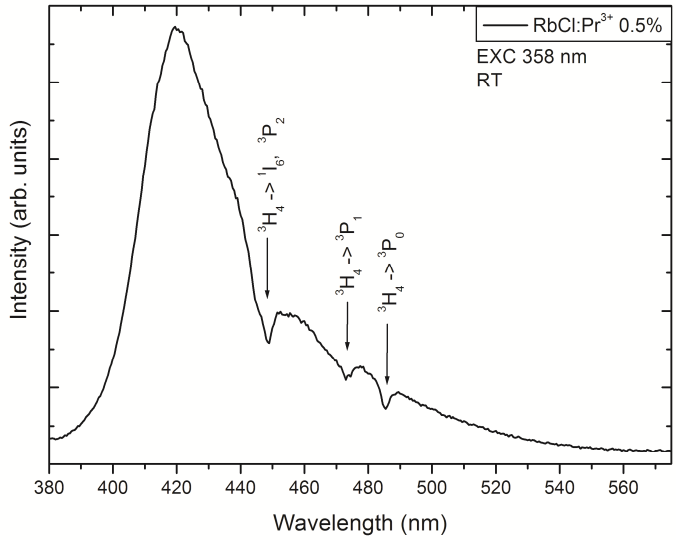

FIG. 3.11. Emission spectrum of 0.5 % Pr^{3+} doped RbCl at RT under a 358 nm excitation. The arrows indicate the positions of the $^3H_4 \rightarrow {}^3P_J, {}^1I_6$ absorption of Pr^{3+}.

To determine the radiative lifetime of the *d-f* emission for Pr^{3+} in RbCl, luminescence decay curves were recorded for different excitation wavelengths and at different temperatures. The results are collected in FIG. 3.12. The decay curves show a close to single exponential decay. The luminescence lifetime is hardly influenced by the excitation wavelength (direct *f-d* or excitonic excitation) or by the temperature (in the investigated temperature range of 9-300 K). The observation that the decay time does not vary up to 300 K indicates that there is no temperature quenching at temperatures below 300 K. The measured lifetime of the Pr^{3+} *d-f* emission is about 17 ns and is considered to be the radiative lifetime. The measured lifetime is about two times shorter than the lifetime for the Ce^{3+} *d-f* emission and is in agreement with the expected radiative lifetime. Typically, the radiative lifetime is between 10 and 20 ns for Pr^{3+} *d-f* emission around 270 nm [31,32]. In a future study we will discuss the wavelength dependence and host

lattice dependence of the decay time for *d-f* emission from Pr^{3+} in more detail [31]. For the decay curves recorded for 175 nm excitation there is also a faster decay component present of about 6 ns. This may be due to emission from Pr^{3+} close to a defect site to which energy transfer occurs. The 17 ns decay time of the emission is favorable for application as a scintillator material but due to the inefficiency of transfer from host lattice excitations to the emitting *fd* levels, RbCl:Pr^{3+} is not a promising scintillator material.

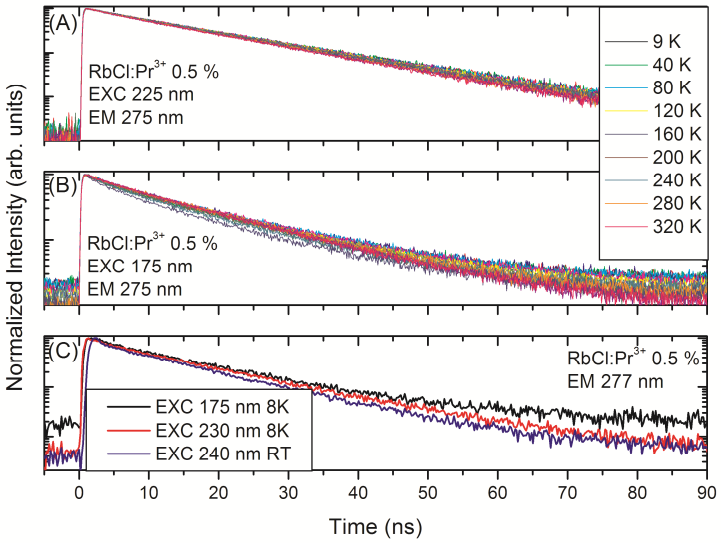

FIG. 3.12. Temperature dependent luminescence decay curves of the 0.5% Pr^{3+} doped RbCl, recorded for the 275 nm emission under 225 nm excitation (A) and 175 nm excitation (B). (C) shows luminescence decay curves recorded for the 277 nm emission under different excitation wavelengths at room temperature and 8 K.

3.3.4. RbCl:Nd^{3+}

The observation of *d-f* emission from Nd^{3+} is rare. The proximity of high energy $4f^3$ states gives rise to fast phonon relaxation and quenches *d-f* emission from Nd^{3+}. The position calculated for the $4f^2 5d$ state of Nd^{3+} using the position of the Ce^{3+} excitation and emission band, the *fd* state is around 50 000 cm^{-1} (200 nm) and emission from the $4f^2 5d$ state may be observed if it is located just below the $^2G_{9/2}$ level of Nd^{3+} around 48 000 cm^{-1}. The energy gap to the next lower $4f^3$ level $^2F(2)_{7/2}$ is 8000 cm^{-1} and is not expected to be

bridged by multi-phonon relaxation in a chloride host. Emission spectra were recorded for RbCl:Nd^{3+} under 175 nm excitation, as well as under a 210 nm excitation. Upon excitation at 210 nm, an emission band is observed around 220 nm (FIG. 3.13). The intensity is low and the emission is only observed at 7 K. The quenching temperature has not been investigated.

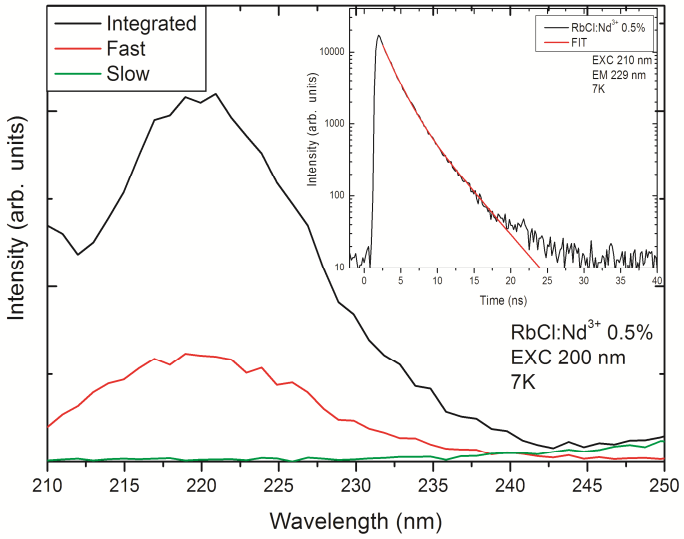

FIG. 3.13. Emission spectra of 0.5% Nd^{3+} doped RbCl under 200 nm excitation at 7 K. The inset shows the luminescence decay curve of 0.5% Nd^{3+} doped RbCl for the 229 nm emission under a 210 nm excitation.

The luminescence decay curve recorded for the 220 nm emission is depicted in the inset in FIG. 3.13. The decay time is short, approximately 4 ns. Even though the emission is expected to be fast, the observed lifetime is shorter than expected for *d-f* emission from Nd^{3+}. The low luminescence intensity and fast decay suggest that luminescence quenching occurs already at low temperatures. Since the position of the emission band and the nanosecond lifetime of the emission are consistent with *d-f* emission from Nd^{3+}, we assign the band around 220 nm to *d-f* emission from Nd^{3+}. The emission wavelength is somewhat longer than calculated with the Dorenbos formula (220 nm vs. 205 nm) but this may be explained by the presence of different types of charge compensated sites. The observed *d-f* emission may originate from a Nd^{3+} site for which the *fd* state is shifted to lower energies due to local charge compensation. The quenching of the emission at higher temperatures is

probably due to thermally activated photoionization from the lowest *fd* state to the conduction band. Thus, there is no *d-f* luminescence of Nd^{3+} at room temperature. The absence of neodymium *d-f* luminescence for bandgap excitation is explained by the high energy position of the *fd* state which prevents energy transfer from the host lattice to the *fd* states of Nd^{3+}.

3.4 CONCLUSIONS

Trivalent lanthanide ions have been incorporated into the RbCl host lattice. Fast *d-f* emission has been observed for Ce^{3+} and Pr^{3+} and possibly for Nd^{3+} ions in RbCl. For Ce^{3+} *d-f* emission is observed between 330 and 430 nm and originates from multiple charge-compensated sites. The luminescence lifetime for the long wavelength emission is about 41 ns. For Pr^{3+} *d-f* emission is situated between 250 and 340 nm and has a much shorter lifetime of approximately 17 ns. In RbCl:Nd^{3+} a short lived emission (τ = 4 ns) is present around 220 nm which may be due to *d-f* emission from Nd^{3+}. In all cases, *d-f* emission is only observed under excitation in the *fd* states. Excitation at energies higher than the bandgap does not yield fast *d-f* emission which is explained by inefficient energy transfer from host lattice excited states to the *fd* states of Ce^{3+}, Pr^{3+} and Nd^{3+}. Due to this inefficient energy transfer, RbCl:Ln^{3+} will not be an efficient scintillator material.

REFERENCES

[1] E. Zych, in: H. Singh Nalwa and L. Shea Rohwer (Eds.), *Handbook of Luminescence, Display Materials, and Devices* vol. 2, American Scientific Publishers, 2003, pp. 251

[2] C.R. Ronda, A.M. Srivastava, in: C. R. Ronda (Ed.), *Luminescence: From Theory to Applications*, Wiley-VCH Verlag, 2008, pp. 105

[3] M.R. Farukhi, C.F . Swinehart. *IEEE Trans. Nucl. Sci.* **NS-18**, (1971) 200

[4] E.V.D. van Loef, P. Dorenbos, C.W.E. van Eijk, K.W. Krämer, H.U. Güdel, *Appl. Phys. Lett.* **77** (2000) 1467

[5] K.S. Shah, J. Glodo, M. Klugerman, W.W. Moses, S.E. Derenzo, M.J. Weber, *IEEE Trans. Nucl. Sci.* **NS-50** (2003) 2410

[6] K.S. Shah, J. Glodo, M. Klugerman, L. Cirignano, W.W. Moses, S.E. Derenzo, M.J. Weber, *Nucl. Instrum. Methods A.* **505** (2003) 76

[7] E.V.D. van Loef, P. Dorenbos, C.W.E. van Eijk, K.W. Krämer, H.U. Güdel, *Nucl. Instrum. Methods A* **486** (2002) 254

[8] A. Bessiere, P. Dorenbos, C.W.E. van Eijk, K.W. Krämer, H.U. Güdel, C. de Mello Donegá, A. Meijerink, *Nucl. Instrum. Methods A* **537** (2005) 22
[9] E.V.D. van Loef, P. Dorenbos, C.W.E. van Eijk, K.W. Krämer, H.U. Güdel, *Nucl. Instrum. Methods A* **496** (2003) 138
[10] M.D. Birowosuto, P. Dorenbos, J.T.M. de Haas, C.W.E. van Eijk, K.W. Krämer, H.U. Güdel, *J. Lumin.* **118** (2006) 308
[11] A. Zych, C. de Mello Donegá, A. Meijerink, *J. Lumin.* **129** (2009) 1535
[12] A. Zych, A. Leferink op Reinink, K. van der Eerden, C. de Mello Donegá, A. Meijerink, *J. Alloy. Compd.* **509** (2011) 4445
[13] J. Selling, S. Schweizer, M.D. Borowosuto, P. Dorenbos, *J. Appl. Phys.* **102** (2007) 074915-1
[14] O.T. Antonyak, I.V. Kityk, N.S. Pydzyrailo, *Opt. Spectrosc.* **63** (1987) 529
[15] W.M. Li, M. Leskelä, *Mater. Lett.* **28** (1996) 491
[16] S.H.M. Poort, A. Meijerink, G. Blasse, *J. Phys. Chem. Solids* **58** (1997) 1451
[17] P. Dorenbos, in: S. Tavernier et al. (Eds.), *Radiation Detectors for Medical Applications*, Springer, 2006, pp. 191
[18] P. Dorenbos, *J. Lumin.* **91** (2000) 155
[19] E. Zych, C. Brecher, *J. Alloys Compd.* **300-301** (2000) 495
[20] W. Drozdowski, T. Lukasiewicz, A. J. Wojtowicz, D. Wisniewski, J. Kisielewski, *J. Cryst. Growth* **275** (2005) e709
[21] C.W.E. van Eijk, J. Andriessen, P. Dorenbos, R. Visser, *Nucl. Instrum. Methods A* **348** (1994) 546
[22] H. H. Li, *J. Phys. Chem. Ref. Data 5* (1976) 329
[23] A.S. Voloshinovskii, M.S. Mikhailik, V.B. Mikhailik, E.N. Mel'chakov, P.A. Rodnyi, C.W.E. van Eijk, G. Zimmerer, *J. Lumin.* **79** (1998) 107
[24] A. Voloshinovskii, *Radiat. Meas.* **33** (2001) 565
[25] R. D. Shannon, *Acta Cryst.* **A32** (1976) 751
[26] P.K. Manimozhi, G. Muralidharan, *Nucl. Instrum. Methods B* **267** (2009) 807
[27] PDF (Powder Diffraction File) # 01-089-3623
[28] G. Zimmerer, *Nucl. Instrum. Methods A* **308** (1991) 178
[29] S.B.S. Sastry, S. Sapru, *Physica B+C* **103** (1981) 324
[30] E.M. Winter, D.R. Wolfe, R.W. Christy, *Phys. Rev.* **186** (1969) 949
[31] A. Zych, M. de Lange, C. de Mello Donegá, A. Meijerink, to be published, see also Chapter 6
[32] C. Pedrini, D. Bouttet, C. Dujardin, B. Moine, H. Bill, *Chem. Phys. Lett.* **220** (1994) 433

4

Luminescence properties of lanthanide doped alkaline earth chlorides under (V)UV and X-ray excitation

ABSTRACT

The photoluminescence and radioluminescence of Ce^{3+}, Pr^{3+} and Nd^{3+} in $SrCl_2$ and $BaCl_2$ are reported and discussed in relation to application as a (fast) scintillator material. The Ce^{3+} doped materials exhibit the typical fast cerium *d-f* emission (358, 382 nm in $SrCl_2$ and 350, 375 nm in $BaCl_2$) both under synchrotron and ionizing radiation excitations. A weak afterglow is observed. For Pr^{3+} a very fast *d-f* emission is observed in $SrCl_2$ (250, 263, 300 and 328 nm, τ = 13 ns) and $BaCl_2$ (260, 288, 315 nm, τ = 10 ns), but only under direct *f-d* excitation. No *d-f* luminescence is observed for Pr^{3+} under X-ray excitation. The absence of *d-f* emission is explained by the energy of the host lattice emission which is too low for energy transfer to the high energy *fd* states of Pr^{3+} (230 nm in $SrCl_2$ and 235 nm in $BaCl_2$). The neodymium doped chlorides do not show *d-f* luminescence.

4.1 INTRODUCTION

Inorganic materials doped with lanthanide ions are well-known for their efficient luminescence related to the unique optical properties of the lanthanides originating from the partially filled *4f* shell. As a result, lanthanide doped materials are widely used in applications where efficient emission of light is required, for example in lighting (fluorescent tubes, white light LEDs), displays and medical imaging. In the field of medical imaging there has been great interest in the past decades in the development of new scintillation materials for the conversion of high energy X-rays or gamma-rays into light. Mostly, scintillators are inorganic crystalline materials (e.g. halides, oxides, silicates, aluminates, tungstates), which emit short flashes of light in the UV-Vis spectral range upon high energy radiation or particle irradiation. There are some stoichiometric scintillators known but most scintillators rely on emission from luminescent ions (activators) doped into the host lattice. The high energy radiation is deposited in the host lattice where it leads to the creation of electron-hole (e-h) pairs which recombine on or nearby the activator ion giving rise to efficient emission from the activator. Scintillators are of increasing interest due to a rise in the need for high energy radiation detectors, e.g. in high energy physics, space exploration, home land security and medical imaging. In the field of medical imaging scintillators are applied in positron emission tomography (PET), computed tomography (CT) and other X-ray imaging techniques and single photon emission computed tomography (SPECT). In the more advanced medical imaging techniques (PET, CT) better scintillators will lead to an increase in the precision of measurements to diagnose cancer earlier and to pinpoint the location of the tumor tissue in the patient's body, as well as decrease the exposure of the patients to the harmful ionizing radiation used in these examinations. The price of the scintillator materials used in these medical imaging machines is an important factor. PET is the technique with the most demanding requirements on the scintillators [1,2]. The emission must not only be efficient (preferably the scintillator material should generate at least 20 000 photons per MeV of incoming radiation) but also very fast, with the emission lifetime shorter than 40 ns, since the technique relies on the co-incident detection of gamma-rays emitted at an angle of 180 degrees upon positron-electron annihilation.

Efficient and fast emission is achieved by incorporation of trivalent Ce^{3+} ions ($4f^1$) in an inorganic host lattice. The 5*d*-4*f* (*d-f*) emission of Ce^{3+} is due to fully allowed (parity and spin) transition with a typical radiative lifetime of 25-70 ns. A wide variety of Ce^{3+} doped materials has been investigated for application in PET scanners. At the same time, it has been realized that an even faster response leads to a better timing resolution and better discrimination between random and real events, giving a higher spatial resolution. New materials with faster response time can use the *d-f* emission of Pr^{3+} ($4f^2$) or Nd^{3+} ($4f^3$). The

d-f emission from Pr^{3+} and Nd^{3+} is at higher energies which leads to faster radiative decay based on Fermi's golden rule [3,4].

Here we report the spectroscopic properties of Ce^{3+}, Pr^{3+} and Nd^{3+} in chloride host lattices. The choice for a chloride host is motivated by the recently reported high photon yields (> 80 000 photons/MeV) for Ce^{3+} in LnX_3 (Ln = La, Lu; X = Cl, Br, I) [5-8]. Possibly, incorporation of Pr^{3+} in a chloride host leads to a combination of a faster decay and high photon yield. Alkaline earth halides are known to show fast emission when doped with trivalent cerium ions [9-16]. Previous work on Ce^{3+} doped into alkaline earth chlorides has revealed Ce^{3+} *d-f* emission around 360 nm and 390 nm ($SrCl_2$) and 350 nm and 375 nm ($BaCl_2$), while the lowest *f-d* excitation bands are observed around 320 nm and 335 nm in strontium and barium chlorides, respectively [10-16]. No reports have been found in the literature on the luminescence of Pr^{3+} and Nd^{3+} in $SrCl_2$ or $BaCl_2$. Here we will show that Pr^{3+} shows fast *d-f* emission in both $SrCl_2$ and $BaCl_2$. Use of the materials as scintillators is however hampered by the absence of energy transfer from the host lattice to the emitting *fd* state.

4.2 EXPERIMENTAL

4.2.1. Synthesis and Characterization

The materials were synthesized by melting and rapid quenching of the starting materials (anhydrous chlorides) in a glassy carbon crucible in a high frequency furnace, similar to the method reported earlier for sodium chloride [17]. This allows for fast synthesis of simple chemical compositions even in the case of ionic radii and charge mismatch between the dopant and the host lattice cations. The samples obtained are polycrystalline. The mixture of anhydrous chlorides was dried over night at 200°C under a constant nitrogen flow. Then the temperature was raised to 300°C and maintained as such for 2 hours. Subsequently, melting at about 1000°C ($SrCl_2$) or 1100°C ($BaCl_2$) took place and after 15 minutes the melt was rapidly quenched to room temperature. The samples showed uniform red luminescence (in case of praseodymium doped host lattices) when observed under UV excitation (254 nm).

The crystal structure of the samples was checked by X-ray powder diffraction (XRD), using a PW 1729 Philips diffractometer, equipped in a Cu K_α X-ray source (λ = 1.5418Å). The XRD patterns of the compounds synthesized have been compared with the theoretical patterns of strontium chloride [18] and barium chloride [19]. Strontium

chloride can exist in several different crystal structures. The compounds that have been synthesized are cubic (a = b = c = 6.98 Å and α = β = γ = 90°), with a density of 3.09 g/cm^3. Barium chloride can also crystallize in various crystal structures depending on the synthesis conditions. The samples that were obtained were orthorhombic (a = 7.88 Å, b = 9.42 Å, c = 4.73 Å and α = β = γ = 90°), with a density of 3.94 g/cm^3. The strontium chloride materials show some additional peaks in the XRD patterns. This is attributed to the hygroscopicity of the material, which results in structural change due to incorporation of water and creation of different hydrates of strontium chloride, possibly during the collection of the XRD pattern.

4.2.2. Optical Measurements

Luminescence spectra have been measured using synchrotron radiation at SUPERLUMI station (DESY, Hamburg) which is an excellent station for vacuum UV (VUV) spectroscopy. A more elaborate description of the set-up can be found in section 1.6 of this thesis as well as in REF. 20. In short, the VUV part of the synchrotron spectrum is dispersed in an excitation monochromator giving the option to measure high resolution excitation spectra between ~ 65 and 335 nm, with a 0.3 nm resolution. Emission can be coupled into different monochromator / detector combinations, allowing for the measurement of emission between 120 and 1 000 nm. The synchrotron spectra have been measured in three time windows (integrated, fast and slow) making it possible to distinguish between fast and slow emissions. Luminescence lifetimes have been recorded with a timing resolution of about 200 ps using time-to-amplitude conversion (TAC). The excitation spectra have been corrected for signal intensity distribution with a spectrum of sodium salicylate. The emission spectra were not corrected for detector response. The samples have been placed in a cold finger cryostat on a copper sample holder.

Emission measurements under soft-X-ray excitation (radioluminescence) have been carried out at room temperature, using the white spectrum of a copper tube operated at 40 kV, with the energy in the maximum of the white band of about 28.7 keV. Afterglow of the investigated materials has been measured as well, using the same set-up.

Due to the hygroscopic character of the materials investigated, special care was taken to prevent incorporation of water. The samples were stored in sealed plastic bags that were UV transparent. Additionally, the samples have been stored in a desiccator above dry silica beads. Only in case of XRD and synchrotron measurements the samples were taken out of the protective bags. The XRD patterns were recorded under ambient conditions which can explain the observation of small lines related to hydrated phases in some cases.

4.3 RESULTS AND DISCUSSION

4.3.1. Luminescence Spectroscopy

4.3.1.1. Undoped $SrCl_2$ and $BaCl_2$

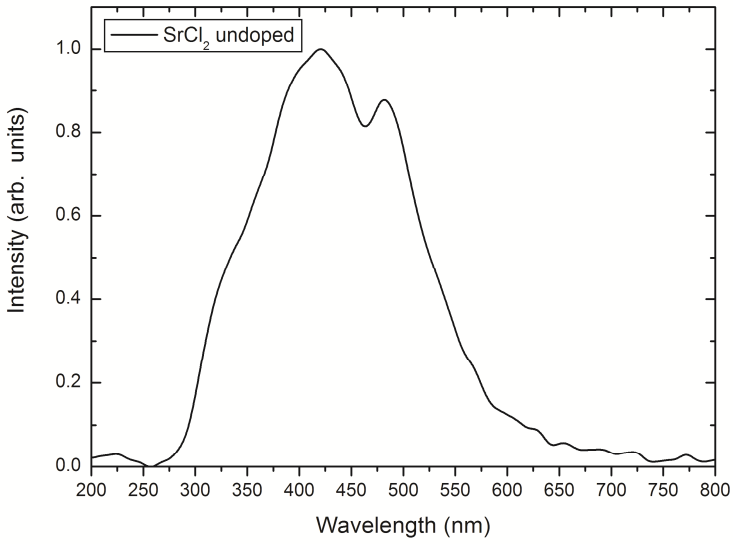

FIG. 4.1. Emission spectrum of undoped $SrCl_2$ under X-ray irradiation (26.7 keV), recorded at 300 K.

The bandgaps reported in the literature for $SrCl_2$ and $BaCl_2$ differ slightly and have been estimated to be 7.5 eV (165 nm) and 7.0 eV (177 nm) for strontium chloride and barium chloride, respectively [21]. The estimate is only approximate, since the bandgap depends on the crystal structure, which has not been mentioned in the cited reference [21]. The luminescence of the undoped barium chloride has been extensively studied in the past [22,23]. Two major emission bands are observed with maxima at around 310 nm and 450 nm. The former has been ascribed to the STE emission and occurs only under excitation in the excitonic absorption peak [22], while the latter has been assigned to the F-V_k center recombination [23]. However, no reports on the spectroscopic properties of the undoped $SrCl_2$ host lattice have been found in the literature. In FIG. 4.1 a typical spectrum

of the undoped $SrCl_2$ host lattice under X-ray excitation is presented. Two major emission bands are observed, peaking at around 420 nm and 483 nm. There is an additional small intensity band present around 225 nm and a shoulder to the main emission band at 420 nm, which is located at around 328 nm. The exact origin of these bands has not been investigated, though the small intensity band at around 225 nm might be an STE emission, while the main broad emission band at 420 nm could be related to the V_k center radiative recombination, analogues to that observed for $BaCl_2$. Since the crystal structure of both the materials is different, the observed features would be located at different wavelengths. The broadened peak at about 480 nm might also be a defect of some sort.

4.3.1.2. Ce^{3+} doped $SrCl_2$ and $BaCl_2$

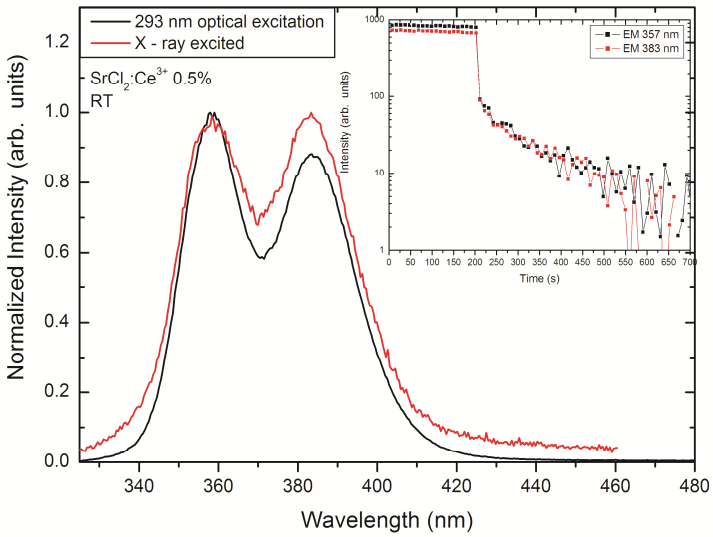

FIG. 4.2. Emission spectra of $SrCl_2:Ce^{3+}$ 0.5% under UV excitation (293 nm, black line) and under X-ray irradiation (26.7 keV, red line), at 300 K. The inset shows the afterglow curves for the 357 nm and 383 nm emissions after X-ray irradiation.

Strontium chloride has been doped with trivalent cerium ions and the luminescence spectra have been recorded under different excitation wavelengths. A typical emission spectrum is presented in FIG. 4.2. The black curve corresponds to the emission as observed under a 293 nm excitation. The emission spectrum shows two broad bands,

located at about 358 and 382 nm. The bands are assigned to transitions from the lowest *fd* state of Ce^{3+} to the $^2F_{5/2}$ and $^2F_{7/2}$ $4f^1$ ground state of Ce^{3+}. The observed energy separation between the two bands is about 1755 cm^{-1}, which is close to the expected spin-orbit splitting of 2000 cm^{-1}. It should be noted that in case of strontium chloride the trivalent cerium ions enter the divalent host lattice site. Due to the need of charge compensation multiple lanthanide sites occur in the sample and can also give rise to different emission wavelengths.

The emission lifetime has been measured under direct *f-d* excitation at 325 nm, monitoring the 340 nm Ce^{3+} *d-f* emission (FIG. 4.3). For 0.1% Ce sample a decay time of 26 ns is measured at 300 K.

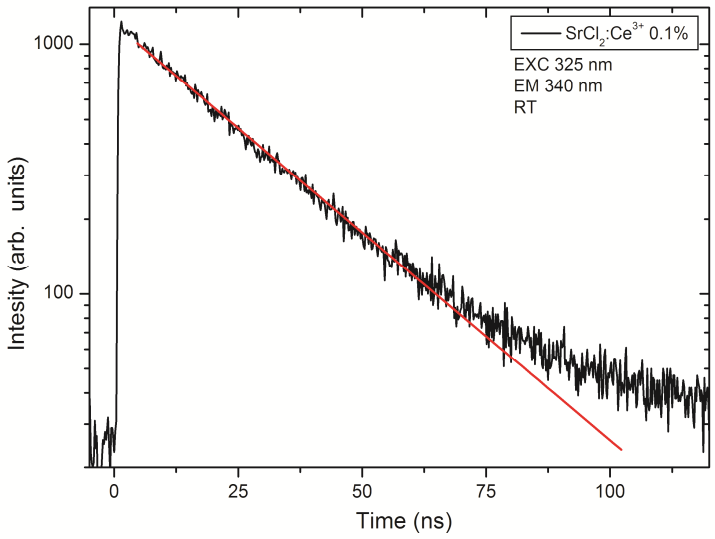

FIG. 4.3. Luminescence decay curve of the Ce^{3+} *d-f* emission (340 nm) in $SrCl_2$:Ce^{3+} 0.1% under direct excitation in the *fd* band (325 nm). The drawn line corresponds to a fit to single exponential decay with τ = 26 ns.

In $BaCl_2$ doped with Ce^{3+} the emission spectrum is similar to that for $SrCl_2$:Ce^{3+}. There is a slight blue shift of the emission bands, which are located around 350 and 375 nm for 295 nm excitation, as shown in FIG. 4.4 (black curve). The energy separation of the bands is about 1900 cm^{-1}, which corresponds well to the expected separation of 2000 cm^{-1}. Just as for $SrCl_2$, also for $BaCl_2$ differently charge compensated sites may influence the observed splitting in two bands. The results obtained for $BaCl_2$:Ce^{3+} are in line with earlier

reports in the literature [10-13]. Further comparison with the literature data will follow in the section on radioluminescence. The emission lifetime has been measured under a direct *f-d* excitation at 275 nm for 350 nm emission (FIG. 4.5). A single exponential fit gives a decay time of 19 ns.

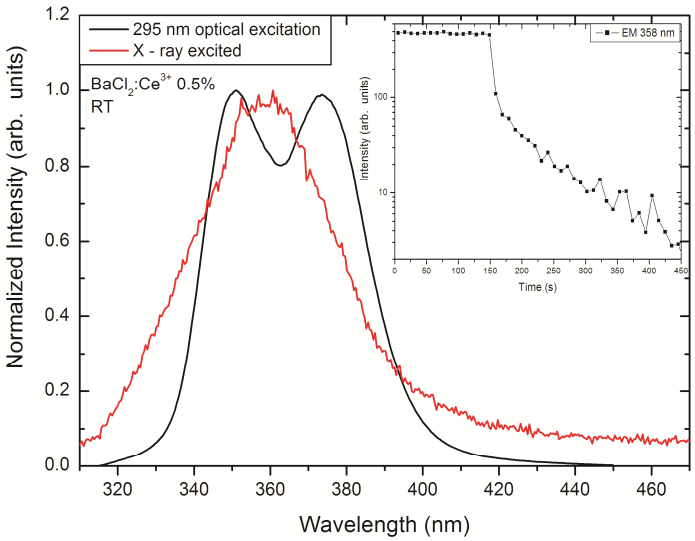

FIG. 4.4. Emission spectra of $BaCl_2$: Ce^{3+} 0.5% under UV excitation (295 nm, black line) and under X-ray irradiation (26.7 keV), at 300 K. The inset shows the afterglow curve for the 358 nm emission after X-ray irradiation.

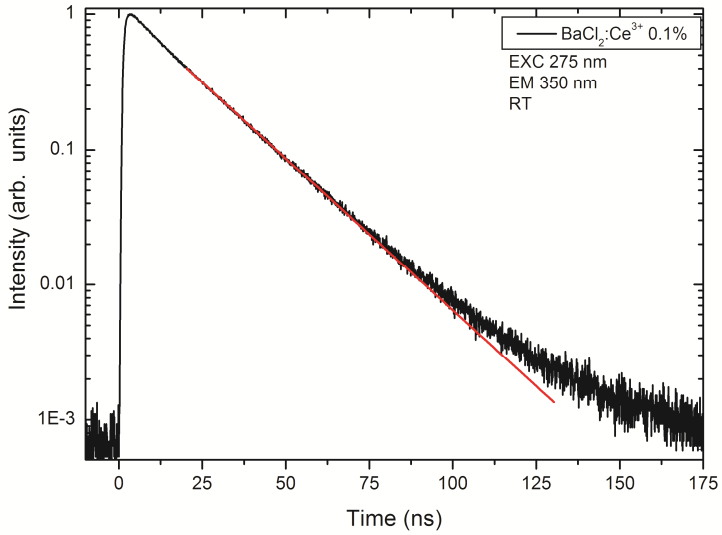

FIG. 4.5. Luminescence decay curve of the Ce^{3+} *d-f* emission (350 nm) in $BaCl_2$:Ce^{3+} 0.1% under direct excitation in the *fd* band (275 nm) at 8 K. The drawn line corresponds to a fit to single exponential decay with τ = 19 ns.

4.3.1.3. Pr^{3+} doped $SrCl_2$ and $BaCl_2$

Emission spectra were recorded for $SrCl_2$:Pr^{3+} under excitation at 165 nm (the excitonic absorption edge) and 236 nm (in the lowest energy *fd* band) at 8K (FIG. 4.6). Under direct excitation in the *fd* band (FIG. 4.6 A), four emission bands are observed, around 250, 263, 300 and 328 nm, as well as a very broad and low intensity band between 400 and 550 nm with maxima around 430, 460 and 490 nm. The broad band is assigned to a defect luminescence. Due to low resolution of the emission monochromator used, it is possible that the 490 nm maximum is in fact the $^3P_0 \rightarrow {}^3H_4$ transition on Pr^{3+}. The visible emission is stronger in the slow time window, indicating that the decay time is slower than ~ 100 ns. This is expected for defect-related emission at low temperatures. The emission bands in the UV part of the spectrum are stronger in the fast time window, indicating that these are the transitions from the lowest *f-d* state of Pr^{3+} which will have a fast (ns) decay time. The bands have been assigned to transitions from the lowest *fd* state to the $^3H_4$, $^3H_5$, $^3F_3$ and $^1G_4$ *4f* states of Pr^{3+} for the bands located at 250, 263, 300, 328 nm, respectively. The separation between the bands agrees well with the known energy differences between the $^3H_4$, $^3H_5$, $^3F_3$ and $^1G_4$ states.

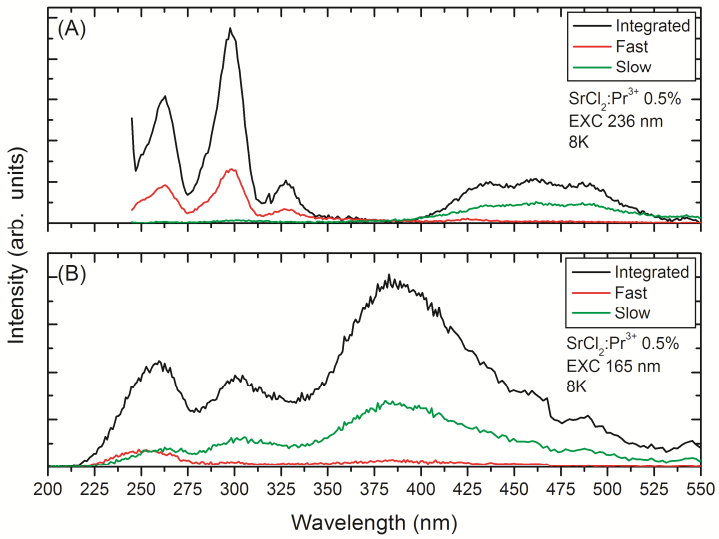

FIG. 4.6. Emission spectra of $SrCl_2:Pr^{3+}$ 0.5% for excitation into the host lattice at 165 nm (A) and direct excitation into the *fd* band of Pr^{3+} at 236 nm (B). The spectra were recorded in different time windows (fast, slow and integrated, see also section 2.2) at 8 K.

Under excitonic excitation at 165 nm (FIG. 4.6 B), the emission spectrum consists of three broad bands in the range 210 nm to about 550 nm. The maxima of the bands are located around 260 nm (with a small shoulder like feature at 237 nm), 300 nm and at 390 nm (with a tail extending to about 550 nm). The bands are stronger in the slow time window, indicating a long luminescence lifetime although some fast emission is observed between 240 and 320 nm. These UV emission bands may have a contribution from Pr^{3+} *d-f* emission. Feeding of the *fd* state through the excitonic state may also result in a longer lifetime for delayed *d-f* emission. The fact that the emission bands are broader than under direct excitation may be caused by broadening resulting from differently charge compensated Pr^{3+} sites, which are excited non-selectively under excitonic excitation. However, also defect related emission from the $SrCl_2$ host lattice has been observed in the spectral region around 300 nm. Due to the strong overlap it is hard to assign the UV emission bands to *d-f* or host lattice emissions. The strong emission band around 390 nm is assigned to defect emission. Its position is consistent with the bands observed in the emission spectrum of the undoped $SrCl_2$ host lattice under ionizing radiation excitation, presented in FIG. 4.1.

The lifetime of the praseodymium *d-f* emission in strontium chloride has been measured under a direct *f-d* excitation at 8K for a sample activated with 0.5% Pr^{3+}. The

decay curve is presented in FIG. 4.7. The decay is single exponential, with a decay time of 13 ns. This is much shorter than the decay times measured for Ce^{3+} emission and is promising for application as a scintillator material.

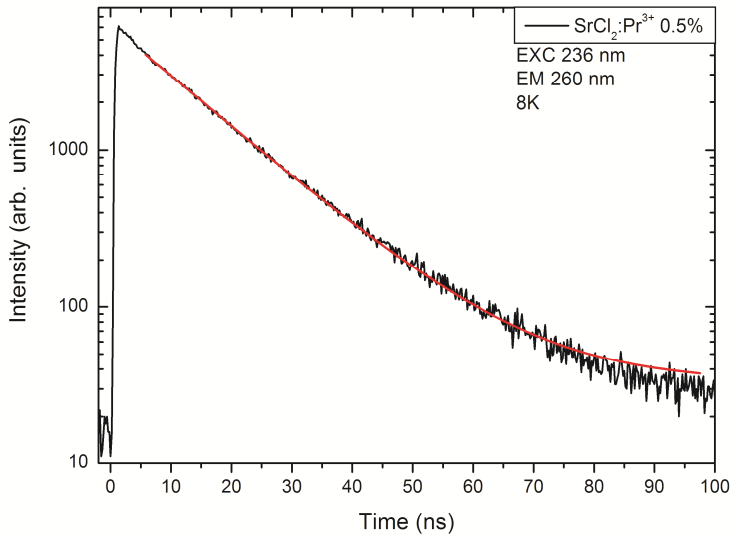

FIG. 4.7. Luminescence decay curve of the Pr^{3+} *d-f* emission (260 nm) in $SrCl_2$:Pr^{3+} 0.5% under direct excitation in the *fd* band (236 nm) at 8 K. The drawn line corresponds to a fit to single exponential decay with τ = 13 ns.

The emission spectra of Pr^{3+} in $BaCl_2$ (at 8K) are shown in FIG. 4.8 for two different excitation wavelengths, 168 nm (excitonic) and 230 nm (*f-d* excitation). Under a direct *f-d* excitation the emission spectrum consists of two sets of emission bands as shown in FIG. 4.8 A. The emissions in the UV part of the spectrum are located at around 260, 288 and 315 nm. These emission bands can be observed in the fast time window, indicating that they are related to the transitions from the lowest *fd* state to the $4f^2$ levels, $^3H_4$, $^3H_6$, $^3F_4$, respectively. The $fd \rightarrow {}^3H_5$ is not observed as a separate band, probably because it overlaps with the $fd \rightarrow {}^3H_4$ transition which is close in energy. It should be noted that the emission band that has been assigned to the $fd \rightarrow {}^3F_4$ transition overlaps with a slower decaying band around 310 nm. This indicates that there is an emission of different nature present at that wavelength that can also be excited at 230 nm, probably a host lattice related emission band. The emission bands between 350 nm and 500 nm are assigned to the defect related emissions. The small peak at 490 nm is probably $^3P_0 \rightarrow {}^3H_4$ emission of Pr^{3+}.

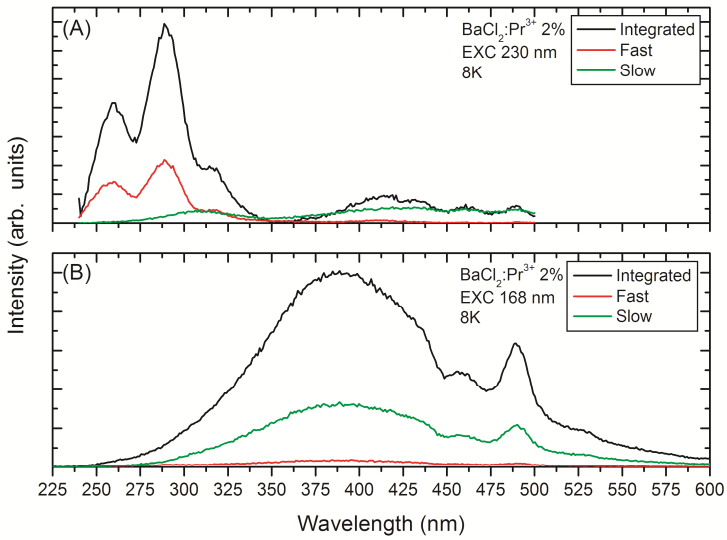

FIG. 4.8. Emission spectra of $BaCl_2:Pr^{3+}$ 2% for excitation into the host lattice at 168 nm (A) and direct excitation into the *fd* band of Pr^{3+} at 230 nm (B). The spectra were recorded in different time windows (fast, slow and integrated, see also section 2.2) at 8 K.

The emission spectrum of $BaCl_2:Pr^{3+}$ 2% under excitonic excitation at 168 nm (FIG. 4.8 B) shows a very broad band from about 240 to 600 nm, peaking at 390 nm. This band is assigned to the host lattice emission, as the one observed in the literature for $BaCl_2$ [22], similar to the band observed in $SrCl_2$. There is also a sharper spectral feature present at about 490 nm which is assigned to the $^3P_0 \rightarrow {}^3H_4$ emission. The presence of this emission demonstrates that there is energy transfer from the excitonic state to the *4f* levels of praseodymium. However, no transition from the lowest *f-d* state has been observed in the region between 250 and 300 nm, contrary to observation for $SrCl_2:Pr^{3+}$ where *d-f* emission from Pr^{3+} was observed after excitonic excitation, albeit weak. This indicates that there is no energy transfer from the host lattice excitonic state to the *fd* state of Pr^{3+} in $BaCl_2:Pr^{3+}$. An interesting spectral feature can be observed around 450 nm. The peculiar dip in the host lattice emission spectrum is a clear signature of radiative energy transfer to the praseodymium $^3P_2$ level. This will be followed by emission from the $^3P_0$ level to the $^3H_4$ ground state. In addition to radiative energy transfer there may also be non-radiative transfer. The praseodymium *d-f* emission lifetime in barium chloride has been measured at 8K under a direct *fd* excitation for the 2% doped sample. The luminescence decay curve is shown in FIG. 4.9. The decay curve has a non-exponential initial part followed by a more exponential tail. The tail has been fit to a single exponential which results in a decay time

of 10 ns. The non-exponential initial part can be explained by cross-relaxation quenching for neighboring Pr^{3+} ions. At 2% of Pr^{3+} it is known that cross-relaxation starts to depopulate the *fd* excited state. The tail represents the decay for isolated Pr^{3+} ions and the fit gives a reliable estimate of the radiative decay rate of the *fd* state. Some non-exponentiality may also be introduced by the presence of multiple sites with different local charge compensation. The 10 ns lifetime is among the shortest radiative lifetimes that have been reported for Pr^{3+} *d-f* emission. For example, the radiative lifetime for the *d-f* emission from Pr^{3+} in the scintillator material LuAG:Pr is 22 ns. The faster radiative decay rate in $BaCl_2$ is explained by the shorter emission wavelength (260 nm) and the higher refractive index of the material. The short decay time is favorable for application in PET scanners where a shorter radiative lifetime contributes to a better image quality.

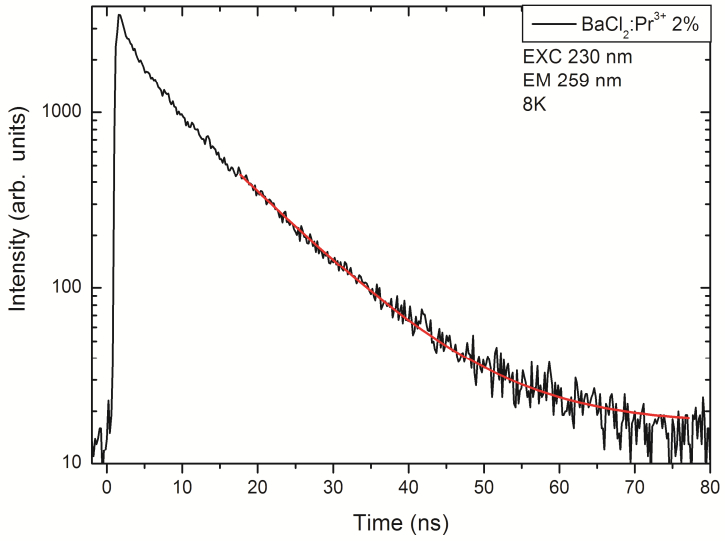

FIG. 4.9. Luminescence decay curve of the Pr^{3+} *d-f* emission (259 nm) in $BaCl_2$:Pr^{3+} 2% under direct excitation in the *fd* band (230 nm) at 8 K. The drawn line corresponds to a fit to single exponential decay for the tail of the curve with τ = 10 ns.

4.3.1.4. Nd^{3+} doped $SrCl_2$ and $BaCl_2$

The lowest energy *fd* level for Nd^{3+} in $SrCl_2$ is expected to be located around 185 nm based on the position of the *fd* level for Ce^{3+} in $SrCl_2$ and the shift of 22 720 cm^{-1} to

higher energy predicted by the Dorenbos relation [3]. The emission spectrum of neodymium doped strontium chloride only shows slow *f-f* emission, even when it is excited directly into the *fd* states (185 nm).

For $BaCl_2:Nd^{3+}$ the lowest *fd* state of Nd^{3+} is expected around 189 nm. Just as for $SrCl_2:Nd^{3+}$, no *d-f* luminescence is observed, even under a direct *f-d* excitation. Instead, there is feeding of the $4f^3$ states of neodymium and only the slow intraconfigurational emission could be observed.

A possible explanation for the lack of Nd *d-f* emission in both $SrCl_2$ and $BaCl_2$ is that the lowest energy *fd* band of Nd in these host lattices is at higher energies than host lattice excited states, leading to energy transfer from *fd* states to defect states, which in turn populate high energy $4f^3$ neodymium levels through energy transfer. It also cannot be excluded that the *fd* states of Nd^{3+} are located close to or in the conduction band of $SrCl_2$ and $BaCl_2$. In this case excitation in the *f-d* state results in an impurity trapped exciton state that can relax by feeding the lower lying $4f^3$ levels of Nd^{3+}, leading to the slow *f-f* emission.

4.3.2. Radioluminescence

Radioluminescence is an important tool in the investigation of potential scintillator materials. It allows to study the luminescence properties under X-ray excitation. Under high energy excitation the efficiency of energy transfer from the host lattice to the activator ion can be investigated along with the kinetics. Also the radiation stability can be evaluated for excitation with ionizing radiation. Finally, it allows for an evaluation of the overall scintillation efficiency and of (undesired) afterglow properties.

4.3.2.1. Ce^{3+} doped $SrCl_2$ and $BaCl_2$

Under ionizing radiation the Ce^{3+} emission for $SrCl_2$:Ce consists of two broad bands that are consistent in shape and spectral location with the spectra observed under UV excitation (see FIG. 4.2, red curve). This proves that the emission comes from Ce^{3+} in $SrCl_2$. The bands are located at 360 nm and 384 nm. Upon ending X-ray excitation afterglow was present and it could be measured (for the 0.5% doped sample) for up to about 8 minutes after removal of the excitation source. The recorded afterglow decay is presented in the inset of FIG. 4.2. The afterglow is related to the slow release of trapped charge carriers generated under X-ray excitation. Recombination of thermally released charge

carriers on or near the Ce^{3+} ions results in Ce^{3+} emission. Traps for free charge carriers may pre-exist in the material but the formation of traps can also be induced by the high energy irradiation.

A peculiar change in the relative intensities of the two Ce^{3+} emission bands was observed during irradiation. Both bands become weaker but the decrease in intensity of the longer wavelength band is much stronger. Probably this is due to the formation of color centers which absorb more strongly at the wavelength of the longer wavelength emission band. After prolonged irradiation the sample turns grayish indicating that color centers are formed.

The scintillation efficiency increased when the Ce^{3+} concentration was increased from 0.5% to 2%. The increase, based on the long wavelength band at 384 nm, is of about 40% for the 2% doped sample, compared to the 0.5% one. This is due to the larger number of Ce^{3+} ions available for excitation. By increasing the concentration of the activator ions, the probability of the excitation energy being captured by them increases. Otherwise the energy would have been lost through competing channels (e.g. recombination at trap sites).

Ce^{3+} emission in $BaCl_2$ has also been studied under ionizing radiation excitation. The emission spectrum consists of one broad band (red curve in FIG. 4.4), located around 358 nm. The position is similar to that observed under UV excitation but the characteristic doublet structure of Ce^{3+} emission has disappeared. The spectrum is also different from previous reports in the literature [10-13], where two emission bands have been observed under ionizing radiation excitation. Selling et al. have also observed a weak band around 300 nm that they have ascribed to the STE emission in barium chloride [12,23]. No such emission has been observed in the present study. The reasons for such a discrepancy are not clear. The single broad emission band around 358 nm has been observed for all samples, with Ce^{3+} concentrations of 0.1%, 0.5% and 2%. The origin of the change in the emission spectrum may be radiation induced defects. The softer $BaCl_2$ is more prone to the creation of defects than $SrCl_2$. Due to defect formation, the local environment of the Ce^{3+} ions changes and the disorder causes broadening of the Ce^{3+} emission bands, and therefore the 2000 cm^{-1} splitting can no longer be observed. This observation is in contrast to the results presented by Selling et al. [12], although it should be pointed out that in the cited reference the authors have used a different excitation source for X-rays. It is possible that the dose of the radiation was different in their case, which would lead to the observed difference, but this aspect has not been further investigated.

The afterglow of the Ce^{3+} emission in $BaCl_2$ under X-ray excitation has been measured for the 0.5% doped sample. The emission could be detected for up to 6 minutes after the excitation has been stopped. The resulting afterglow decay is presented in the inset of FIG. 4.4. Just as in case of $SrCl_2$:Ce^{3+} the afterglow is assigned to the slow thermally activated release of trapped charge carriers.

The highest scintillation intensity has been observed for the 2% doped sample and the intensity has increased in the concentration series from 0.1% to 2%. The increase when going from the 0.1% doped sample to the 0.5% doped one is of about 18%. When the concentration has been increased to 2%, the increase in the scintillation efficiency compared to the 0.1% doped sample has been about 62%. Just as in the case of $SrCl_2:Ce^{3+}$ this observation is explained in the terms of a greater number of activator ions available for excitation by the created electron-hole pairs (which number for a specific material and specific excitation is constant), leading to the increased probability that the excitation energy will reach the activators, leading to increased luminescence intensity.

4.3.2.2. Pr^{3+} doped $SrCl_2$ and $BaCl_2$

To investigate the efficiency of the fast *d-f* emission of Pr^{3+} under X-ray excitation, the emission spectrum of $SrCl_2:Pr^{3+}$ (0.5% and 2%) has been measured under X-ray excitation and is shown in FIG. 4.10. The spectrum consists of a broad band around 400 nm and two sets of sharp emission lines at about 490 nm and 600-650 nm. The broad band emission is consistent with the previously observed host lattice emission of $SrCl_2$. The sharp lines are assigned to the Pr^{3+} *f-f* emission. No Pr^{3+} *d-f* emission is observed. This indicates that the energy transfer from the electron-hole pairs created by the X-rays to the *fd* state of Pr^{3+} is inefficient. This is consistent with the VUV luminescence measurement discussed in the previous section. The host lattice emission is too low in energy and there is no spectral overlap with the *f-d* excitation bands of Pr^{3+}, which are situated at high energies. There is spectral overlap with the $4f^2$ excitation lines and as a result, there is partial energy transfer to the $4f^2$ levels (^3P_J) of Pr^{3+}, resulting in the *f-f* emission lines. The presence of host lattice emission in the spectrum of the 0.5% doped sample shows that at this dopant concentration there is only partial energy transfer from the host lattice to Pr^{3+}. To increase the energy transfer efficiency the Pr^{3+} concentration has been increased to 2%. This strongly reduces host lattice emission intensity, showing that the energy transfer from the host lattice is indeed more efficient, but also the Pr^{3+} emission intensity decreases by a factor of about 7. This is explained by the cross-relaxation quenching of the Pr^{3+} emission, which is well-known to occur at higher Pr concentrations and starts at Pr^{3+} concentrations as low as 0.5%.

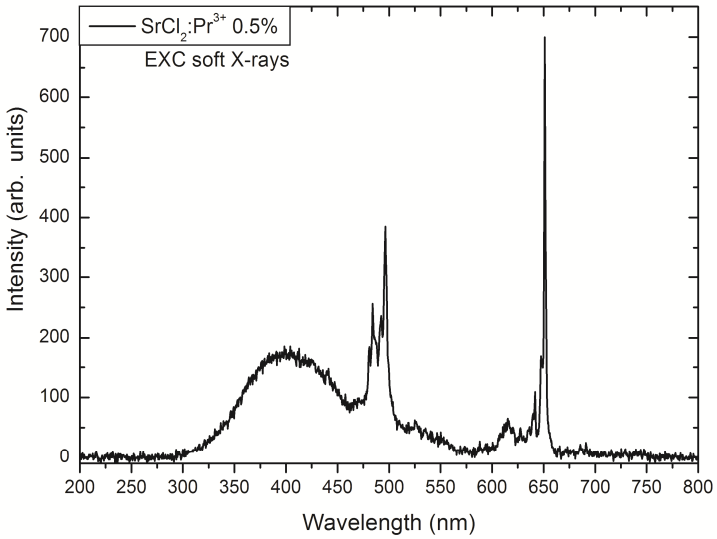

FIG. 4.10. Emission spectrum of $SrCl_2:Pr^{3+}$ 0.5% at 300 K under X-ray excitation Cu-source, operated at 40kV).

The Pr^{3+} emission in $BaCl_2$ under ionizing radiation excitation has been investigated by measuring the X-ray excited emission spectra for three samples with Pr^{3+} concentrations of 0.1%, 0.5% and 2%. The spectrum of the 0.5% doped sample is presented in FIG. 4.11 and shows line emission between 490-550 nm and 600-725 nm due to Pr^{3+} *f-f* emission. Just as for $SrCl_2$:Pr, no *d-f* emission is observed showing that there is only energy transfer from the host lattice excited states to the $4f^2$ states of Pr^{3+} and not to the *fd* states. A very low intensity band is observed around 325 nm. It is most likely that this weak emission band is STE emission in $BaCl_2$, since its position is consistent with the one reported by Selling et al. [10]. There is only very weak host lattice emission in the sample with 0.5% Pr. The emission spectrum of the 0.1% doped $BaCl_2$ sample (not shown) does show a strong host lattice emission band around 435 nm. When the Pr content is increased to 2%, the emission spectrum under X-ray irradiation is very similar to the one of the 0.5% doped material. The faint broad band emission is still present alongside the sharp line emissions of Pr^{3+}. There is a decrease in the intensity of the praseodymium emission as compared to the 0.5% doped sample (~ factor 1.6) due to cross-relaxation at the high Pr concentrations. The absence of *d-f* emission in $BaCl_2$ under excitation with X-rays is, just as for $SrCl_2$:Pr, due to the lack of spectral overlap between the emission of the host lattice and the absorption of the Pr *fd* states which are situated at too high energies.

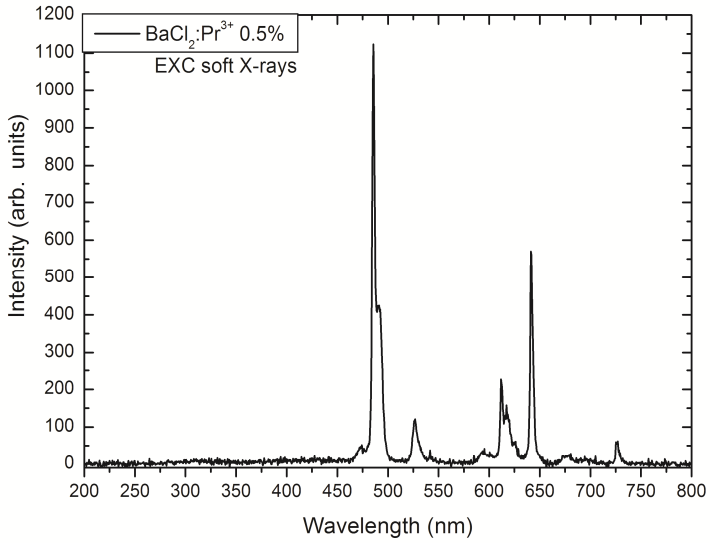

FIG. 4.11. Emission spectrum of $BaCl_2:Pr^{3+}$ 0.5% at 300 K under X-ray excitation (Cu-source, operated at 40kV) at 300 K.

Comparison of the luminescence from $SrCl_2$:Pr and $BaCl_2$:Pr shows that the energy transfer from the host lattice to the Pr^{3+} $4f^2$ states is more efficient in $BaCl_2$:Pr, leading to stronger Pr^{3+} emission in $BaCl_2$ under X-ray excitation. Secondly, the intensity ratio between the green $^3P_0 \rightarrow {}^3H_4$ (around 500 nm) and red $^3P_0 \rightarrow {}^3F_J$ (around 600-650 nm) *f-f* emission is reversed for the two materials.

4.4 CONCLUSIONS

$SrCl_2$ and $BaCl_2$ host lattices have been doped with Ce^{3+}, Pr^{3+} and Nd^{3+} to investigate the luminescence properties of the fast *d-f* emission and the potential for application as a fast scintillation material. Efficient and fast Ce^{3+} *d-f* emission is observed in both $SrCl_2$ and $BaCl_2$ under direct *f-d* excitation, host lattice (VUV) excitation and X-ray irradiation. The lifetime of the emission is 26 ns and 19 ns for Ce^{3+} in $SrCl_2$ and $BaCl_2$, respectively. After X-ray irradiation both Ce^{3+} activated compounds suffer from afterglow, which is most likely due to defect creation (e.g. color centers) by X-ray irradiation. The barium chloride results are in good agreement with the ones presented by Selling et al. [12], with the position of the cerium emission band being the same and where the afterglow has

also been observed. Only the doublet structure of the cerium emission is not present in the spectra presented in this work, which might be related to the dose of the ionizing radiation used.

For Pr^{3+} in $SrCl_2$ and $BaCl_2$ fast *d-f* emission between 250 and 325 nm is observed under direct excitation into the *fd* states. The emission and excitation spectra show an about 12 180 cm^{-1} and 12 610 cm^{-1} shift to higher energies of the lowest *fd* state in comparison with the lowest *5d* state for Ce^{3+} in the same host lattice for strontium chloride and barium chloride, respectively, in relatively good agreement with the expected shift based on the Dorenbos formula of 12 240 cm^{-1}. The lifetime of the Pr^{3+} *d-f* emission is about 13 ns in $SrCl_2$ and 10 ns in $BaCl_2$ which are among the fastest radiative decay times observed for *d-f* emission from lanthanide ions. Under host lattice excitation and X-ray irradiation no *d-f* emission is observed. Instead, slow host lattice related emission bands are observed along with *f-f* emission. The absence of *d-f* emission is explained by the high energy positions of the *fd* excited states for Pr^{3+}. The *fd* states are at higher energies than the host lattice emissions of both $SrCl_2$ and $BaCl_2$ (situated between 300 and 500 nm) and as a result there is no energy transfer from the host lattice to the *fd* states of Pr^{3+} in $SrCl_2$ and $BaCl_2$. The absence of energy transfer from the host lattice to the Pr^{3+} *fd* states makes $SrCl_2$ and $BaCl_2$ doped with Pr^{3+} unsuitable for application as fast scintillator materials, in spite of the superior fast decay time in comparison to known Ce^{3+} and Pr^{3+} scintillator materials.

Emission spectra for $SrCl_2$ and $BaCl_2$ doped with Nd^{3+} under VUV and X-ray excitation show only intraconfigurational $4f^3$ emission lines and host lattice related emission bands. No evidence for *d-f* emission from Nd^{3+} was found. The absence for *d-f* emission, even upon direct excitation in the *fd* band, is explained by the high energy position of the $4f^2 5d$ levels of neodymium very close to or in the conduction band of $SrCl_2$ and $BaCl_2$.

REFERENCES

[1] W.W. Moses, *Nucl. Instrum. Methods. A* **580** (2007) 919

[2] G. Muehllehner, J.S. Karp, *Phys. Med. Biol.* **51** (2006) R117

[3] P. Dorenbos, *J. Lumin.* **91** (2000) 155

[4] E. Zych, Luminescence and Scintillation of Inorganic Phosphor Materials in: H. Singh Nalwa and L. Shea Rohwer (Eds.), Handbook of Luminescence, Display Materials, and Devices vol. 2, American Scientific Publishers, 2003, pp. 251

[5] E.V.D. van Loef, P. Dorenbos, C.W.E. van Eijk, K.W. Krämer and H.U. Güdel, *Nucl. Instrum. Methods. A* **486** (2002) 254
[6] A. Bessiere, P. Dorenbos, C.W.E. van Eijk, K.W. Kramer, H.U. Güdel, C. de Mello Donegá, A. Meijerink, *Nucl. Instrum. Methods. A* **537** (2005) 22
[7] E.V.D. van Loef, P. Dorenbos, C.W.E. van Eijk, K.W. Kramer, H.U. Güdel, *Nucl. Instrum. Methods. A* **496** (2003) 138
[8] M.D. Birowosuto, P. Dorenbos, J.T.M. de Haas, C.W.E. van Eijk, K.W. Kramer, H.U. Güdel, *J. Lumin.* **118** (2006) 308
[9] W. Drozdowski, A.J. Wojtowicz, *Nucl. Instrum. Methods. A* **486** (2002) 412
[10] J. Selling, S. Schweizer, M.D. Birowosuto, P. Dorenbos, *IEEE Trans. Nucl. Sci.* **55** (2008) 1183
[11] J. Selling, Barium Halide Nanocrystals in Fluorozirconate based Glass Ceramics for Scintillation Application (PhD thesis, Universität Paderborn, 2007)
[12] J. Selling, S. Schweizer, M.D. Birowosuto, P. Dorenbos, *J. Appl. Phys.* **102** (2007) 074915
[13] J. Selling, Ce-doped $BaCl_2$ and fluorochlorozirconate glass-ceramic X-ray storage phosphors (M.Sc. thesis, Universität Paderborn, 2004)
[14] O.T. Antonyak, I.V. Kityk, N.S. Pydzyrailo, *Opt. Spectrosk.* **63** (1987) 529
[15] O.T. Antonyak, I.V. Kityk, N.S. Pydzyrailo, *Opt. Spectrosk.* **69** (1990) 606
[16] W.M. Li, M. Leskelä, *Mater. Lett.* **28** (1996) 491
[17] A. Zych, C. de Mello Donegá, A. Meijerink, *J. Lumin.* **129** (2009) 1535
[18] PDF (Powder Diffraction File) # 01-072-1537
[19] PDF (Powder Diffraction File) # 01-072-1388
[20] G. Zimmerer, *Nucl. Instrum. Methods. A* **308** (1991) 178
[21] Ch. Sugiura, *Phys. Rev. B* **9** (1974) 2679
[22] K. Onodera, M. Koshimizu, K. Asai, *Radiat. Phys. Chem.* **78** (2009) 1031
[23] J. Selling, M.D. Birowosuto, P. Dorenbos, S. Schweizer *J. Appl. Phys.* **101** (2007) 034901

5

Luminescence and energy transfer in $Lu_3Al_5O_{12}$ scintillators co-doped with Ce^{3+} and Tb^{3+}

ABSTRACT

$Lu_3Al_5O_{12}$ (LuAG) doped with Ce^{3+} is a promising scintillator material with a high density and a fast response time. The light output under X-ray or γ-ray excitation is, however, well below the theoretical limit. In this chapter the influence of co-doping with Tb^{3+} is investigated with the aim to increase the light output. High resolution spectra of singly doped LuAG (with Ce^{3+} or Tb^{3+}) are reported and provide insight into the energy level structure of the two ions in LuAG. For Ce^{3+} zero-phonon lines and vibronic structure are observed for the two lowest energy *5d* bands and the Stokes shift (2350 cm^{-1}) and Huang-Rhys coupling parameter (S=9) have been determined. Tb^{3+} *4f-5d* transitions to the high spin (HS) and low spin (LS) states are observed (including a zero-phonon line and vibrational structure for the high spin state). The HS - LS splitting of 5400 cm^{-1} is smaller than usually observed and is explained by a reduction of the *5d-4f* exchange coupling parameter J by covalency. Upon replacing the smaller Lu^{3+} ion with the larger Tb^{3+} ion, the crystal-field splitting for the lowest *5d* states increases causing the lowest *5d* state to shift below the $^5D_4$ state of Tb^{3+} and allowing for efficient energy transfer from Tb^{3+} to Ce^{3+} down to the lowest temperatures. Luminescence decay measurements confirm efficient energy transfer from Tb^{3+} to Ce^{3+} and provide a qualitative understanding of the energy transfer process. Co-doping with Tb^{3+} does not result in the desired increase in light output and an explanation based on electron trapping in defects is discussed.

5.1 INTRODUCTION

The field of medical imaging develops rapidly. New imaging techniques and improvement of existing techniques benefit from materials research aimed at higher sensitivity and resolution as well as increasing the safety and comfort of patients [1]. Computed Tomography (CT) is an important tool in the diagnosis of diseases. It relies on the creation of 3D-images of the body based on cross-sections created by a rapidly revolving scanning X-ray source and detector array around the patient. A crucial component in the detector array are scintillator crystals which convert high energy (X-ray) radiation into visible light which is detected by photodiodes or photomultipliers [2].

An important class of scintillators are aluminum garnets doped with lanthanide ions. The garnets have good chemical and radiation stability, excellent mechanical properties and show efficient luminescence when doped with lanthanide ions. Because of their cubic structure it is possible to prepare highly transparent scintillators by pressing of polycrystalline material. Scintillators made as transparent ceramics have important benefits over single crystals (lower cost, higher flexibility, reduced fracture risk) [3]. Of the various garnets, $Lu_3Al_5O_{12}$ (Lutetium Aluminum Garnet, LuAG) has a high density ($\rho_{LuAG} = 6.73$ g/cm^3) and high effective atomic number ($Z_{eff} = 60$) and therefore high stopping power. This makes LuAG more attractive as a scintillator host lattice than the lower density $Y_3Al_5O_{12}$ (Yttrium Aluminum Garnet, YAG) which was investigated extensively in the past thirty years for various applications [4].

LuAG doped with Ce^{3+} (LuAG:Ce) is regarded as a particularly promising scintillator due to its allowed electric-dipole *5d - 4f* transition and high theoretical light yield (LY). Based on the Bartram-Lempicki model the maximum LY has been calculated to be 60 000 photons/MeV [5]. However, experimental studies report lower values for the LY of LuAG:Ce and YAG:Ce which were 12 500 and 25 000 photons/MeV, respectively [6]. The discrepancy may be related to native defects in the host lattice (vacancies, anti-sites, dislocations) which trap electrons and holes which recombine non-radiatively [7]. In addition to a low efficiency, some afterglow is also observed which also points to a role of defects in the garnets [8].

To compete with trapping by defects, a higher activator concentration may be used. However, increasing the Ce^{3+} concentration will lead to concentration quenching: the excitation energy will be transferred between Ce^{3+} neighbors, which leads to energy migration to defects [9]. Concentration quenching is commonly observed at high activator concentrations. A possible solution to improve the energy flow from the host lattice to the emitting Ce^{3+} ions is the introduction of a co-activator which can capture the excitation energy (by capturing excitons) and transfers the excitation energy efficiently to Ce^{3+}. The

choice of a suitable co-activator can be guided by the analysis of the Dieke diagram for trivalent rare earth ions. FIGURE 5.1 presents the Dieke diagram where the *4f-5d* absorption and emission bands of Ce^{3+} in LuAG are marked.

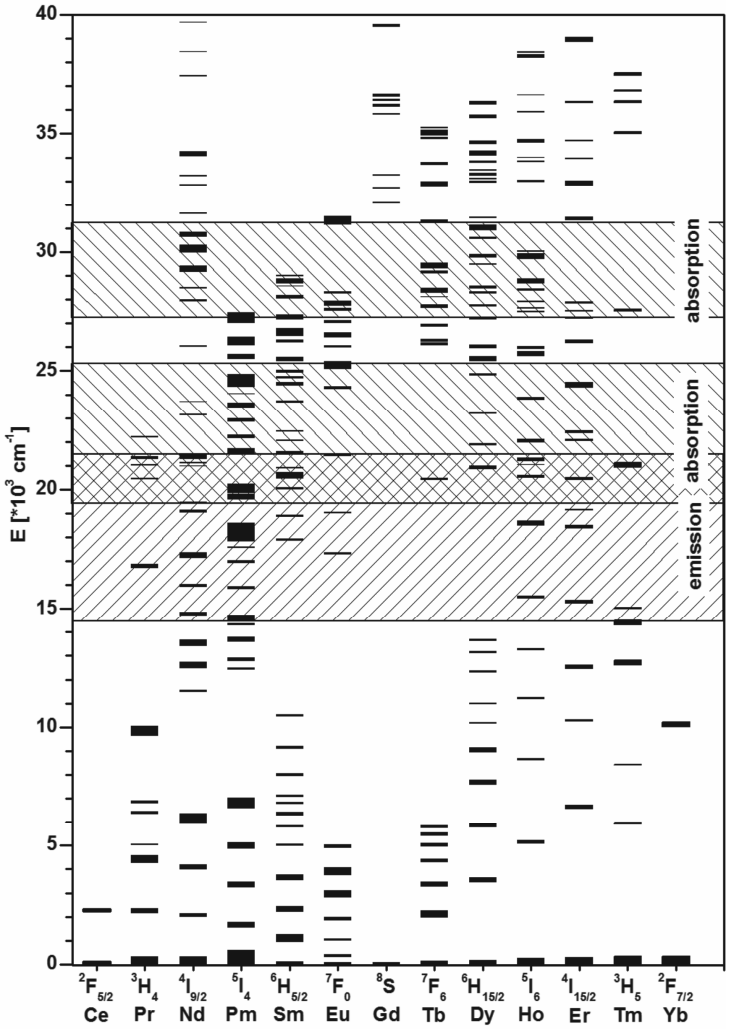

FIG. 5.1. Dieke diagram of trivalent rare earth ions with *4f-5d* Ce^{3+} absorption and emission bands indicated.

A suitable co-activator should be characterized by absorption levels located between absorption of host lattice and Ce^{3+} emission. In addition, its emission should overlap with Ce^{3+} absorption. At high co-activator concentrations an efficient capture of the host electronic excitations (electron-hole pairs or excitons) [10] created under high energy excitation will occur by the co-activator ions and will be followed by energy transfer to Ce^{3+}. Analysis of the diagram in FIG. 5.1 shows that Pr^{3+}, Tb^{3+} and Tm^{3+} are possible co-activators because the emitting levels $^3P_0$, $^5D_4$, and $^1G_4$ of Pr^{3+}, Tb^{3+}, and Tm^{3+}, respectively, overlap with Ce^{3+} absorption band around 450 nm.

In this chapter the potential of Tb^{3+} as a co-activator is explored and the energy transfer processes in LuAG:Ce,Tb are investigated. In order to gain insight into the energy transfer processes, also high resolution spectra were recorded at low temperatures and luminescence lifetime measurements of the Ce^{3+} and Tb^{3+} emission were performed. The results show that the $^5D_4$ level of Tb^{3+} is very close in energy to the lowest *5d* state of Ce^{3+}. Efficient donor-acceptor energy transfer takes place from Tb^{3+} to Ce^{3+}, but this does not result in an enhanced light output under high energy excitation.

5.2 EXPERIMENTAL

5.2.1. Synthesis

All materials investigated were prepared using a modified Pechini method as described by Katelnikovas et. al [11] using high purity reagents (at least 99.999%). Lu_2O_3, $Al(NO_3)_3 \cdot 9H_2O$, $Pr(NO_3)_3 \cdot 6H_2O$ and $Ce(NO_3)_3 \cdot 6H_2O$ were used as starting materials. Citric acid was used as the polymerizing agent. The calcinations were performed in two steps at 1000°C for 3 h and 1650°C for 4 h with intermediate grinding step. To obtain Ce and Tb ions in trivalent state the annealing was carried out under CO. Single crystalline phase formation in all samples was confirmed with the X-ray diffraction (XRD) measurements recorded on Rigaku Miniflex II diffractometer. Based on the XRD patterns, it was concluded that the samples are phase pure and for the mixed (Lu,Tb) compositions, solid solutions are formed based on the continuous shift of the XRD lines upon substitution of Lu by Tb.

5.2.2. Optical Spectroscopy

Luminescence spectra were recorded between 1.5 and 300 K on an Edinburgh Instruments FLS 920 spectrofluorometer using 450 W Xe lamp as excitation source. The spectra were measured with a resolution of 0.05 nm to 1 nm. Low-temperature measurements were done using an Oxford Instruments liquid helium flow cryostat. Luminescence decay traces were recorded using a ps diode laser at 406 nm in combination with time correlated photon counting using a TimeHarp card (for decays in the ns regime), excitation with 10 ns pulses at 355 nm from frequency-tripled YAG-laser in combination with a Tektronix 2 440 digital oscilloscope (in the μs regime) and flashlamp excitation at 280 nm using a multi-channel scaling card for decays in the ms time regime. Radioluminescence (RL) measurements were performed in reflection geometry using Ocean Optics HR2000 CG spectrometer (with a CCD detector) coupled to a 600 μm fiber optics and a 74-UV Collimating Lens to collect the light more efficiently. The resolution of the system was about 1.2 nm. Dedicated Ocean Optics SpectraSuite software was used to process the measurements. The counting time was 250 ms. White X-rays from a copper X-ray lamp of a DRON diffractometer were used as the excitation source. RL efficiencies of the materials studied were calculated against a commercial Gd_2O_2S:Eu (GOS) phosphor from Phosphor Technology (UKL63/F-R1, $D_{AV.}$ = 4.0 μm).

5.3 RESULTS AND DISCUSSION

In order to understand the energy flow in the co-doped LuAG:Ce,Tb samples, a good spectroscopic characterization of singly doped LuAG:Ce and LuAG:Tb is required. In sections *5.3.1* and *5.3.2* the optical properties of the singly doped samples are reported and discussed. In section *5.3.3* the luminescence properties, including luminescence lifetime measurements, for the co-doped sample LuAG:Ce,Tb are reported as well as light yield measurements under X-ray excitation.

5.3.1. LuAG:Ce^{3+}

From the Dieke diagram shown in FIG. 5.1 it is clear that the position of the lowest energy *5d* state for Ce^{3+} is very close in energy to the $^5D_4$ level of Tb^{3+}. The position of the *5d* state has been accurately determined for Ce^{3+} in YAG, where the zero-

phonon line (ZPL) for the lowest energy *5d* state is at 489.2 nm [9,12]. Since *5d* state is very sensitive to small variations in the local coordination, which affect the covalency and the crystal-field (CF) splitting, the position of the lowest energetic ZPL can be different when Ce^{3+} is doped into LuAG. To understand the energy transfer between Tb^{3+} and Ce^{3+} in LuAG it is important to determine the energy of the lowest *5d* level of Ce^{3+}. If the lowest *5d* level is higher in energy than the $^5D_4$ level, efficient trapping of the excitation energy by Ce^{3+} will be prevented.

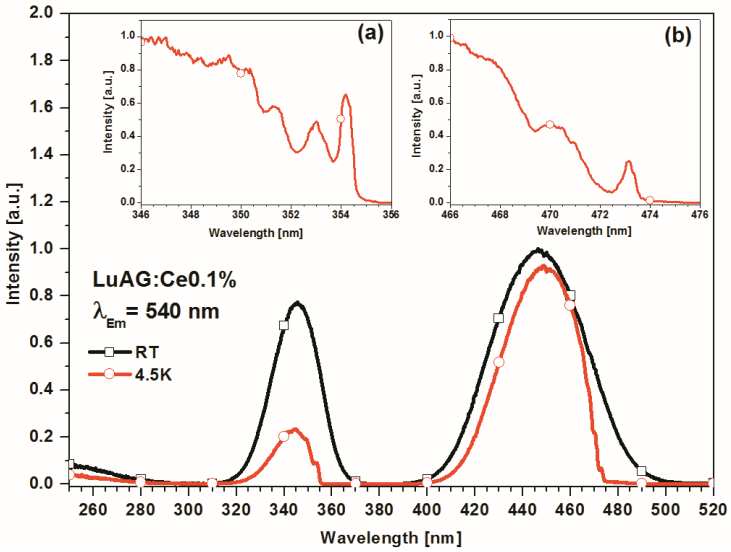

FIG. 5.2. Excitation spectra of the Ce^{3+} emission at 540 nm in LuAG:Ce^{3+} 0.1% at 4.5 K and RT. The insets (a) and (b) show higher resolution 4.5 K spectra around the onset of the two lowest energy *5d* excitation bands.

In FIG. 5.2 the excitation spectrum for the Ce^{3+} emission is shown, recorded at 293 K and at 4.5 K. The spectra exhibit two excitation bands with maxima in 445 nm and 340 nm which correspond to transitions to the two lowest energy levels of the five CF components in D_2 symmetry. The positions are similar to those for YAG:Ce. Both the width and relative intensities of these bands change with temperature. The 340 nm band is weaker at low temperatures, just as observed for YAG:Ce, due to the symmetry forbidden nature of the transition from the lowest CF component of the $^2F_{5/2}$ ground state to the second *5d* state (around 340 nm). The transition from the second CF component of the $^2F_{5/2}$ ground state to the *5d* state around 340 nm is symmetry allowed, which explains the

increase in relative intensity of the 340 nm excitation band at higher temperatures when the second CF component is thermally populated. This observation is consistent with results for YAG:Ce [9,12].

On the low energy side of both the 340 nm and the 450 nm excitation band, fine structure is observed at low temperature. The insets in FIG. 5.2 present high resolution spectra of the band edges recorded at 4.5 K in order to show the fine structure in more detail. The spectra reveal ZPL of Ce^{3+} *5d* bands as narrow peaks at 473.1 nm (21 138 cm^{-1}) and 354.2 nm (28 233 cm^{-1}) for the lowest and next higher Ce^{3+} *5d* levels, respectively. Thus the CF splitting for the two lowest *5d* CF levels of Ce^{3+} ion is 7100 cm^{-1}. This value is considerably smaller than the one observed for Ce^{3+} in YAG where ZPLs for the two lowest energetic *5d* bands are situated at 489.2 and 347.2 nm, giving a splitting of 8360 cm^{-1}. The difference in splitting reflects the strong influence of the local coordination on the *5d* CF splitting. It is, however, surprising that the larger CF splitting is observed for Ce^{3+} on the site with the larger ionic radius: the ionic radius of Y^{3+} in VIII coordination is 1.019 Å, while it is 0.977 Å for Lu^{3+} [13]. Usually, a larger CF splitting is observed for Ce^{3+} on a smaller site (smaller distances to the ligands give a larger CF splitting). For the garnet host a different trend is observed. Replacing the Y^{3+} ion (r_{VIII} = 1.019 Å) with the larger Gd^{3+} (r_{VIII} = 1.053 Å) has been shown before to result in larger CF splitting between the two lowest *5d* levels and a red-shift of the emission, both resulting from a higher CF splitting. In comparing YAG and LuAG, we observe the same trend: upon replacing Y^{3+} with the smaller Lu^{3+} ion, a blue shift of the emission is observed and the CF splitting decreases by 15%. Recent theoretical calculations on YAG:Ce,La have confirmed that replacing the smaller Y^{3+} ion by the larger La^{3+} ion (r_{VIII} = 1.160 Å) causes a blue-shift and a larger CF splitting, in spite of local average expansion. First principles calculations reproduce the experimental observations and show how other effects (covalency, ligand field anisotropies) can explain the blue shift and decreasing CF splitting of the Ce^{3+} emission in LnAG when the ionic radius of the Ln^{3+} ion decreases [14]. The present quantitative results on the position and shift of ZPLs of the two lowest energy *5d* bands for Ce^{3+} in LuAG may serve as an accurate input for comparison with future calculations.

The Ce^{3+} *5d-4f* emission spectrum of LuAG:Ce0.1% is shown in FIG. 5.3. The spectrum, recorded at 4.5 K, reveals two emission bands, split by ~ 2000 cm^{-1}. This splitting is typically observed and related to the splitting of the ^2F ground state in a $^2F_{5/2}$ and a $^2F_{7/2}$ state. The high resolution spectrum in the inset reveals the presence of a ZPL at 473.10 nm, the same position as observed in the low-temperature excitation spectrum. The relative intensity of the zero-phonon origin with respect to the higher energy emission band at 500 nm is small, approximately $1.2 \cdot 10^{-4}$.

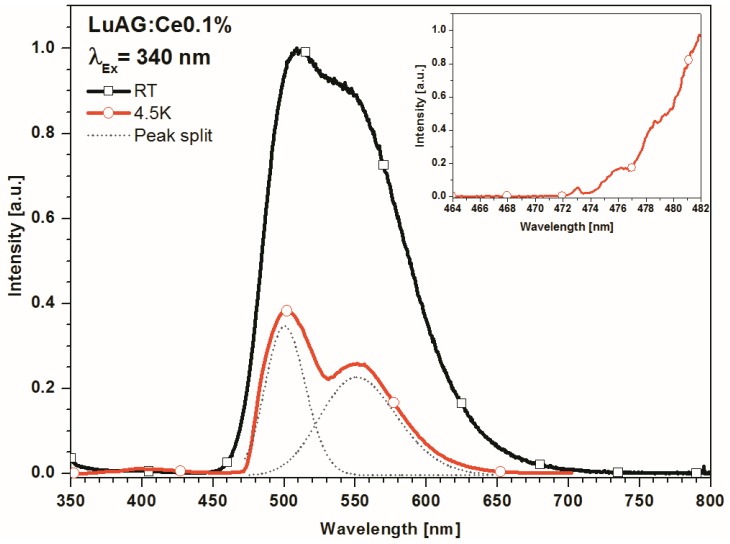

FIG. 5.3. Emission spectrum for LuAG:Ce^{3+} 0.1% recorded at 4.5 K (λ_{exc} = 340 nm). The inset shows the fine structure in the onset of the emission in more detail.

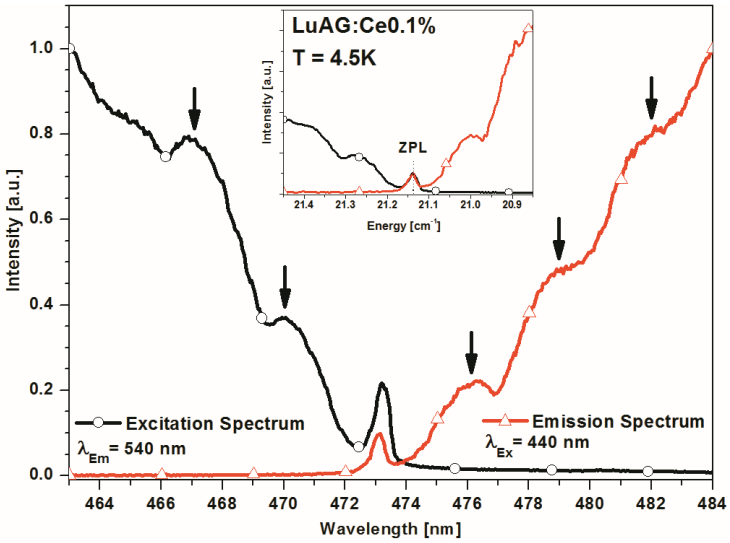

FIG. 5.4. High resolution excitation and emission spectra of LuAG:Ce^{3+} 0.1% showing ZPL overlap and vibronic replicas. Arrows mark the vibronic side bands.

In FIG. 5.4 the onset of both the excitation and emission spectrum are plotted in one figure. The typical mirror symmetry in the ZPL at 473.1 nm is observed. For YAG:Ce similar behavior of spectra has been reported [9]. The vibronic progression observed in low-temperature emission spectra for YAG:Ce revealed a strong coupling with 200 cm^{-1} vibrational modes. In case of LuAG:Ce, the phonon energies observed in the emission spectra are lower, ~ 130 cm^{-1} (see arrows in FIG. 5.4). The lower energies of the vibrational modes can be explained by the higher mass of the Lu^{3+} ion relative to Y^{3+}.

The information gained from the high resolution excitation and emission spectra at low temperature enables the calculation of the Stokes' shift and the Huang-Rhys coupling parameter. Note that accurate calculations are possible only for spectra recorded for low dopant concentrations. Re-absorption, inhomogeneous broadening and saturation effects prevent the observation of the ZPL and vibronic structure for higher concentrations and a red shift in the emission occurs as a result of energy transfer and re-absorption of the high energy part of the emission. This results in an overestimation of the value for the Stokes' shift, as is often found in the literature. Also, to determine the *5d*-$^2F_{5/2}$ emission maximum correctly, measurements should be performed at low temperature. At higher temperatures (e.g. 300 K) the spectra features related to emission from *5d* state to $^2F_{5/2}$ and $^2F_{7/2}$ multiplets overlap and one broad band is observed, as shown in FIG. 5.3, that prevents the determination of the Stokes' shift for the $5d \rightarrow {}^2F_{5/2}$ emission. The Stokes' shifts and the Huang-Rhys electron-coupling parameter *S* have been determined using different methods. A simple approach to calculate the Stokes' shift involves the determination of the energy difference between excitation (449.5 nm) and emission (501.5 nm) band maxima. This yields a value of 2312 cm^{-1} for the Stokes' shift of the *5d-4f* emission in LuAG:Ce. Another method relies on doubling of the energy distance between the ZPL and the maximum of the emission band. In this case a value of 2363 cm^{-1} is obtained. A third method involves the determination of the Huang-Rhys electron-phonon coupling parameter *S* from the relative intensity of the ZPL and using the equation for the Stokes' shift (SS): $SS = 2S \cdot \hbar\omega$. The intensity of the ZPL (I_{ZPL}) and the total emission (I_0) intensity are related by $I_{ZPL} = I_0 \cdot \exp(-S)$. The relative intensity of the ZPL is weak. After background subtraction the intensity of the ZPL has been determined to be $1.2 \cdot 10^{-4}$ from the total emission intensity of the $5d \rightarrow {}^2F_{5/2}$ emission band which gives $S = 9$. This, together with the dominant phonon frequency of 130 cm^{-1}, gives the value of Stokes' shift of 2340 cm^{-1}. The values obtained for *S* and the Stokes' shift are consistent.

5.3.2. *LuAG:Tb*$^{3+}$

The luminescence properties of the LuAG:Tb 1% are studied to determine the energies of the *4f-5d* absorption bands and the *4f-4f* emission bands.

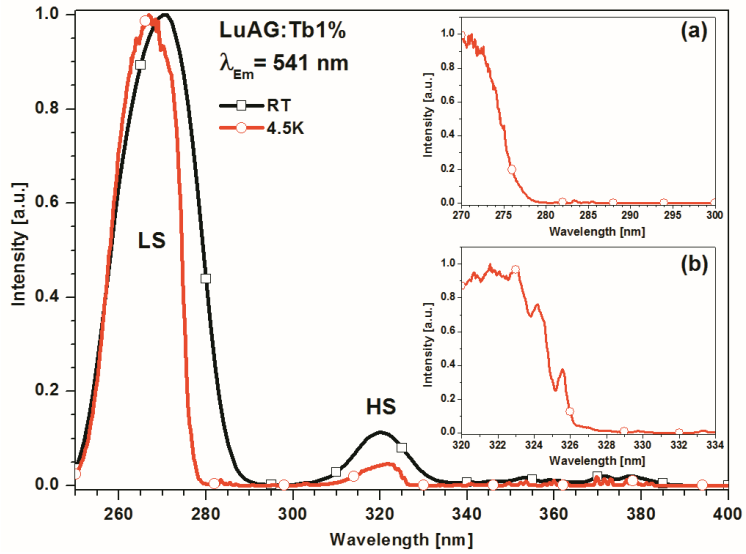

FIG. 5.5. Excitation spectra of 541 nm emission in LuAG:Tb^{3+} 1% at 4.5 K and 300 K. Insets (a) and (b) show high resolution spectra of the band onset, recorded at 4.5 K.

The excitation spectrum of Tb^{3+} doped LuAG for the $^5D_4$ emission at 541 nm is shown in FIG. 5.5. The spectrum shows a strong excitation band at 270 nm and a weaker band at 320 nm. The stronger band is assigned to the spin-allowed *4f-5d* transition from the ground state to the low spin *4f* ^{7}*5d* state (indicated by LS, low spin) and the weaker band is assigned to the transition to the spin-forbidden transition of the high spin (HS) *4f* ^{7}*5d* state. At 4.5 K fine structure (ZPL and vibronic side bands) is observed for the HS band (see inset (b) in FIG. 5.5) with the ZPL at 325.60 nm and vibrational energies of 130 cm^{-1}. Even though no ZPL is observed for the LS band, the HS-LS splitting can be calculated as 5388 cm^{-1} from the sharp onset of the LS band at 277 nm and the ZPL for the HS band at 325.6 nm. The value of HS-LS splitting obtained is smaller than what is typically observed for Tb^{3+} in other compounds. The average HS-LS splitting for Tb^{3+} reported by Dorenbos is 6300 cm^{-1} [15]. Meanwhile, in fluorides the HS-LS splitting close to 8000 cm^{-1} is typically observed. The large variation in HS-LS splitting has been related to the covalency

of the host lattice [16]. In a more covalent host lattice the larger spatial extension of the *5d* orbital will reduce the interaction with the *4f*-core electrons resulting in a smaller HS-LS splitting. In this connection it is interesting to compare the results to those for YAG:Tb where the HS - LS splitting is calculated to be 5285 cm^{-1} from the onset of the LS band at 280.7 nm and the ZPL for the HS band at 329.6 nm [17]. This indicates that the covalency for Ce^{3+} in the YAG lattice is larger than for Ce^{3+} in the LuAG lattice. The very low energy emission of Ce^{3+} in YAG can be explained by the lowering of the lowest energy emitting *5d* state of Ce^{3+} by a combined effect of a large CF splitting and a high covalency. The Tb^{3+} *4f-5d* absorption bands partly overlap with the intrinsic emission bands of LuAG typically observed as broad UV bands between 220 and 300 nm [18,19]. Efficient energy transfer from the host lattice to Tb^{3+} can be expected. Relaxation from the *5d* states to the $^5D_4$ state will be fast. Whether or not efficient energy transfer from the $^5D_4$ state of Tb^{3+} to the *5d* state of Ce^{3+} can occur, depends on the energy of the lowest $^5D_4$ state relative to the *5d* state of Ce^{3+}.

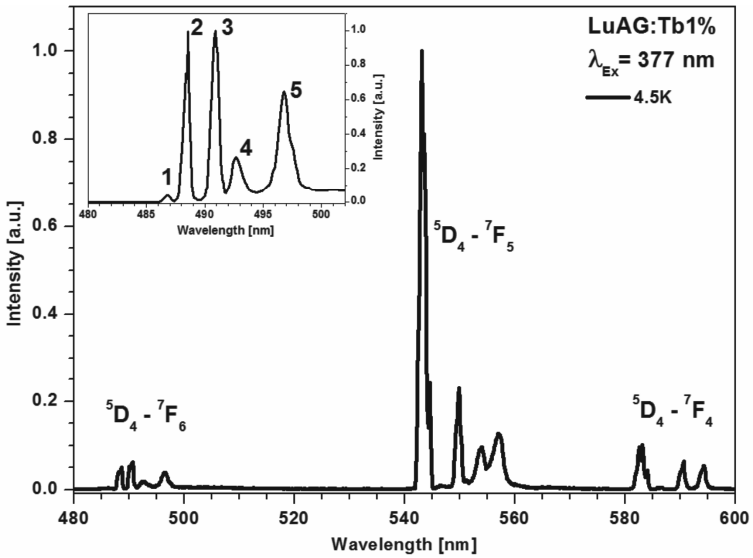

FIG. 5.6. Emission spectrum LuAG:Tb^{3+} 1% recorded at 4.5 K for excitation at 377 nm. The inset shows $^5D_4$ - $^7F_6$ emission in more detail.

To determine the position of the $^5D_4$ level, emission spectra of the *4f-4f* emission were measured for LuAG:Tb in the visible part of the spectrum. In FIG. 5.6 the emission spectrum of LuAG:Tb 0.1% is shown under excitation at 377 nm in the $^5D_3$ level of Tb. The emission spectrum shows *4f-4f* line emission corresponding to $^5D_4 \rightarrow {}^7F_{(6,5,4)}$

transitions. The structure of the $^5D_4$-$^7F_6$ emission presented in the high resolution inset comprises five emission lines that result from transitions from the lowest energy CF component of the $^5D_4$ level to different CF components of the $^7F_6$ ground level. The highest energy peak is at 486.85 nm, which is about 600 cm^{-1} lower in energy than the *5d* state of Ce^{3+}.

5.3.3. LuAG:Ce^{3+},Tb^{3+}

The information from the analysis of the luminescence spectra of the singly doped samples has been used to construct the energy diagram presented in the FIG. 5.7. The part above 40 000 cm^{-1} is evaluated from the analysis of FIG. 5.9 *(vide infra)*. Relaxation of high-energy photon excitation (X- or γ-ray) consists in multiple excitation and relaxation processes. In final stages, the energy dissipation in the doubly doped material will involve trapping of the elementary electronic excitations by both Ce^{3+} and Tb^{3+} ions. Based on the 600 cm^{-1} higher energy of the ZPL of the Ce^{3+} *5d* state relative to the $^5D_4$ state of Tb^{3+} energy transfer from Ce^{3+} to Tb^{3+} is expected rather than the desired $Tb^{3+} \rightarrow Ce^{3+}$ energy transfer. At low temperatures the Tb^{3+} emission is therefore expected to dominate. However, at higher temperatures the thermal equilibrium between the two states will allow for thermal population of the *5d* state of Ce^{3+} (at room temperature the Boltzmann distribution predicts a 5% population of a state 600 cm^{-1} higher in energy) and because of the ~ 10^4-10^5 times higher decay rate of the *5d* emission, the Ce^{3+} emission will dominate even though the *5d* state is higher in energy than the $^5D_4$ state of Tb^{3+}. It is however important to realize that replacing a substantial fraction of Lu^{3+} (r_{VIII} = 0.977) by the larger Tb^{3+} (r_{VIII} = 1.04) will cause a red-shift of the Ce^{3+} *5d* level, based on the trend discussed above (larger CF for Ce^{3+} on a larger cation site) and the *5d* state of Ce^{3+} may be shifted below the $^5D_4$ state of Tb^{3+} at high Tb^{3+} concentrations making the energy transfer from Tb^{3+} to Ce^{3+} efficient even at low temperatures.

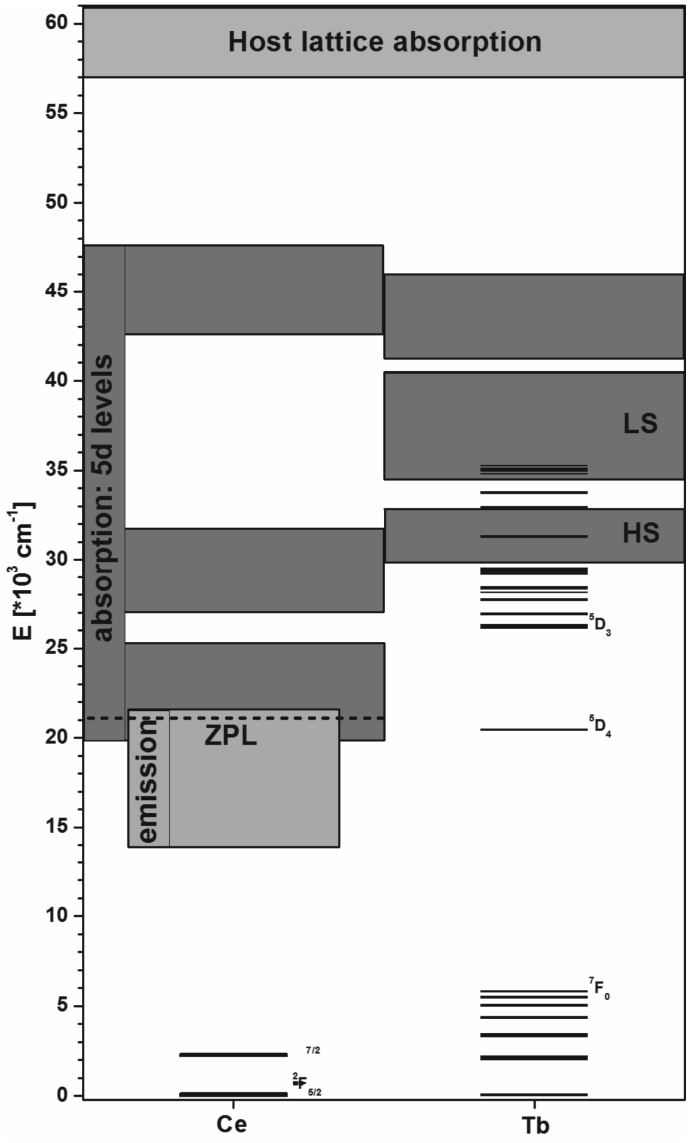

FIG. 5.7. Diagram of the energy levels for Ce^{3+} and Tb^{3+} in LuAG.

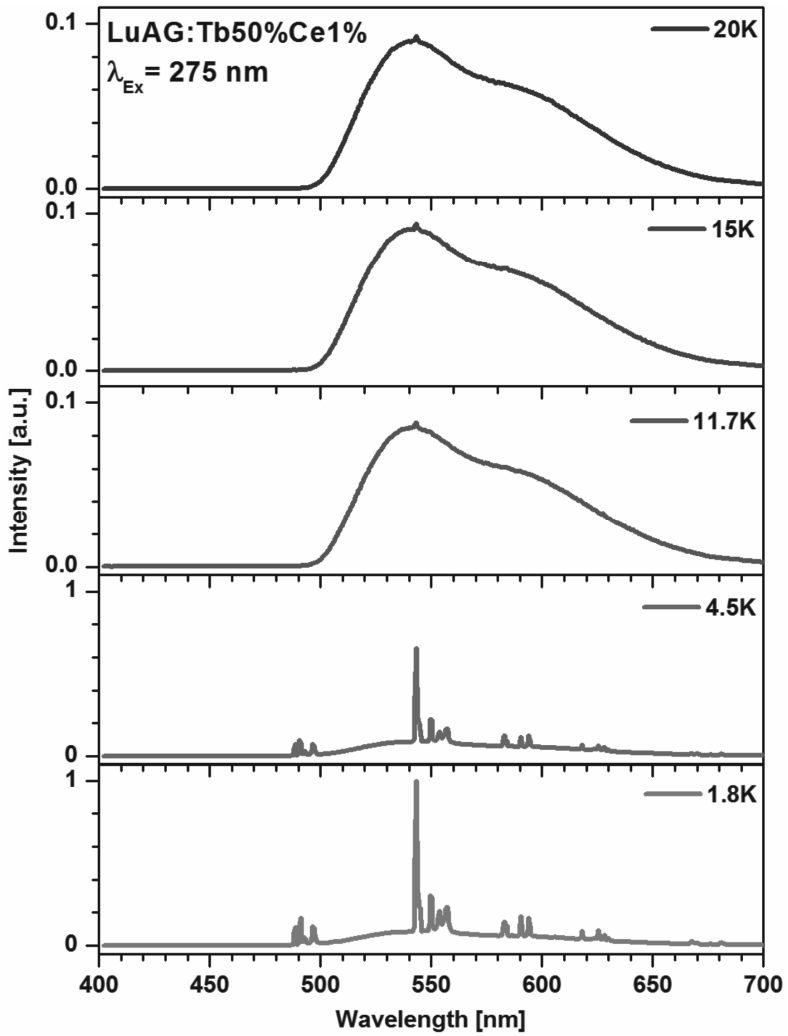

FIG. 5.8. Temperature dependent emission spectra of LuAG:Ce^{3+} 1%, Tb^{3+} 50% for excitation at 275 nm corresponding to the LS *5d* band of Tb^{3+}. All spectra were normalized to the spectrum measured at 1.8 K.

To investigate the energy transfer between Ce^{3+} and Tb^{3+}, excitation and emission spectra were measured for LuAG:Ce,Tb samples where 25, 50 or 75% of the Lu^{3+} was replaced by Tb^{3+}. As an example, in FIG. 5.8 emission spectra for LuAG:Ce 1%, Tb 50% at temperatures between 1.8 and 20 K are shown. At 1.8 K the Tb^{3+} emission is clearly

visible on top of the broad Ce^{3+} emission band. Upon raising the temperature, the Tb^{3+} emission decreases rapidly and above 5 K the Ce^{3+} emission dominates. Only a very weak Tb^{3+} emission line at 541 nm remains, superimposed on the Ce^{3+} *5d-4f* emission band. Even at low temperatures no ZPL is observed on the high energy side of the Ce^{3+} *5d-4f* emission band. This prevents a very accurate determination of the position of the lowest energy *5d* state for Ce^{3+}. The fact that no ZPL is observed is due to inhomogeneous broadening caused by disorder in the Lu-Tb^{3+} sub-lattice around the Ce^{3+} ions. The onset of the *5d-4f* emission band at low temperatures is around 495 nm which confirms the expected shift to lower energies due to the replacement of Lu^{3+} by the larger Tb^{3+} ion. In line with the 22 nm red-shift of the ZPL the emission band maximum has also shifted to some 25 nm longer wavelengths. Due to the shift, the Ce^{3+} *5d* level has energetically moved below the Tb^{3+} $^5D_4$ level, which remains around 487 nm since the position of *4f* levels is hardly influenced by the local surroundings. As a result of this, efficient trapping of the excitation energy by Ce^{3+} can be expected even at low temperature. This is in agreement with the observation of strong Ce^{3+} emission down to the lowest temperatures.

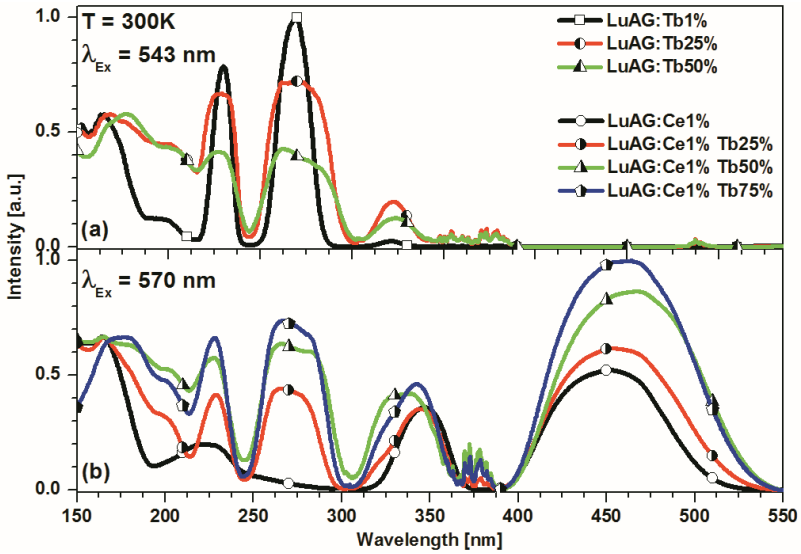

FIG. 5.9. Room temperature excitation spectra of: (a) the Tb^{3+} emission at 543 nm for LuAG with 1, 25, 50% of Tb^{3+}, and (b) the Ce^{3+} emission at 540 nm for (Lu,Tb)AG:Ce^{3+} 1% where 0, 25, 50 or 75% of the Lu^{3+} ions have been replaced by Tb^{3+}.

Finally, it is interesting to understand the strong decrease in the Tb^{3+} emission intensity between 1.8 and 10 K. At high Tb^{3+} concentrations, efficient energy migration over the Tb-sub-lattice can be expected. Energy migration in concentrated rare earth systems has been extensively investigated in the past, especially for Eu^{3+}, Tb^{3+} and Gd^{3+} [20-23]. For concentrations above the percolation point (where a 3D network of the optically active lanthanide ion is formed) energy transfer between lanthanide neighbors results in energy migration over the sub-lattice of the optically active ion to traps. In the present system, energy transfer between Tb^{3+} neighbors is efficient and the energy migrates over the $^5D_4$ levels of Tb^{3+} ions to traps, in this case Ce^{3+}. At the lowest temperatures (below 10 K) the energy migration is hampered due to small energy mismatches between neighboring Tb^{3+} ions resulting from inhomogeneous broadening. At higher temperatures phonon assistance (one- and two-phonon assisted energy transfer processes) helps to overcome the energy mismatch but at the lowest temperatures the phonons are frozen out and energy migration over the Tb^{3+} sub-lattice to Ce^{3+} becomes inefficient as the excitation energy is 'trapped' by Tb^{3+} ions having the $^5D_4$ level at slightly lower energies. This can explain the observation of Tb^{3+} emission below 10 K and the strong temperature dependence between 1.8 and 10 K [24,25].

The presence of efficient energy transfer from Tb^{3+} to Ce^{3+} is confirmed by the excitation spectra of the Ce^{3+} emission in (Lu,Tb)AG:Ce1% shown in FIG. 5.9. The excitation spectra of co-doped samples show, in addition to the *4f-5d* absorption bands of Ce^{3+}, the *4f-5d* excitation bands of Tb^{3+}, with strong spin-allowed absorption bands at 270 nm (also discussed above) and at 225 nm. The higher energy band at 225 nm is about 7500 cm^{-1} higher in energy than the 270 nm band, consistent with the CF splitting between the two lowest energy *5d* states observed for Ce^{3+}. Upon increasing the Tb-concentration from 25 to 50%, the 270 nm band shows a red-shift while the 225 nm band shows a blue shift, in line with the observation of an increase in CF splitting observed when the smaller host lattice ion Lu^{3+} is replaced by the larger Tb^{3+} ions. Another observation we should highlight here is dependence of host lattice intrinsic absorption edge on Tb^{3+} content. The pure Lu sample shows an onset of fundamental absorption around 185 nm that is in agreement with [18,19]. Co-doping with Tb^{3+} leads to gradual red shift of the onset and overlap with 225 nm Tb^{3+} *4f-5d* absorption band when Tb^{3+} content reaches 75%.

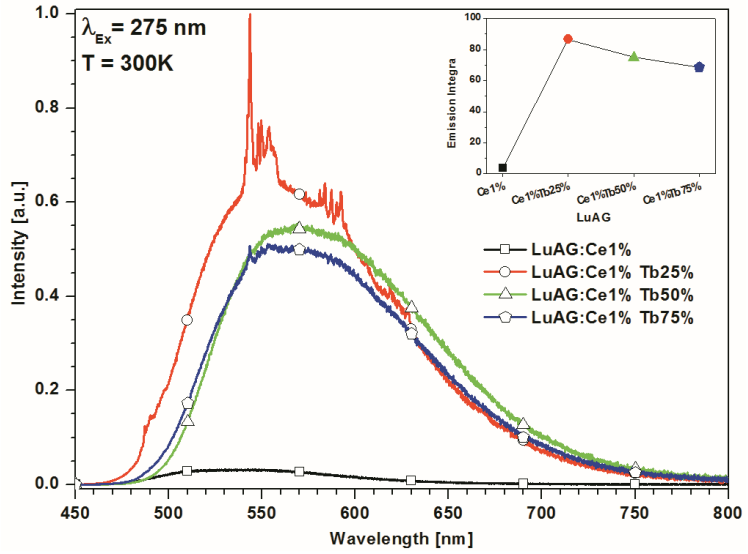

FIG. 5.10. Room temperature emission spectra of Ce^{3+} and Tb^{3+} doped LuAG at excitation wavelength of 275 nm corresponding to LS *5d* band of Tb^{3+}. The inset shows the integrated intensity in the 450-800 nm range.

In FIG. 5.10 emission spectra at room temperature are shown for (Lu,Tb)AG:Ce 1% with 0, 25, 50 or 75% Tb^{3+} for excitation at 275 nm in the LS *5d* band of Tb^{3+}. Analysis of these spectra together with decay time measurements shown in FIG. 5.11, help to understand the energy transfer occurring in between Tb^{3+} and Ce^{3+} ions doped into LuAG host. Upon excitation at 275 nm in the sample doped with Ce^{3+} only, the emission intensity is weak, as Ce^{3+} is not efficiently excited at 270 nm (no *4f-5d* absorption band). In all spectra the broad band emission of Ce^{3+} dominates showing that there is efficient energy transfer from Tb^{3+} to Ce^{3+}. In case of LuAG:Ce 1%,Tb 25%, Tb^{3+} *4f-4f* line emissions on top of a broad Ce^{3+} emission band are visible. The relative intensity of the Tb^{3+} emission is approximately 3%. The Tb^{3+} emission peaks almost disappear when 50 or 75% Tb^{3+} is introduced. The small peak around 550 nm for the 75% Tb^{3+} sample is only ~ 0.4% of the total emission intensity. The incomplete $Tb^{3+} \rightarrow Ce^{3+}$ energy transfer in the 25% samples indicates that energy migration over the diluted Tb-sub-lattice is not efficient at 25% Tb^{3+} and a significant fraction of excited Tb^{3+} ions experiences an intra-center radiative relaxation. At 50% and above, efficient energy migration over the Tb-sub-lattice to Ce^{3+} ions occurs. Note that, after a continuous red-shift for increasing Tb^{3+} concentration, the emission spectrum for the system with 75% Tb^{3+} shows a small blue shift in comparison with the system with 50% Tb^{3+}. The relative intensity of the Tb^{3+} emission can be

estimated theoretically, assuming fast energy migration and an energy difference between the Ce^{3+} *5d* level and the Tb^{3+} $^5D_4$ level that is much smaller than kT, i.e. the population of the Ce^{3+} and Tb^{3+} excited states is proportional to the concentrations of these ions. The relative emission intensities are then proportional to the concentration of ions and the radiative decay rates:

$$\frac{I_{Tb}}{I_{Ce}} = \frac{P_r^{Tb} \cdot C^{Tb}}{P_r^{Ce} \cdot C^{Ce}} \tag{5.1}$$

where I_{Tb} is the Tb^{3+} emission intensity, I_{Ce} is the Ce^{3+} emission intensity, P_r are the radiative decay rates (~ 310 s^{-1} for the $^5D_4$ emission of Tb^{3+} and $16 \cdot 10^6$ s^{-1} for the *5d-4f* emission of Ce^{3+} in LuAG) and C denotes the concentration. For the 75% Tb^{3+} samples, a relative intensity for the Tb^{3+} emission is calculated to be 0.15% that is close to the experimentally obtained value of 0.4%.

To further analyze the energy transfer processes, luminescence decay curves can be recorded. Decay curves were measured at different time scales (ns, µs and ms) for the Ce^{3+} emission in samples co-doped with different Tb^{3+} concentrations. In FIG. 5.11(a) the decay curves are shown on a ns time scale. For the samples without Tb^{3+} or with low Tb^{3+} concentration (1% or less) a single exponential decay is observed with $\tau = 63$ ns. Upon increasing the Tb^{3+} concentration, an initial faster decay for the Ce^{3+} emission is observed due to energy transfer to Tb^{3+}. The fast component is more pronounced for the higher Tb-concentrations. For the intermediate (µs) time scale (FIG. 5.11(b)) the situation is complex. The initial decay is faster for the samples co-doped with 25 and 75% Tb^{3+} and slower for the 50% Tb^{3+} sample. In the 10-40 µs regime, the situation is reversed. In the long (ms) time regime (FIG. 5.11(c)), the sample with 25% Tb^{3+} shows a fast initial decay followed by a slow tail, confirming that the energy migration is hampered by the low Tb-concentration. One of the reasons for existence of the slow decay components reflecting delayed feeding of the Ce^{3+} ions is connected with migration of excitation energy over the Tb^{3+} sub-lattice. The faster diffusion (above the percolation point) in the samples with 50 and 75% Tb^{3+} results in a rapid decay and no ms decay component is observed. Another reason for appearance of ms decay tail can be connected with thermally induced de-trapping of electrons from shallow traps into the conduction band followed by the delayed recombination at Ce^{3+} ions [26,27]. The longer decay in the 100-200 µs regime for the Ce^{3+} emission decay in the 75% Tb^{3+} sample compared with the 50% Tb^{3+} sample is consistent with the observations in FIG. 5.11(b), but seems to be unusual. Normally, for higher donor concentration the faster energy migration leads to shorter decay times. However, the phenomenon observed may be connected with variation of trap depth due to lowering the conduction band. Particularly, some traps may become shallower and other become delocalized within the conduction band. The higher Tb^{3+} concentration can also explain a

slightly longer decay, since in the case of thermal equilibrium the population of the $^5D_4$ state of Tb^{3+} is higher, but it cannot explain the lengthening observed in FIGS. 5.11(b) and 5.11(c). In spite of extensive studies of the decay curves, also as a function of temperature, it has not been possible to explain all the observed luminescence decay behavior. This illustrates the complexity of the system, where due to the proximity of the Ce^{3+} and Tb^{3+} levels, both ions can act as donor and acceptor, with a very different decay rate, while also energy migration over the Tb^{3+} sub-lattice occurs. In addition, the energy mismatch varies as a function of Tb-concentration due to the strong red-shift of the *5d* state of Ce^{3+} upon raising the Tb-concentration. Because of this complexity, any further analysis of the decay curves is cumbersome. The observations presented above are in good qualitative agreement with the results recently presented by Setlur et al. [28] who provided a more quantitative analysis of the luminescence decay curves and found evidence of a shift from energy transfer through dipole-dipole transfer to exchange mediated energy transfer at higher Tb^{3+} concentrations.

The results presented above demonstrate that energy transfer from Tb^{3+} to Ce^{3+} is very efficient in LuAG:Ce,Tb. Energy losses in LuAG:Ce scintillators due to competition in trapping of host lattice excitations between Ce^{3+} and defects may be prevented by co-doping with Tb^{3+}. At high Tb^{3+} concentrations, trapping of host lattice excitations will occur mainly at Tb^{3+} ions and will be followed by energy transfer to Ce^{3+} ions.

To verify if this concept can be used to increase the actual efficiency of the scintillator materials above the typical 12 500 photons/MeV, luminescence efficiency measurements under soft X-ray excitation were done for (Lu,Tb)AG:Ce1% with 0, 25, 50 or 75% Tb. The results are shown in FIG. 5.12. Emission spectra were recorded under identical conditions for excitation with a soft X-ray source. The spectra were recorded over a wide spectral range 200-1100 nm. Only in the region between 450 and 750 nm emission is observed. The integrated intensity under the emission curves is proportional to the quantum yield for the different materials. In the inset the integrated intensity is plotted for the different systems. The intensity is approximately constant for the systems with 0-50% terbium. A lower light yield is observed for the sample co-doped with 75% Tb^{3+}. The fact that there is no increase in the light yield indicates that the efficiency losses cannot be reduced by co-doping with Tb. There are different models that could explain these observations. Possibly, the energy losses are related to electron traps which trap a considerable fraction of electrons in the conduction band, which recombine non-radiatively with holes. Both Ce^{3+} and Tb^{3+} can only act as hole trap and as a result, energy losses by defects trapping electrons will not be reduced and give rise to the same fractional loss. The co-doping only results in a shift of the initial excitation from Ce^{3+} to Tb^{3+} but since excitation of Tb^{3+} is followed by an almost 100% energy transfer to Ce^{3+}, the light output from Ce^{3+} is not affected. In the past a variety of shallow electron traps related to anti-site

defects have been identified in LuAG:Ce and this may explain the low light output upon X-ray excitation [27].

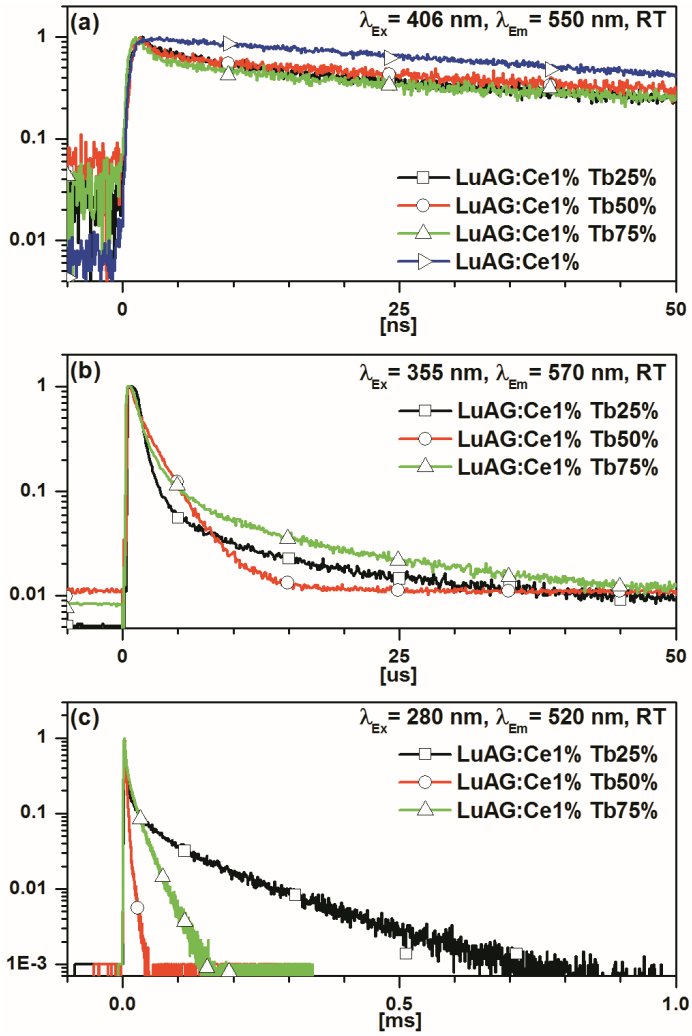

FIG. 5.11. Room temperature luminescence decays of Ce^{3+} emission in LuAG:Ce^{3+},Tb^{3+}: (a) ns time regime, λ_{exc} = 406 nm, λ_{em} = 550 nm; (b) µs time regime, λ_{exc} = 355 nm, λ_{em} = 570 nm and (c) ms time regime, λ_{exc} = 280 nm, λ_{em} = 520 nm.

It would be interesting to co-dope LuAG:Ce with a co-dopant that is capable of trapping electrons and transferring its excitation energy to Ce^{3+}. Eu^{3+} and Tm^{3+} are interesting candidates, although energy back-transfer from Ce^{3+} to Eu^{3+} or Tm^{3+} may prevent the observation of an increased Ce^{3+} light output. Alternatively, the low light yield may be more general and inherent to the relatively high defects concentration in LuAG (and other garnets). Part of the excitation energy is lost at defect sites before the activators are reached. If this is the case, only improved synthesis techniques aimed at reducing the defect concentration will raise the light yield. Efforts in this direction are ongoing. An important aspect is reducing the temperature at which the single crystals are grown. The very high growth temperatures (e.g. ~ 2000°C in a typical Czochralski growth) are responsible for the high defect concentration in garnet, e.g. anti-site defects [29]. An option is to make transparent ceramics from (nano)crystalline powders at lower temperatures (1500-1700°C), as has been successfully demonstrated for YAG [30,31]. This route may lead to more efficient LuAG:Ce scintillators.

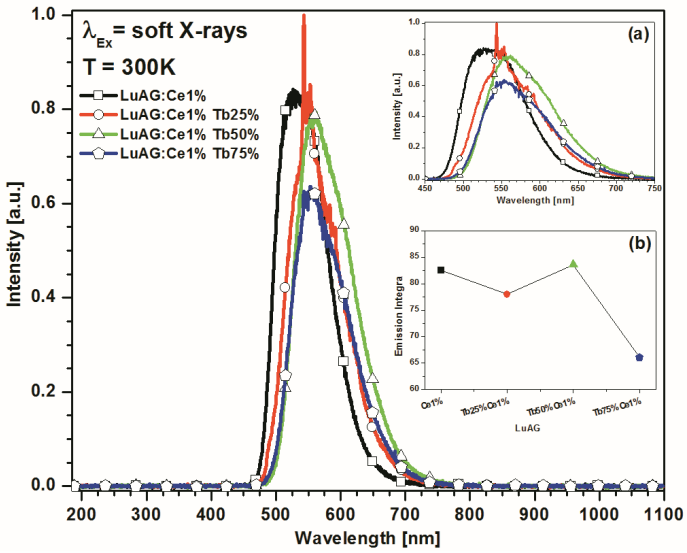

FIG. 5.12. Emission spectra of LuAG:Ce^{3+},Tb^{3+} monitored under soft X-ray excitation. The measurements were done at 300 K under identical experimental conditions.

5.4 CONCLUSIONS

The luminescence properties of LuAG doped with Ce^{3+} and Tb^{3+} have been investigated and new insights into the energy level structure, energy transfer and scintillation efficiency have been obtained. For Ce^{3+} in LuAG ZPLs are observed at 473.1 nm (21 138 cm^{-1}) and 354.2 nm (28 233 cm^{-1}) for the lowest and next higher Ce^{3+} *5d* levels, respectively. Vibronic structure is observed in both the excitation and emission spectra. The Huang-Rhys parameter ($S = 9$), phonon energy (130 cm^{-1}) and Stokes' shift (2300 cm^{-1}) have been determined from the low-temperature spectra. The luminescence spectra of Tb^{3+} show the characteristic $^5D_4$ emission lines in the green spectral region. The Tb^{3+} excitation spectra are dominated by $4f^8 \rightarrow 4f^7 5d$ transition. The spin-forbidden transition to the high spin (HS) state has a ZPL at 325.6 nm and shows vibronic structure, the spin-allowed transition to the low spin (LS) state has a sharp onset at 277 nm, giving a HS-LS splitting of 5 400 cm^{-1}, which is lower than usually observed. The smaller splitting is explained by a smaller *5d-4f* exchange coupling parameter *J* which is reduced by covalency effects.

The co-doped system LuAG:Ce,Tb demonstrates efficient energy transfer from Tb^{3+} to Ce^{3+}. Replacement of the smaller Lu^{3+} ion by the larger Tb^{3+} ion induces a larger crystal splitting that shifts the lowest *5d* state of Ce^{3+} to lower energies, even below the $^5D_4$ state of Tb^{3+}. The red-shift of the Ce-emission and larger CF splitting upon substitution of a smaller rare earth ion by a larger one has been observed previously in garnet host lattices and is contrary to the usual observation (larger CF splitting on a smaller cation site). In the co-doped systems with 25, 50 and 75% of Tb^{3+} efficient energy transfer to Ce^{3+} occurs down to the lowest temperatures. Luminescence lifetime measurements show that for 25% Tb^{3+} there is still slow (ms) feeding of the Ce^{3+} emission, which is not observed for 50 and 75% of Tb^{3+} where fast diffusion over the Tb^{3+} sub-lattice is followed by efficient energy transfer and emission from Ce^{3+}. A quantitative analysis of the decay curves to extract energy transfer parameters is hampered by the complicated situation of the nearly resonant $^5D_4$ state of Tb^{3+} and the *5d* state of Ce^{3+} and rapid energy transfer between Ce^{3+} - Tb^{3+}, Tb^{3+} - Ce^{3+} and Tb^{3+} - Tb^{3+}.

The light output under soft X-ray excitation has been shown to not increase upon co-doping with Tb^{3+} remaining well below the theoretical maximum based on the Bartram-Lempicki model. An increase in light output due to efficient trapping of host electronic excitations by Tb^{3+} followed by energy transfer to Ce^{3+} does not occur. Possibly, fast trapping of electrons in defect sites, followed by non-radiative recombination with holes, is responsible for the lower efficiency and these losses are not reduced by co-doping with Tb^{3+} since both Ce^{3+} and Tb^{3+} act as hole traps. To increase the scintillation efficiency

either co-doping with luminescent sensitizers for Ce^{3+} that act as electron traps or improved crystal growth techniques, reducing the defect concentration, is required.

REFERENCES

[1] M. Conti, L. Eriksson, H. Rothfuss, C.L. Melcher, *IEEE Trans. Nucl. Sci.* **56** (2009) 3
[2] C.R. Ronda, J.M. Gondek, E. Goirand, T. Jüstel, M. Bettinelli, A. Meijerink, in *Proceedings of Material Research Society Symposium* **1111** (2009) 1111-D08-01
[3] N.J. Cherepy, J.D. Kuntz, T.M. Tillotson, D.T. Speaks, S.A. Payne, B.H.T. Chai, Y. Porter-Chapman, S.E. Derenzo, *Nucl. Instrum. Methods* **579** (2007) 1
[4] R. Autrata, P. Schauer, J. Kvapil, J. Kvapil, *J. Phys. E* **11** (1978) 7
[5] A.M. Srivastava, C.R. Ronda, "*Luminescence: From Theory to Applications"*, edited by C.R. Ronda (Wiley-VCH Weinheim, 2007), Chapter 5
[6] J.A. Mares, A. Beitlerova, M. Nikl, N. Solovieva, C. D'ambrosio, K. Blazek, P. Maly, K. Nejezchleb, F. De Notaristefani, *Radiat. Meas.* **38** (2004) 4-6
[7] M.J. Weber, *Nucl. Instrum. Methods Phys. Res., Sect. A* **527** (2004) 1-2
[8] J.J. Shiang, A.A. Setlur, A.M. Srivastava, H.A. Comanzo, **US6630077 B2** (2003)
[9] V. Bachmann, C. Ronda, A. Meijerink, *Chem. Mater.* **21** (2009) 2077-2084
[10] M.V. Korzhik, W.P. Trower, *Appl. Phys. Lett.* **66** (1995) 18
[11] A. Katelnikovas, J. Barkauskas, F. Ivanauskas, A. Beganskiene, A. Kareiva, *J. Sol-Gel Sci. Technol.* **41** (2007) 3
[12] D.J. Robbins, *J. Electrochem. Soc.* **126** (1979) 9
[13] R.D. Shannon, C.T. Prewitt, *Acta Crystallogr., Sect. B: Struct. Sci* **25** (1969) 5
[14] A.B. Munoz-Garcia, J.L. Pascual, Z. Barandiaran, L. Seijo, *Phys. Rev. B* **82** (2010) 6
[15] P. Dorenbos, *J. Lumin.* **91** (2000) 3-4
[16] P. Dorenbos, *J. Phys.: Condens. Matter* **15** (2003) 36
[17] A. Zych, J.M. Ogiegło, C.R. Ronda, C. de Mello Donegá, A. Meijerink "Analysis of the shift of zero-phonon lines for *f-d* luminescence of lanthanides in the relation to the Dorenbos model", to be published
[18] V. Babin, K. Blazek, A. Krasnikov, K. Nejezchleb, M. Nikl, T. Savikhina, S. Zazubovich, *Phys. Status Solidi* **2** (2005) 1
[19] Yu. Zorenko, A. Voloshinovskii, V. Savchyn, T. Voznyak, M. Nikl, K. Nejezchleb, V. Mikhailin, V. Kolobanov, D. Spassky, *Phys. Status Solidi B* **244** (2007) 6
[20] A. Meijerink, G. Blasse, *J. Lumin.* **43** (1989) 5
[21] M. Batentschuk, A. Osvet, G. Schierning, A. Klier, J. Schneider, A. Winnacker, *Radiat. Meas.* **38** (2004) 4-6
[22] H.S. Kiliaan, A. Meijerink, G. Blasse, *J. Lumin.* **35** (1986) 3

[23] W.M.A. Smit, G. Blasse, *J. Solid State Chem.* **63** (1986) 2
[24] G. Blasse, *Prog. Solid State Chem.* **18** (1988) 2
[25] T. Holstein, R.K. Lyo, R. Orbach, "*Laser Spectroscopy of Solids*", edited by W.M. Yen and P.M. Selzer (Springer Verlag, Berlin, 1981), Chapter 2
[26] M. Nikl, J. Pejchal, E. Mihokova, J.A. Mares, H. Ogino, A. Yoshikawa, T. Fukuda, A. Vedda, C. D'Ambrosio, *Appl. Phys. Lett.* **88** (2006) 14
[27] M. Nikl, A. Vedda, M. Fasoli, I. Fontana, V.V. Laguta, E. Mihokova, J. Pejchal, J. Rosa, K. Nejezchleb, *Phys. Rev. B* **76** (2007) 19
[28] A.A. Setlur, J.J. Shiang, C.J. Vess, *J. Phys. Chem. C* **115** (2011) 8
[29] M. Zhuravleva, K. Yang, M. Spurrier-Koschan, P. Szupryczynski, A. Yoshikawa, C.L. Melcher, *J. Cryst. Growth* **312** (2010) 8
[30] T. Tachiwaki, M. Yoshinaka, K. Hirota, T. Ikegami, O. Yamaguchi, *Solid State Commun.* **119** (2001) 10-11
[31] L. Wen, X. Sun, Z. Xiu, S. Chen, C.-T. Tsai, *J. Eur. Ceram. Soc.* **24** (2004) 9

6

Analysis of the radiative lifetime of Pr^{3+} *d-f* emission

ABSTRACT

The radiative lifetime of excited states is governed by Fermi's golden. For many applications the radiative decay rate is an important parameter. For example, for scintillators materials in PET scanners a short response time is crucial and it has been realized that the *d-f* emission of Pr^{3+} is faster than for the widely applied *d-f* emission from Ce^{3+}. In this chapter the radiative decay rate of *d-f* emission from Pr^{3+} is systematically investigated in a wide variety of host lattices, including scintillators materials. The variation in the decay rate is analyzed based on Fermi's Golden Rule. The trend observed is best described using a full cavity model to correct for local-field effects and a λ^3 factor to account for the energy of the transition. Still, there is a considerable scatter of the experimental data around the best fit to these data. The variation is explained by uncertainties in the refractive indices and a variation in the transition dipole moment of the *d-f* transition for Pr^{3+}. Based on the results, the shortest radiative lifetime that can be achieved for Pr^{3+} *d-f* emission is predicted to be ~ 6 ns.

6.1 INTRODUCTION

Inorganic scintillator materials with a short response time are widely investigated for application in the field of medical imaging, especially for use in the Positron Emission Tomography (PET) [1-6]. The coincident detection of two γ-rays emitted during a positron annihilation event depends strongly on the sharpness of the emission spikes generated by the absorption of γ-photons by the scintillator. A faster response time improves the image resolution. Emission in scintillators materials originates from activator ions, which show luminescence after energy transfer from the host lattice to the activator. Fast emission is achieved for a fully allowed electronic transition. The present generation of PET-scanners mostly applies Ce^{3+} - doped scintillators materials. The fully allowed (parity and spin allowed) transition on the Ce^{3+} ions between the excited *5d* state and the *4f* ground state results in lifetimes between 20 and 70 ns. The energy of the emitting 5d state is influenced by the covalency of the material as well as the crystal-field splitting. Ce^{3+} emission can occur in a broad spectral range (350-600 nm). As a consequence, the emission lifetime varies widely from ~ 20 ns for UV emission to ~ 70 ns for orange emission, as predicted by Fermi's Golden rule [1,2]. Since for PET a shorter-lived emission will improve the timing resolution of the system, Pr^{3+} *d-f* emission in inorganic host lattices is a promising alternative for Ce^{3+} *d-f* emission. The *d-f* emission of Pr^{3+} is about 2-3 times faster than *d-f* emission of Ce^{3+} because this emission is at ~ 12 240 cm^{-1} higher energy for Pr^{3+} than for Ce^{3+} in the same host [7]. As a result, research on scintillator materials with efficient Pr^{3+} *d-f* emission has attracted much attention in recent years. There is however no quantitative analysis of the trend in the emission lifetimes. It is the aim of this chapter to provide such an analysis and compare the results with earlier work on the *d-f* emission lifetimes of Eu^{2+} and Ce^{3+} [1,2]. Careful experiments were conducted to accurately determine the radiative lifetime and wavelength of the *d-f* emission from Pr^{3+} in phosphates, borates, silicates, aluminates, fluorides and oxychlorides. A clear general trend is observed: the radiative lifetime increases from 7.6 ns to 23 ns as the Pr^{3+} *d-f* emission shifts from 230 nm to 320 nm. A careful quantitative analysis and comparison with Fermi's golden rule is hampered by a large scatter in the data due to uncertainties in the refractive indices, different models for local-field correction and a variation in the transition dipole moment. It will be discussed that these uncertainties are similar as in previous studies on the decay times of the *d-f* emission from Eu^{2+} and Ce^{3+}.

6.2 EXPERIMENTAL

6.2.1. Measurements

The luminescence spectra and luminescence decay curves have been measured using synchrotron radiation at SUPERLUMI station (DESY, Hamburg). A detailed description of the set-up can be found in section 1.6 of this thesis, as well as in REF. 8. The synchrotron spectra were measured in three time windows (integrated, fast and slow) making it possible to distinguish between fast and slow emissions. The fast time window extended from 2 to 14 ns, while the slow time window was set between about 100 and 200 ns after the ps synchrotron excitation pulse. Excitation spectra were corrected for variation of the intensity as a function of wavelength using the excitation spectrum of sodium salicylate as a reference. The emission spectra were not corrected for detector response. Luminescence decay curves were recorded using time correlated photon counting with a time resolution of ~ 200 ps, mainly limited by the response time of the MCP detector (Hamamatsu R6358p). Time to Amplitude Conversion (TAC) and Pulse Height Analysis (PHA) were used to measure luminescence decay curves. The sample temperature could be varied between ~ 8 K and 320 K in a cold finger helium cryostat. Luminescence lifetimes and luminescence spectra were recorded at different temperatures. For the analysis of the radiative decay times the low temperature values under excitation in the *fd* band were used since non-radiative processes are suppressed at low temperatures and excitation in the *fd* band of Pr^{3+} prevents possible delayed emission related to energy transfer from the host lattice.

6.2.2. Choice of investigated systems

The measurements of the radiative decay time of emission have been conducted in a variety of systems, including fluorides and chlorides, phosphates, borates, silicates and aluminates. The synthesis of the materials was done according to conventional solid state synthesis techniques. The phase purity was checked by X-ray powder diffraction. The materials have different crystal structures and a variation of refractive index values between 1.5 and 2.0 at the wavelengths of the Pr^{3+} *d-f* emission (225-315 nm). The values of the refractive indices were taken from the literature or have been estimated using literature data for similar compounds [9-19]. The host lattices investigated have relatively large bandgaps which is required to position the lowest energy *fd* state of Pr^{3+} within the forbidden gap of

the materials. If the *fd* levels are in or close to the edge of the conduction band, (thermally induced) quenching of the luminescence occurs due to photoionization processes. The doping concentrations for Pr^{3+} were low (0.05-0.2 %) in order to prevent cross-relaxation between Pr^{3+} neighbors which shortens the lifetime. The list of materials investigated is summarized in Table 6.1. Note that for many of the materials extensive literature exists on the *d-f* luminescence properties (spectra and decay time) of Pr^{3+}. Nevertheless, it turned out to be very difficult to extract reliable and consistent data on the radiative lifetime of the Pr^{3+} *d-f* emission in many of the materials investigated. Discrepancies in the reported values can result from high Pr-concentrations (quenching by cross-relaxation), elevated temperatures (temperature quenching), host lattice/X-ray excitation (delayed feeding) or other unknown issues related to luminescence decay time measurements. It is for this reason that low-doped systems were synthesized and investigated using the same experimental set-ups, aimed at carefully determining the radiative lifetime of the Pr^{3+} *d-f* emission.

Table 6.1. Radiative decay times for the Pr^{3+} *d-f* luminescence in a variety of host lattices. λ is the emission wavelength in nm, τ_{exp} is the experimental emission lifetime in ns, *n* is the refractive index of the material at the emission wavelength, χ_{full} is the local-field correction value for the full cavity model, χ_{empty} is the local-field correction value for the empty cavity model.

Host lattice	λ (nm)	τ_{exp}(ns)	*n*	χ_{full}	χ_{empty}
$LiYF_4$	225	18.1	1.53 [13]	3.2	2.3
YPO_4	242	11.8	1.75 [14]	5	2.9
$LaPO_4$	228	13.4	1.8 [15]	5.5	3
$LuPO_4$	245	15.4	1.72 [14]	4.7	2.8
$ScBO_3$	265	15.7	1.9 [16]	6.6	3.3
$LuBO_3$	257	16.1	1.9 [16]	6.6	3.3
YBO_3	260	14.5	1.9 [17]	6.6	3.3
$LaBO_3$	245	12.7	1.85 [18]	6	3.2
$YAlO_3$ (YAP)	247	7.5	2.03 [19]	8.5	3.6
$Y_3Al_5O_{12}$ (YAG)	315	23.3	1.9 [13]	6.6	3.3
$Lu_3Al_5O_{12}$ (LuAG)	308	18	1.87 [20]	6.3	3.2
Y_2SiO_5 (YSO)	271	20.4	1.79 [21]	5.4	3
Lu_2SiO_5 (LSO)	270	20	1.82 [22]	5.7	3.1
LaOCl	260	12	2.1 [23]	9.6	3.8

6.3 THEORETICAL BACKGROUND

In a two-level system the spontaneous emission rate (Γ_R) for an electronic transition depends on the emission wavelength, the refractive index n of the host material and the transition dipole moment of the transition, as described by Fermi's Golden Rule for an electric dipole transition [1,20-23]:

$$\Gamma_R = 64\pi^4/3h \cdot \chi \cdot \nu^3 \cdot |\mu_{if}|^2 \qquad (6.1)$$

In this equation χ is the local-field correction factor which is function of n, ν is the energy of the transition (in cm^{-1}) and μ_{if} is the transition dipole moment for the electric dipole transition between the initial and final state. An alternative expression that is often encountered in the literature is:

$$\Gamma_R = 1.5\ 10^{-4} \cdot f \cdot \chi / \lambda^2 \qquad (6.2)$$

where f is the oscillator strength of the transition, and λ is the wavelength of the transition (in nm). For *f-d* transitions the expression:

$$\Gamma_R = 4.34\ 10^{-4} \cdot [|\langle 5d|r|4f\rangle_{eff}|^2] \cdot \chi \cdot \nu^3 \qquad (6.3)$$

has been derived from Fermi's Golden Rule [23]. Here $|\langle 5d|r|4f\rangle_{eff}|$ is the radial integral for the *f-d* transition. Based on Eq. (6.2) sometimes it is argued that there should be a quadratic rather than cubic relation between the radiative lifetime and the emission wavelength [1,24]. However, one should realize that the oscillator strength is linearly proportional to ν [23] which results in an overall increase of Γ_R with ν^3, consistent with Eqs. (6.1) and (6.3).

To describe the influence of the local-field on the transition probability many models have been developed to correct for the interaction of the two-level system with the surrounding dielectric medium [20-22,25]. Mostly, two models are considered, the empty (or real) cavity model for which:

$$\chi = n \cdot [3n^2 / (2n^2+1)]^2 \qquad (6.4)$$

and the full (or virtual) cavity model, which is based on the Lorentz local-field and gives:

$$\chi = n \cdot [(n^2+2) / 3]^2 \qquad (6.5)$$

The difference between the two models is in the refractive index of the cavity where the luminescent ion or molecule resides. For the full cavity model n is assumed to be the same as for the surrounding host, whereas in the empty cavity model it is different [20,25]. Many different models have been developed in addition to these two models,

including microscopic models based on the interaction between the emitter and local dipoles [26,27], but experimental verification of the various models is challenging [28].

It is not known which model is valid for lanthanide luminescence. The real cavity model has been suggested in the literature for intraconfigurational *f-f* emissions of Eu^{3+} [20], while the full cavity model has been proposed for the interconfigurational *d-f* luminescence of Ce^{3+} [1,21,24]. Neither the hand waving arguments used to justify the use of one model over the other, nor the experimental evidence for either model have been convincing [1,20,21,24]. Due to the uncertainties, both local-field correction models will be discussed and compared. From the expressions for the local-field correction one can see that the dependence on the refractive index is much stronger in case of the full (virtual) cavity model. The dependence of the local-field correction factor on the refractive index is illustrated in FIG. 6.1.

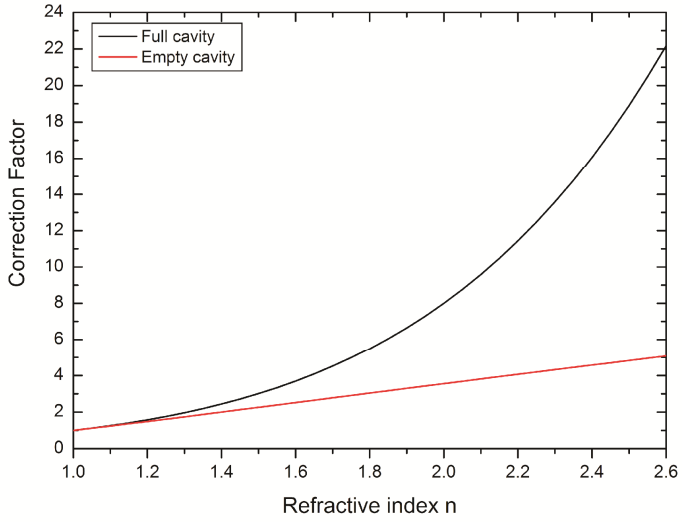

FIG. 6.1. Dependence of the value of the local-field correction factor on the refractive index of the material, for the full (black curve) and empty (red curve) cavity models.

In the past experimental and theoretical work has been done on the relation between the radiative lifetime and emission wavelength for the *d-f* emission from Ce^{3+} and Eu^{2+} [1,20,21,24,29]. In case of the investigations for Eu^{2+} and Ce^{3+} a single *d-f* emission wavelength is used for λ. This is a good approximation since the emission band is confined in narrow spectral region due to transition from the *5d* state to a single *4f* $^7(^8S_{7/2})$ ground

state of Eu^{2+} or two $4f^1$-states separated by only 2000 cm^{-1}, the $^2F_{5/2}$ and $^2F_{7/2}$ states of Ce^{3+}. For Pr^{3+} *d-f* emission is observed over a wider spectral range. The strongest transitions are to the $^3H_4$ ground state, but typically four emission bands can be observed, spanning over a range of about 10 000 cm^{-1}, the energy difference between the $^3H_4$ ground state and the $^1G_4$ excited $4f^2$ state. Typical emission spectra of Pr^{3+} *d-f* emission will be shown in the next section. A more appropriate procedure would involve taking a weighted average of wavelengths and wavelength dependent refractive indices of the material to calculate Γ_R. In view of the larger uncertainties in the various other parameters, we have chosen to use a single emission wavelength and refractive index for the strongest and highest energy emission band in the analysis of the wavelength dependence of the decay time.

6.4 RESULTS AND DISCUSSION

In this section the luminescence properties and luminescence decay times of Pr^{3+} in a variety of host lattices will be shown and compared, where possible, to results reported in the literature. For some host lattices extensive data exist in the literature. The large variation in luminescence lifetimes reported warrants a brief overview of our results on low doped systems and a comparison and discussion with reported literature data to provide a background to the data collected in Table 6.1.

6.4.1. Aluminates

Aluminates are among the most widely studied materials when it comes to *d-f* luminescence of lanthanides. For Ce^{3+}, Eu^{2+} and also Pr^{3+} the *d-f* emission has been studied in a variety of aluminates and resulted in application of Eu^{2+} doped aluminates in fluorescent tubes and afterglow materials [30,31] and Ce-doped aluminates in scintillators crystals [32,33] and white light LEDs [34,35].

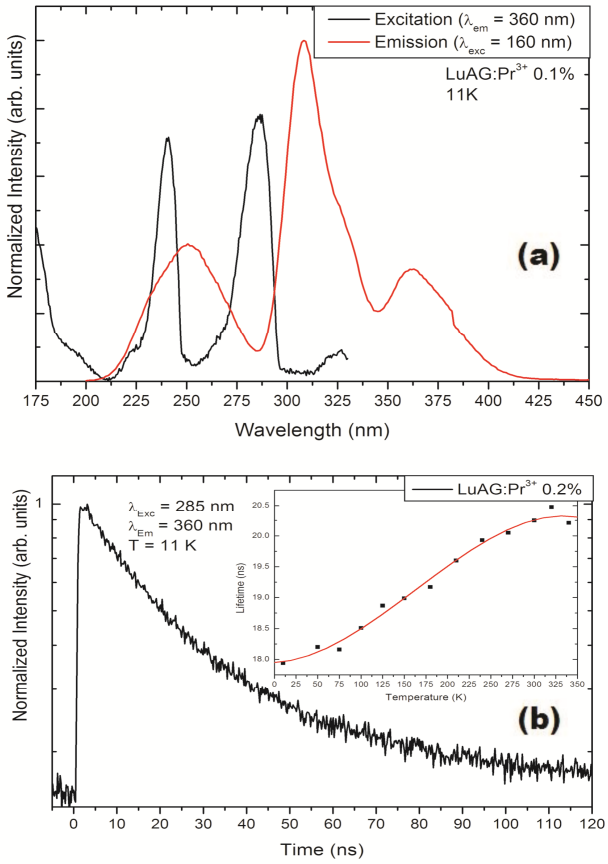

FIG. 6.2. (a) Excitation (black curve) and emission (red curve) spectra of LuAG:Pr^{3+} at 11 K. (b) Luminescence decay curve for Pr^{3+} *d-f* emission in LuAG under direct *fd* excitation at 11 K. The inset shows the temperature dependence of the Pr^{3+} *d-f* emission lifetime.

The luminescence of Pr^{3+} in aluminates has been especially studied in the garnets $Y_3Al_5O_{12}$ (YAG) and $Lu_3Al_5O_{12}$ (LuAG). In the garnet structure there is one crystallographic site for the large lanthanide ion which has dodecahedral symmetry. LuAG:Pr has great potential as a fast scintillator material. In FIG. 6.2 the excitation and emission spectra and the luminescence decay curve are shown for LuAG doped with 0.1% Pr^{3+}. The luminescence spectra are consistent with previous reports: *f-d* excitation bands are observed at 240 nm and 285 nm, while below 190 nm strong host lattice (HL)

absorption is observed, indicating that energy transfer from the HL to the *fd* excited states of Pr^{3+} is efficient. Especially in low-doped systems, where the direct absorption into the *fd* band is weak due to the low activator concentration, a high relative intensity of the host lattice absorption band in the excitation spectrum of the *d-f* emission is a good measure for the energy transfer efficiency to the *fd* state of Pr^{3+}. Emission bands at 308 nm and 364 nm correspond to transitions from the lowest *fd* state to the ($^3H_4$, $^3H_5$) and ($^3H_6$, ^3F_J (J=2-4)) states within the $4f^2$ configuration. The luminescence decay curve at 4 K is single exponential with an 18.2 ns decay time. At room temperature a longer decay time is measured, 21.3 ns. The increase of the decay time with the temperature is peculiar and is plotted in the inset in FIG. 6.2. Probably, thermal occupation of a higher energy *fd* state which has a lower decay rate is responsible for the lengthening of the decay time. The presently found values for the luminescence decay times are consistent with values in the literature, although there is some variation in the values reported. Room temperature decay times between 19 and 25 ns have been reported [36-38]. A careful temperature dependent study on low Pr-doped (0.25%) LuAG crystals reports an 18 ns lifetime at 4 K increasing to 21 ns at RT, consistent with the present findings [36-38].

For YAG:Pr^{3+} 0.1% the excitation and emission band for the lowest energy $^3H_4 \rightarrow fd$ transition is shifted to slightly longer wavelengths, 315 nm in emission and 288 nm in excitation with respect to LuAG. The red-shift of the lowest *fd* state in YAG with respect to LuAG has also been observed for *d-f* emission from Ce^{3+}. For the smaller Lu^{3+}-cation site, compared with Y^{3+}, a larger crystal-field splitting is expected to shift the lowest *fd* to lower energies in LuAG. Calculations have been done to explain this unexpected shift, but have not been able to fully clarify the observations [39]. The luminescence lifetime of the *d-f* emission for Pr^{3+} in YAG is 21.5 ns at 4 K and decreases to 13.5 ns at RT. The drop is explained by temperature quenching which causes the intensity and decay time of the *d-f* emission of Pr^{3+} in YAG to decrease between 150 and 350 K. In the literature decay times between 18 and 22 ns have been reported at 4 K, while at RT similar values (13-14 ns) have been found [40,41].

The perovskite aluminate $YAlO_3$ (Yttrium Aluminate Perovskite or YAP) is not easy to synthesize. Often additional crystalline phases, especially the garnet phase, are formed during the synthesis. In the perovskite structure the lanthanide ion is in a cubic twelve coordination. In FIG. 6.3 the luminescence spectra and luminescence decay curves for the *d-f* emission of Pr^{3+} in YAP are shown. The sample investigated did contain YAG:Pr^{3+} as a second phase, but the higher energy *d-f* emission from Pr^{3+} in YAP could be selectively monitored. The excitation spectra show a double band between 210 and 230 nm for the transition to the lowest energy *fd* state. In the emission spectrum the highest energy band is observed at 247 nm (transition to the $^3H_4$, $^3H_5$ state) and the 280 nm emission band is assigned to the transition to the $^3H_6$, $^3F_2$ states at ~ 5000 cm^{-1} higher energy. The emission spectrum is similar to the spectrum reported in the literature for YAP:Pr^{3+} for a

low doped (0.05%) crystal [42]. At higher doping concentrations the relative intensity of the 247 nm band was observed to decrease due to reabsorption.

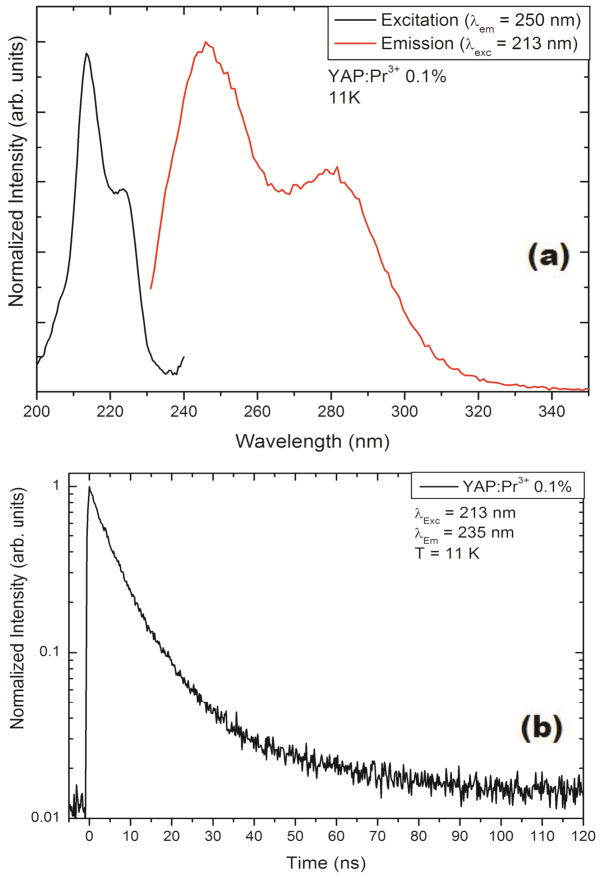

FIG. 6.3. (a) Excitation (black curve) and emission (red curve) spectra of YAP:Pr^{3+} at 11 K. (b) Luminescence decay curve for Pr^{3+} *d-f* emission in YAP under direct *fd* excitation at 11 K.

The luminescence decay curve recorded for the *d-f* emission under *fd* excitation is depicted in FIG. 6.3(b). The decay curve is close to single exponential with a decay time of 7.5 ns. This short decay time is consistent with values reported in the literature. In REF. 42 decay curves of the Pr^{3+} *d-f* emission were reported for pulsed X-ray excitation.

The decay curves showed a multi-exponential decay, with a short time component of about 7-10 ns related to the radiative decay of the *d-f* emission and a longer time component of 100-200 ns, probably due to slower feeding processes related to trapping and de-trapping processes after host lattice excitation. The presently observed decay time of 7.5 ns is consistent with the short radiative lifetimes reported in REF. 42.

6.4.2. Orthoborates

Orthoborates MBO_3 (M=Sc, Lu, Y, La) are well-known host lattices for luminescence studies and have been doped with a variety of trivalent lanthanide ions [43-45]. The crystal structure varies: for the smaller cations (Sc and Lu) the orthoborates have the calcite structures with a six-coordination for the lanthanide ion. YBO_3 has a vaterite related structure with two crystallographic sites for the trivalent ion (6 or 6+6 coordination) and in $LaBO_3$ with the aragonite structure the trivalent ion is in 9-coordination [46]. In FIGS. 6.4-6.7 the luminescence spectra and luminescence decay curves are shown for the Pr-doped orthoborates.

The emission spectra reveal a four-band structure corresponding to transitions from the lowest *fd* state to the $^3H_4$, $^3H_5$, $^3H_6/^3F_2$ and $^3F_3/^3F_4$ states. For the Sc, Lu and Y the four bands are well-resolved due to the small band widths as a result of small Stokes shifts. For $LaBO_3$ the bands are broadened. The positions of the highest energy emission bands are 265 nm (Sc), 257 nm (Lu), 260 nm (Y) and 245 nm (La). The general trend of a shift to higher energies for larger cation sites is explained by a reduction in crystal-field splitting. The slight anomaly for the Lu and Y (the larger Y ion host shows a lower energy Pr^{3+} *d-f* emission) can be related to the change in crystal structure.

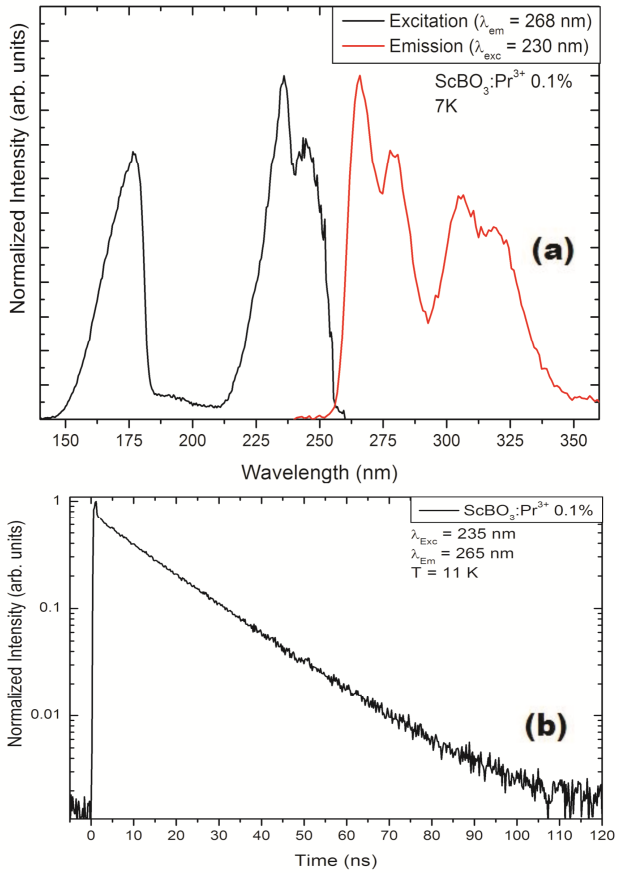

FIG. 6.4. (a) Excitation (black curve) and emission (red curve) spectra of $ScBO_3:Pr^{3+}$ at 7 K. (b) Luminescence decay curve for Pr^{3+} *d-f* emission in $ScBO_3$ under direct *fd* excitation at 11 K.

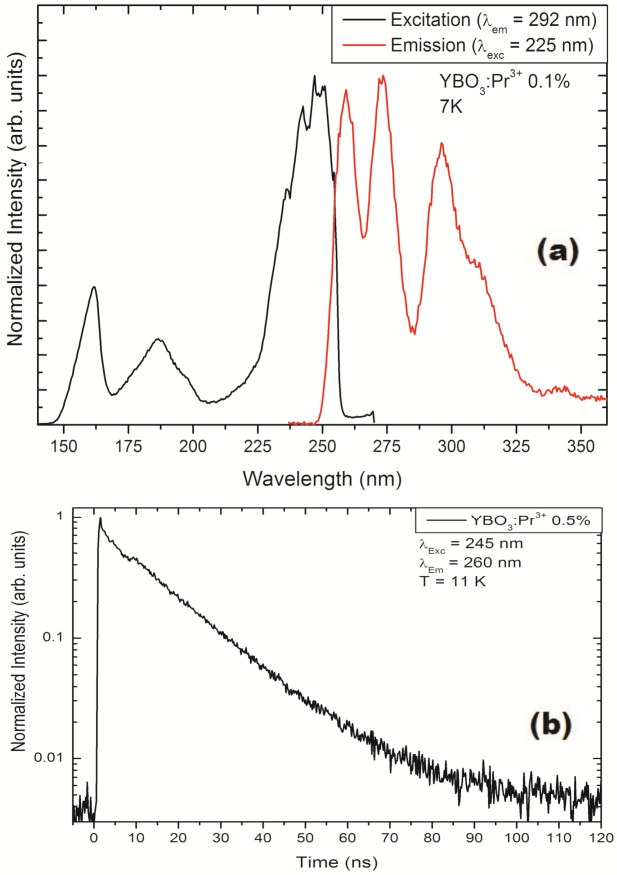

FIG. 6.5. (a) Excitation (black curve) and emission (red curve) spectra of $YBO_3:Pr^{3+}$ at 7 K. (b) Luminescence decay curve for Pr^{3+} *d-f* emission in YBO_3 under direct *fd* excitation at 11 K.

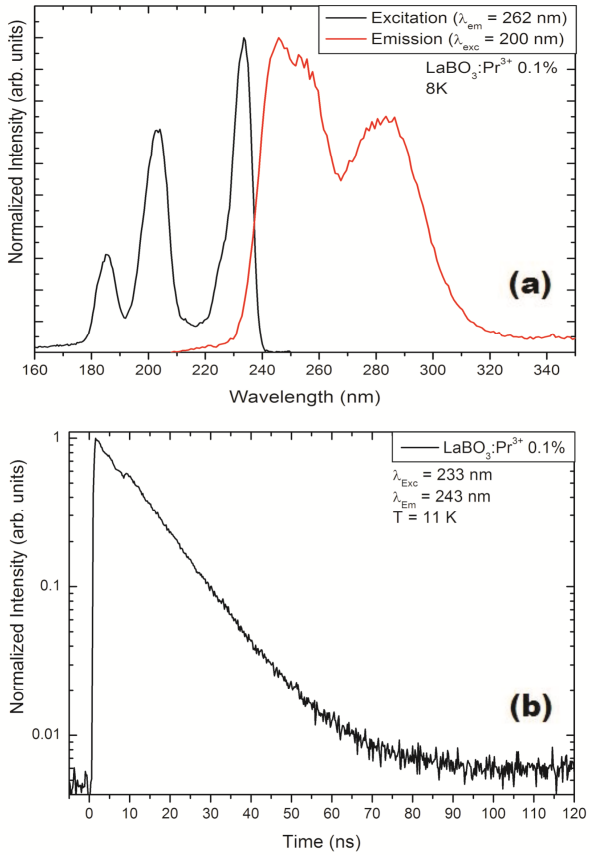

FIG. 6.6. (a) Excitation (black curve) and emission (red curve) spectra of $LaBO_3:Pr^{3+}$ at 8 K. (b) Luminescence decay curve for Pr^{3+} *d-f* emission in $LaBO_3$ under direct *fd* excitation at 11 K.

The excitation spectra of the *d-f* emission reveal a structured lowest energy *fd* band between 210 and 250 nm for Sc, Y and Lu and a host lattice absorption band with an onset at 180 nm (Sc) or 165 nm (Lu, Y). For $LaBO_3$ the crystal-field splitting for the lower site symmetry results in multiple *fd* excitation bands (230 nm and 200 nm). The third band with an onset at 190 nm may be a third crystal-field component or be related to host lattice absorption. The luminescence decay curves of the *d-f* emission show a single exponential decay with decay times of 15.7 ns (Sc), 16.1 ns (Lu), 14.5 ns (Y) and 12.7 ns (La). The decay times decrease with increasing energy of the emitting *fd* state. Note that there is an

irregularity in some of the decay curves (La and Lu) after 10 ns. This is an instrumental artifact. The decay times were determined from single exponential fits starting after the artifact.

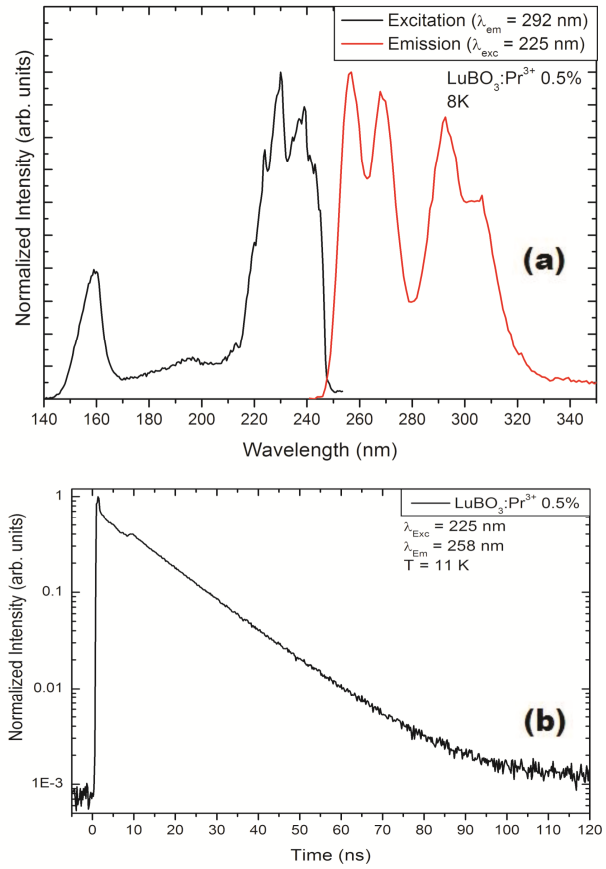

FIG. 6.7. (a) Excitation (black curve) and emission (red curve) spectra of $LuBO_3:Pr^{3+}$ at 8 K. (b) Luminescence decay curve for Pr^{3+} *d-f* emission in $LuBO_3$ under direct *fd* excitation at 11 K.

The luminescence spectra for Pr^{3+} in Sc, Y and La orthoborate have been reported before [43,47]. The emission spectra are consistent with previous results. The presently reported excitation spectra show that the position of the lowest energy *fd* excitation band is

at slightly shorter wavelengths than reported in REF. 43, which can be explained by instrumental limitations due to the use of a Xe-lamp in REF. 43. The luminescence decay time reported for the *d-f* emission in $Lu_{0.8}Sc_{0.2}BO_3$ is shorter (11.9 ns) than the presently reported values (~16 ns for $LuBO_3$ and $ScBO_3$). Both the higher Pr concentration (0.5% in REF. 47) and higher temperature (RT in REF. 47) can be responsible for the shorter lifetimes due to concentration quenching and/or temperature quenching.

6.4.3. Orthophosphates

The orthophosphates have been model systems in the study of *fd* spectra of lanthanide ions. The small Stokes shift for the *d-f* luminescence in YPO_4 allows for the observation of fine structure (zero-phonon lines and vibronic side bands) in the *f-d* excitation and the *d-f* emission spectra [48-51]. Systematic studies of the *fd* spectra for the lanthanides in YPO_4 have aided in the development of theoretical models explaining the energy level structure in $4f^{n-1}5d$ excited states. In FIG. 6.8 the excitation and emission spectra of Pr^{3+} in YPO_4 are shown. The emission spectrum shows two emission bands with maxima at 242 and 260 nm, with a shoulder on the short wavelength side of the 242 nm band. The large spectral width is due to the poor spectral resolution of the emission monochromator. The luminescence spectra for YPO_4:Pr^{3+} reported in the literature show narrow bands with vibrational structure at low temperature with a weaker band around 233 nm and stronger bands peaking at 242 and 260 nm, in agreement with the presently reported spectra [49,51,52]. The excitation spectrum shows fine structure for the lowest energy *fd* band around 225 nm. At higher energies *fd* bands are observed around 180 and 150 nm. The luminescence decay of the *d-f* emission (shown in FIG. 6.8(b)) is single exponential with decay time of 11.8 ns. In the literature longer lifetimes have been reported (17 ns) [53], which may be related to the time resolution of the pulsed xenon lamp used in REF. 53.

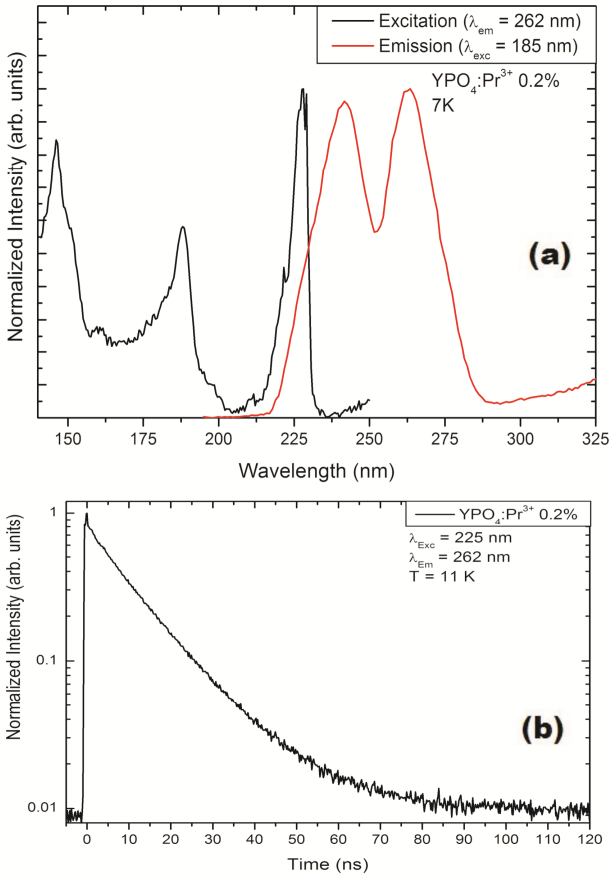

FIG. 6.8. (a) Excitation (black curve) and emission (red curve) spectra of $YPO_4:Pr^{3+}$ at 7 K. (b) Luminescence decay curve for Pr^{3+} *d-f* emission in YPO_4 under direct *fd* excitation at 11 K.

For $LuPO_4$ doped with Pr^{3+} the luminescence spectra are similar and red-shifted by a few nm (FIG. 6.9). The luminescence decay time is longer: 15.4 ns.

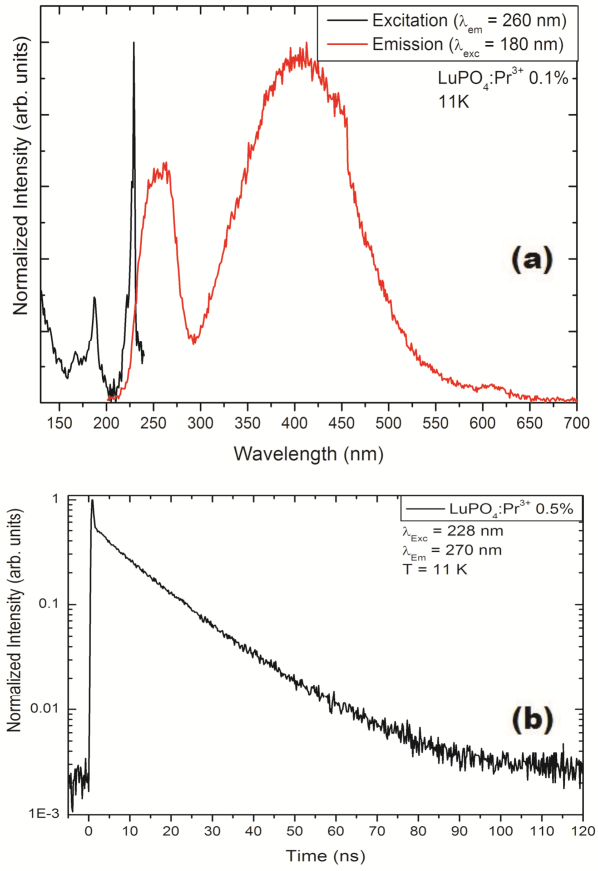

FIG. 6.9. (a) Excitation (black curve) and emission (red curve) spectra of $LuPO_4:Pr^{3+}$ measured at 11 K. (b) Luminescence decay curve for Pr^{3+} *d-f* emission in $LuPO_4$ under direct *fd* excitation at 11 K.

For Pr^{3+} in $LaPO_4$ the lowest energy *fd* level has shifted to higher energies due to a smaller crystal-field splitting. In FIG. 6.10 the luminescence spectra are shown. The excitation and emission bands corresponding to transitions involving the lowest energy *fd* state are around 205 and 228 nm, respectively. The luminescence decay curve for the *d-f* emission is shown in FIG. 6.10 (b). The decay is single exponential with a decay time of 13.4 ns. Previous work on $LaPO_4:Pr^{3+}$ has shown interesting Pr^{3+} luminescence in $LaPO_4$, including emission from the $^1S_0$ level in competition with non-radiative decay to the lowest *fd* state [54]. The luminescence spectra are in agreement with those in the

literature [54,55]. As far as we are aware of, no lifetime has been reported for the *d-f* luminescence for Pr^{3+} in $LaPO_4$.

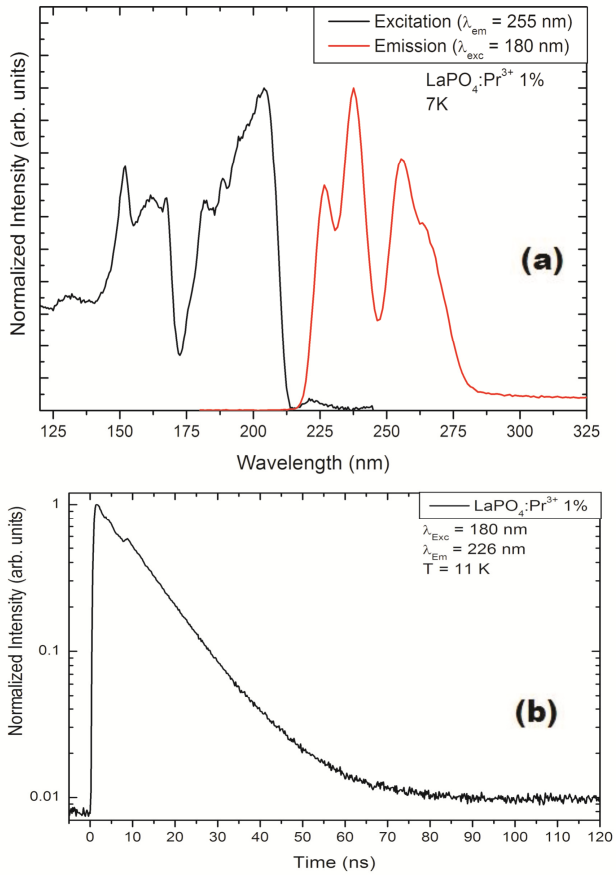

FIG. 6.10. (a) Excitation (black curve) and emission (red curve) spectra of $LaPO_4:Pr^{3+}$ at 7 K. (b) Luminescence decay curve for Pr^{3+} *d-f* emission in $LaPO_4$ under direct *fd* excitation at 11 K.

6.4.4. Oxyorthosilicates

The oxyorthosilicates Y_2SiO_5 (YSO) and Lu_2SiO_5 (LSO) host lattices doped with lanthanides are used in a variety of applications, including CRT phosphors, scintillators and optical data storage [32]. LSO and the high temperature modification of YSO have the same (monoclinic) crystal structure in which there are two crystallographic sites for the rare earth ions with 6 and 7 coordination by oxygen. Luminescence from Pr^{3+} in both YSO and LSO has been studied extensively [52,56-59].

In FIG. 6.11 the luminescence spectra and decay curve are shown for YSO doped with 0.1% of Pr^{3+}. In the excitation spectrum *fd* excitation bands are observed around 248 and 220 nm. Below 200 nm the host lattice absorption starts. The highest energy emission band has a maximum at 271 nm and is assigned to the transition to the $^3H_{4,5}$ ground state. For Pr^{3+} in LSO the luminescence spectra are very similar. In FIG. 6.11(b) the luminescence decay curve of the *d-f* emission from Pr^{3+} is shown. The decay is single exponential with a decay time of 20.4 ns. The low temperature decay time of the *d-f* emission is also the same for Pr^{3+} in LSO and YSO, for Pr^{3+} in LSO a decay time of 20 ns is found. For YSO the room temperature decay is very similar to the room temperature decay time, 19.5 ns. For Pr^{3+} in LSO temperature quenching reduces the decay time. The presently reported spectra are in good agreement with spectra reported in the literature [52,56-59]. The luminescence decay times reported in the literature vary. For Pr^{3+} in LSO low temperature decay times of 25 ns [56] or 7 and 26 ns [57] have been reported. At room temperature the decay is shortened by thermal quenching to 6 ns [56]. For YSO the decay time for the *d-f* emission from Pr^{3+} has been reported to be 30 ns [59] and 17 ns [58]. The latter value is close to the presently observed 19.5 ns decay time.

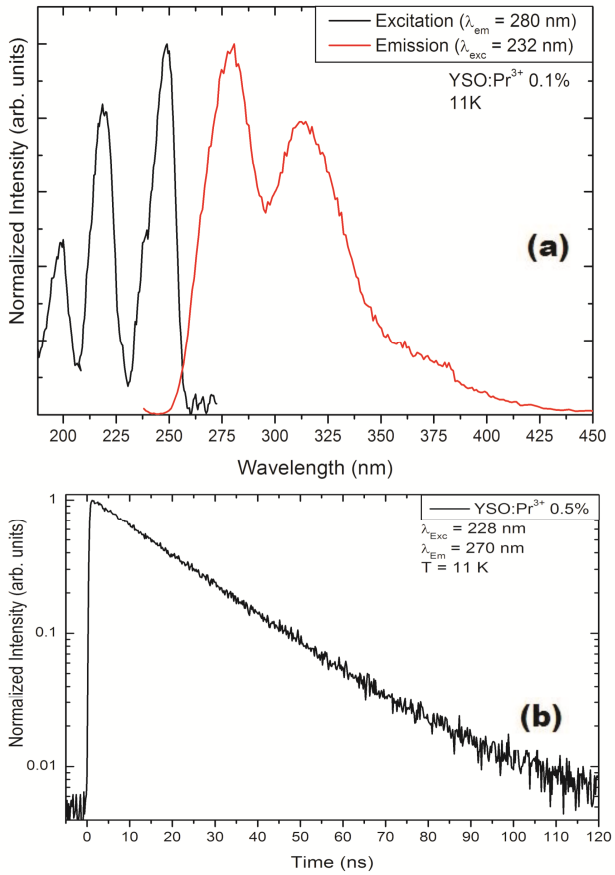

FIG. 6.11. (a) Excitation (black curve) and emission (red curve) spectra of YSO:Pr^{3+} at 11 K. (b) Luminescence decay curve for Pr^{3+} *d-f* emission in YSO under direct *fd* excitation measured at 11 K.

6.4.5. Other host lattices

In addition to the classes of host lattices discussed above, the *d-f* luminescence for Pr^{3+} has been investigated in two other compounds: $LiYF_4$ and LaOCl. $LiYF_4$ is a model system for studies in lanthanide spectroscopy, both for providing insight in intraconfigurational $4f^n$-$4f^n$ and interconfigurational $4f^n$-$4f^{n-1}5d$ transitions.

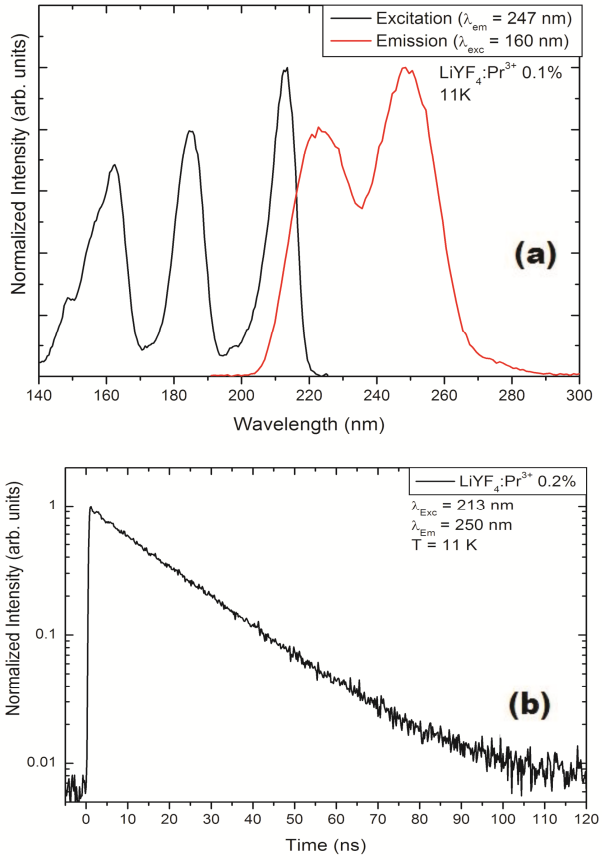

FIG. 6.12. (a) Excitation (black curve) and emission (red curve) spectra of $LiYF_4:Pr^{3+}$ at 11 K. (b) Luminescence decay curve for Pr^{3+} *d-f* emission in $LiYF_4$ under direct *fd* excitation at 11 K.

In FIG. 6.12 the excitation and emission spectra for Pr^{3+} in $LiYF_4$ are shown. The emission spectrum shows bands around 225 and 248 nm while the excitation spectrum consists of three bands between 140 and 220 nm. The emission bands can be assigned to transitions from lowest energy *fd* state to the $^3H_4$ and $^3H_5$ levels (225 nm) and the $^3H_6$ and $^3F_{3,4}$ levels (248 nm). The large spectral width is due to the poor resolution of the emission monochromator. Higher resolution emission spectra have been reported in which sharp zero-phonon lines and vibronic lines are observed and the transitions to the $^3H_4$, $^3H_5$ and $^3H_6$ levels are spectrally well-resolved [51]. Careful spectroscopic investigations have also

revealed fine structure in the excitation spectra, which cannot be observed in FIG. 6.12 due to the low spectral resolution of the experimental set-up. For the present study the vibronic features are not important. The spectra are in agreement with those reported in the literature. The luminescence decay curve shows a purely single exponential decay with a characteristic decay time of 18.1 ns. In the literature different decay times have been reported for the *d-f* emission of Pr^{3+} in $LiYF_4$, sometimes significantly different from the presently determined value of 18.1 ns (e.g. 26 ns in REF. 53) and sometimes quite similar (e.g. 19 ns in REF. 60). As discussed above, based on careful experiments with a fast response (~ 200 ps) detection system on a low-doped system, where lengthening of the decay time by re-absorption or shortening by concentration quenching is prevented, the presently reported decay times are considered to be reliable.

For Pr^{3+} in LaOCl extensive literature exists on the splitting of the $4f^2$ levels, but research on *fd* transitions is limited. In FIG. 6.13(a) the excitation and emission spectra are shown. The excitation onset is just below 240 nm and *fd* excitation bands are observed at 225 nm (with a shoulder on the short wavelength side) and 200 nm. The absence of host lattice absorption bands in the excitation spectrum of the *d-f* emission shows that energy transfer from the host lattice to the *fd* excited state is inefficient. Broad *d-f* emission bands are observed between 240 and 300 nm. The luminescence decay curves are close to single exponential with a decay time of ~ 12 ns. To the best of our knowledge, in the literature no *d-f* emission from Pr^{3+} has been reported. VUV excitation spectra of *f-f* emissions in REF. 61 show three *fd* excitation bands between 240 and 180 nm, similar to the presently reported excitation spectrum.

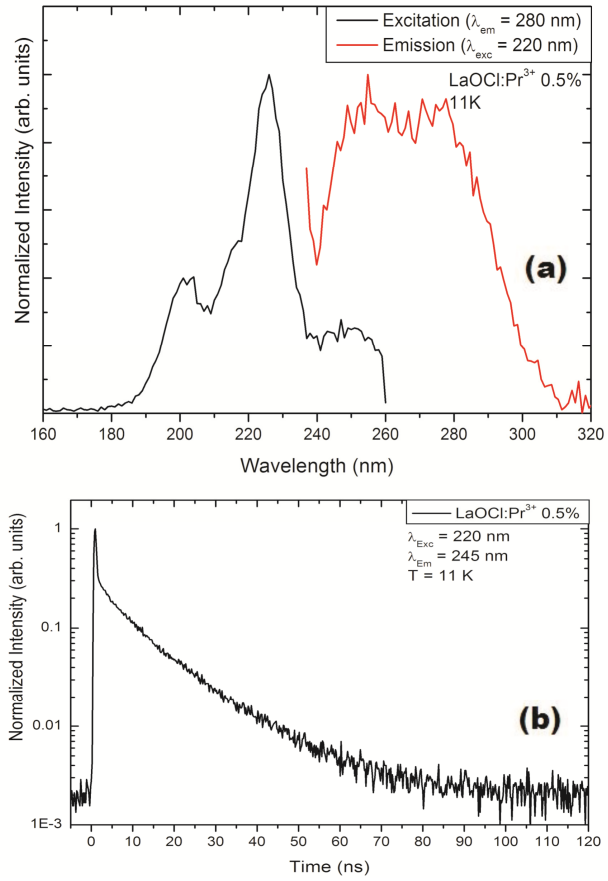

FIG. 6.13. (a) Excitation (black curve) and emission (red curve) spectra of LaOCl:Pr^{3+} at 11 K. (b) Luminescence decay curve for Pr^{3+} *d-f* emission in LaOCl under direct *fd* excitation at 11 K.

6.5 GENERAL DISCUSSION

The radiative lifetimes of the *d-f* emission for Pr^{3+} in a variety of host lattices vary from 7.5 ns to 23.3 ns. In Table 6.1 the lifetimes and information on the emission wavelength of the highest energy emission band and the refractive index are collected. In FIG. 6.14 the lifetimes are plotted as a function of emission wavelength. Clearly, there is a trend showing that longer lifetimes are observed for longer emission wavelengths. The scatter in the data is however large. In order to be able to better compare the measured lifetimes with the theoretical models, the data have been re-plotted as $\chi.\tau$ (the radiative lifetimes from Table 6.1 multiplied by χ to correct for the local-field).

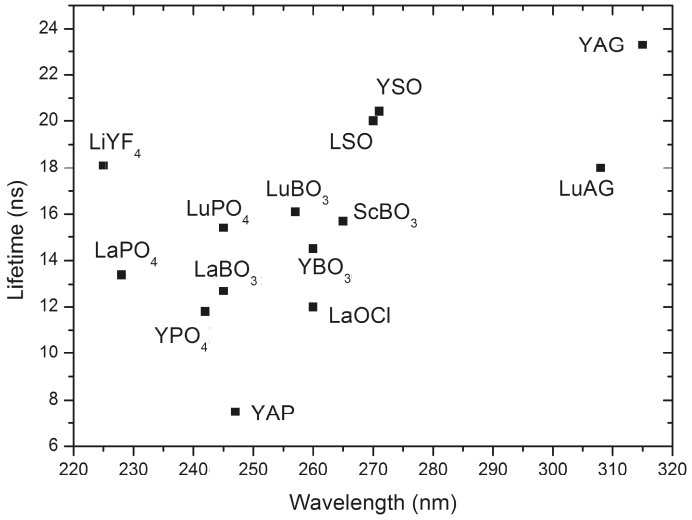

FIG. 6.14. Dependence of the uncorrected radiative lifetime on the emission wavelength of investigated systems.

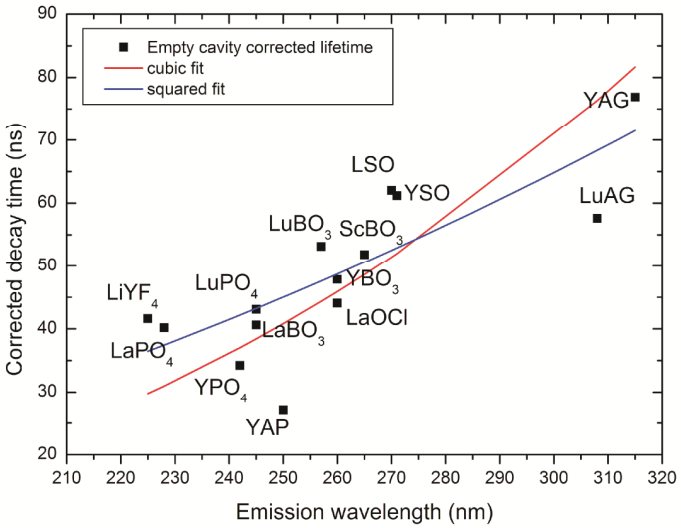

FIG. 6.15. Dependence of the corrected radiative lifetime on the emission wavelength of investigated systems, using the empty cavity correction.

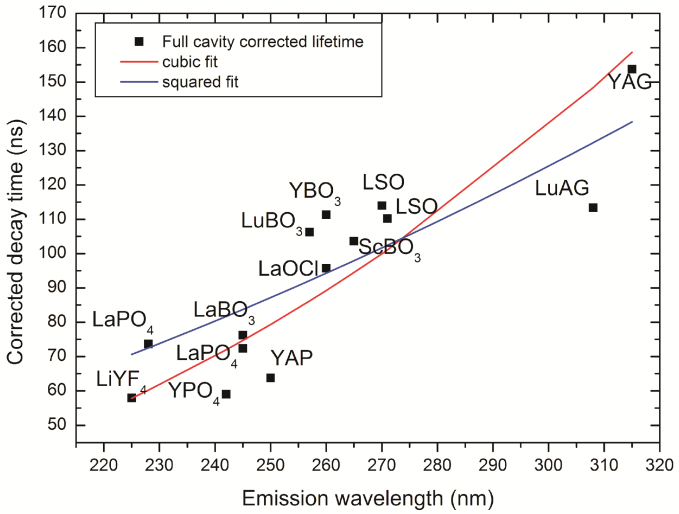

FIG. 6.16. Dependence of the corrected radiative lifetime on the emission wavelength of investigated systems, using the full cavity correction.

FIGURE 6.15 shows the results using the correction factor for the empty cavity model, while the results after correction for the full cavity model are shown in FIG. 6.16. The theoretically predicted increase in radiative lifetime for longer emission wavelength is more clearly observed after correcting for local-field effects. Still, there is a significant scatter of the data points. Using the correction factor predicted by the full cavity model (FIG. 6.16) seems to be slightly better (less scatter in the data points) than for the empty cavity model (FIG. 6.15), but the difference is not sufficient to decide which of the models is the correct one. In order to compare the results with theory, the wavelength dependence of the lifetimes, after correction for the local-field, was fitted to both a squared and a cubic wavelength dependence. The blue lines in FIGS. 6.15 and 6.16 represent the fits to a λ^2, while the red lines give the fits to a λ^3 dependence. The agreement is better for the λ^3 dependence, as expected (see Theory). For the λ^2 fits the data point on short wavelength side (below 260 nm) are below the line for the best fit while for longer wavelength the data points are above the line. Clearly, the wavelength dependence of the radiative lifetime is steeper than a λ^2 dependence. The data points for the λ^3 fit are scattered around the line and data points are found above and below the line over the full wavelength range, indicating that the theoretically predicted λ^3 dependence gives a better agreement with experiment. From the scatter in the data around the λ^3 line it is also clear that Eq. (6.3) cannot be used for an accurate calculation of the radiative lifetime once the emission wavelength of the *d-f* emission and the refractive index of the host are known. Below we will discuss the origin for this observation. The quality of the fit for the data corrected using the full cavity model is slightly better than for the data corrected using the empty cavity model, favoring the use of χ for the full cavity model (Eq. 6.5) for *d-f* emission, in line with the results in REF. 20. Again, it should be noted that the large scatter of the data does not allow for definite conclusions.

It is important to understand the factors that contribute to the deviation between experiment and theory. We see two main contributions. The first is the uncertainty in the values for the refractive index. It is difficult to find accurate numbers for the refractive index for many of the crystalline hosts in the UV part of the spectrum. The data collected in Table 6.1 are the most reliable estimates for n that could be obtained. Often n had to be estimated from values given for similar host lattices or values for n in the visible range. Because of the strong variation of χ with n, a more accurate determination of the refractive index will improve the reliability of the experimental data points. This will also help to provide support for which of the models for χ is correct.

A second source for the deviation of the experimental data from a smooth λ^3 dependence is the variation in the transition dipole moment $\langle 5d|r|4f\rangle_{eff}$. For a perfect λ^3 dependence, there should be no change in transition dipole moment. In first approximation this assumption is justified. The *f-d* transition is a fully allowed electric dipole transition. For forbidden transitions the local environment has a strong influence on the radiative

lifetime since the partial lifting of selection rules through e.g. spin-orbit coupling or admixture of opposite parity states depends on the nature of surrounding neighbors and symmetry of the local ligand field. For parity allowed transitions there is no such influence. For a pure *d-f* transition the transition dipole moment is constant. For the free ion the transition dipole moment for the *f-d* transition on Pr^{3+} has been calculated to be 0.0271 [22]. However, through the nephelauxetic effect delocalization of the *5d* orbital over the ligands can reduce the transition dipole moment below the free ion value. Differences in covalency will affect the delocalization and cause a variation in $|\langle 5d|r|4f\rangle_{eff}|$. In the literature this is recognized. In studies on the wavelength dependence of the lifetime of the *d-f* emission for Eu^{2+} [29] and Ce^{3+} [22] the transition dipole moments were calculated from the measured lifetimes, using Eq. (3) assuming a full cavity model for χ. The variation in the calculated transition dipole moments for Eu^{2+} and Ce^{3+} in REFS. 22,29 is large, 30-40%, very similar to the presently observed deviation of the data points in FIGS. 6.15 and 6.16 from the fitted curves representing the λ^3 dependence. Based on these observations we can conclude that the experimentally observed wavelength dependence of the lifetime of the *d-f* emission for Ce^{3+}, Eu^{2+} and Pr^{3+} follows Eq. (3) but there is a 30-40% scatter, to which both uncertainties in *n* and a variation in $|\langle 5d|r|4f\rangle_{eff}|$ between host lattices contributed. To improve the modeling a more accurate determination of *n* and a better insight in the variation of $|\langle 5d|r|4f\rangle_{eff}|$ in different host lattices, e.g. through *ab initio* calculations of the wave functions in the *4f* ground state and $4f^{n-1}5d$ excited states [39] can contribute.

In addition to the two major factors contributing to the deviation of the data points from the fits to Eq. (3), several minor sources can be identified. In our modeling we used a single emission wavelength for the Pr^{3+} *d-f* emission. Clearly, the emission covers a wide spectral region (wider than for Eu^{2+} and Ce^{3+}) with the most intense bands spread over about 10 000 cm^{-1}. As discussed above, it would be more correct to calculate a wavelength and intensity weighted λ^3 factor from high resolution emission spectra. This laborious procedure is however estimated to reduce the scatter in the data by less than 10%. The strongest emission bands always correspond to transitions at the highest energies and the variation in the intensity distribution for the $4f5d\text{-}4f^2$ emission spectra is not large (see FIGS. 6.2-6.13). Even more accurate would be to also include the wavelength dependence of *n* in the analysis. As long as the uncertainty in the other parameters (values of *n* and $|\langle 5d|r|4f\rangle_{eff}|$) is so much larger, no effort was made to include these refinements. The accuracy of the measured radiative lifetimes is also important. As discussed, care was taken to determine the radiative lifetime with the highest possible accuracy by systematic research on low-doped systems at cryogenic temperatures and using sensitive and fast (sub-ns) detection schemes. The high quality and single exponential character of the decay curves give confidence that the error in the reported radiative lifetimes is small. In many cases the lifetimes were determined for multiple combinations of *f-d* excitation and *d-f* emission wavelengths giving rise to very consistent data, with variations in the lifetimes for

d-f emission for Pr^{3+} in a specific host lattice well below 5%. The accuracy of the experimentally determined lifetimes is clearly not a bottleneck. Note, however, that careful measurements are needed, as values reported in the literature for lifetime of the *d-f* emission in a specific host can vary strongly due to a variety of factors (e.g. excitation over the band gap, concentration quenching, temperature quenching, and limited time resolution of the system).

The best fit of the experimentally measured radiative lifetimes has been obtained assuming a full cavity model for the local-field correction and a λ^3 dependence. The fit parameter for $|\langle 5d|r|4f\rangle_{eff}|$ for the best fit (red curve in FIG. 6.16) is 0.0214 nm. This value is smaller than the free ion value of 0.0271. The 20% reduction can be explained by the nephelauxetic effect. Based on the present results a reasonable estimate for the decay time of the *d-f* emission can be obtained from:

$$\Gamma_R = 1/\tau = 4.34\ 10^{-4} \cdot [|\langle 5d|r|4f\rangle_{eff}|^2] \cdot \chi \cdot \nu^3 \qquad (6.3)$$

with $|\langle 5d|r|4f\rangle_{eff}| = 0.0214$ and $\chi = n \cdot [(n^2+2) / 3]^2$. To estimate the fastest decay time possible for Pr^{3+} we need to consider that the short wavelength limit for the *d-f* emission from Pr^{3+} is about 220 nm, taking into account a small Stokes shift and the fact that the *fd* state of Pr^{3+} needs to be below the $^1S_0$ $4f^2$ level of Pr^{3+} around 212 nm [26]. The refractive index of the material at the emission wavelength should be as large as possible. An upper limit is estimated to be ~ 1.8 for a material in which the *d-f* emission is at high energies. Based on these considerations, the shortest radiative lifetime of the Pr^{3+} *d-f* emission at 220 nm in a material with an assumed refractive index of 1.8 would be about 6 ns.

6.6 CONCLUSIONS

The luminescence decay times of *d-f* emission of Pr^{3+} have been investigated in a variety of host lattices. The radiative decay times vary between 7.5 and 23 ns and show a clear correlation with wavelength: longer lifetimes are observed for longer wavelength emission. The general trend is in agreement with the Fermi's Golden Rule but the scatter in the data is significant. The best agreement between experiment and theory is obtained for a λ^3 wavelength dependence and using the full cavity model for the local-field correction factor χ. The main contribution to deviations from the theoretical relation are the lack of reliable values for the refractive index n (needed to calculate χ) in the UV spectral region and a variation in the transition dipole moment for the *d-f* transition for Pr^{3+} in different host lattices. A more reliable determination of n may improve the accuracy, but the variation in transition dipole moment is inherent to *d-f* transitions and has also been observed for Eu^{2+} and Ce^{3+}. Since the transition dipole moment varies, a calculation of the

radiative lifetime of *d-f* is not possible from the emission wavelength and refractive index. Still, radiative lifetimes can be estimated using an average value for $\langle 5d|r|4f\rangle_{eff}$ of 0.0214 nm. Using this value, the shortest lifetime that can be achieved for *d-f* emission from Pr^{3+} is estimated to be ~ 6ns. This gives a lower limit for the radiative lifetime in inorganic scintillators based on luminescent ions.

REFERENCES

[1] A. Lempicki, A.J. Wojtowicz, *J. Lumin.* **60&61** (1994) 942-947

[2] P. Dorenbos, in: S. Tavernier et al. (Eds.), *Radiation Detectors for Medical Applications*, Springer, 2006, pp. 191-207

[3] L. Pidol, A. Kahn-Harari, B. Viana, B. Ferrand, P. Dorenbos, J.T.M. de Haas, C.W.E. van Eijk, E. Virey, *J. Phys.: Condens. Matter* **15** (2003) 2091-2102

[4] L. Pidol, B. Viana, A. Galtayries, P. Dorenbos, *Phys. Rev. B* **72** (2005) 125110

[5] A. Zych, A. Leferink op Reinink, K. van der Eerden, C. de Mello Donegá, A. Meijerink, *J. Alloys Compd.* 509 (2011) 4445-4451

[6] A. Zych, C. de Mello Donegá, A. Meijerink, *Opt. Mater.* **33** (2011) 347-354

[7] P. Dorenbos, *J. Lumin.* **91** (2000) 155-176

[8] G. Zimmerer, *Nucl. Instrum. Methods A* **308** (1991) 178-186

[9] D.E. Castleberry, A. Linz, *Appl. Opt.* **14** (1975) 2056-2056

[10] G.E. Jellison, L.A. Boatner, C. Chen, *Opt. Mater.* **15** (2000) 103-109

[11] W. Mayr, T. Jüstel, P.J. Schmidt, *US Patent no. 20090032772* May 2 (2009)

[12] F. Qin, R.K. Li, *J. Cryst. Growth* (2010) in press, doi:10.1016/j.jcrysgro.2010.08.037

[13] S. Levene, C.R. Ronda, *US Patent no. 20100032578* November 2 (2010)

[14] J. Fan, Z. Lin, L. Zhang, G. Wang, *J. Phys. D: Appl. Phys.* **39** (2006) 3226-3229

[15] S. Baccaro, A. Cecilia, M. Montecchi, T. Malatesta, F. de Notaristefani, S. Torrioli, F. Vittori, *Nucl. Instrum. Methods A* **406** (1998) 479-485

[16] Y. Kuwano, K. Suda, N. Ishizawa, T. Yamada, *J. Cryst. Growth* **260** (2004) 159-165

[17] C.L. Sun, J.F. Li, C.H. Hu, H.M. Jiang, Z.K. Jiang, *Eur. Phys. J. D* **39** (2006) 303-306

[18] http://www.apace-science.com/proteus/lso.htm

[19] J. Holsa, P. Porcher, *J. Less-Common Met.* **112** (1985) 121-125

[20] D. Toptygin, *J. Fluoresc.* **13** (2003) 201-219

[21] C.-K. Duan, M.F. Reid, *Curr. Appl. Phys.* **6** (2006) 348-350

[22] T. Chen, C.-K. Duan, S. Xia, *J. Alloys Compd.* **439** (2007) 363-366

[23] B. Henderson, G.F. Imbusch, *Optical Spectroscopy of Inorganic Solids*, Clarendon Press-Oxford, 1989 pp. 315-386
[24] E. Zych, in: H. Singh Nalwa, L. Shea Rohwer (Eds.), *Luminescence and Scintillation of Inorganic Phosphor Materials*, Handbook of Luminescence, Display Materials, and Devices vol. 2, American Scientific Publishers, 2003, pp. 251-300
[25] K. Dolgaleva, R.W. Boyd, P.W. Milonni, *J. Opt. Soc. Am. B* **24** (2007) 516-521
[26] I. Sokólska, S. Kück, *Chem. Phys.* **270** (2001) 355-362
[27] M.E. Crenshaw, *Phys. Rev. A* **78** (2008) 053827
[28] S.F. Wuister, C. de Mello Donegá, A. Meijerink, *J. Chem. Phys.* **121** (2004) 4311
[29] S.H.M. Poort, A. Meijerink, G. Blasse, *J. Phys. Chem. Solids* **58** (1997) 1451-1456
[30] D. Dacyl, D. Uhlich, T. Justel, *Cent. Eur. J. Chem.* **7(2)** (2009) 164-167
[31] C. Ronda, in: C. Ronda (Ed.), *Emission and Excitation Mechanisms of Phosphors*, Luminescence: From Theory to Applications, WILEY-VCH, 2008, pp. 1-34
[32] E. Zych, A. Zych, J. Zhang, Sh. Wang, *J. Alloys Compd.* **451** (2008) 286-289
[33] J.M. Ogiegło, A. Zych, K.V. Ivanovskikh, T. Justel, C. Ronda, A. Meijerink, submitted to: *Phys. Rev. B*
[34] V. Bachmann, C. Ronda, A. Meijerink, *Chem. Mater.* **21** (2009) 2077-2084
[35] K. Li, Ch. Shen, *Proc. SPIE* **7658** (2010) 76583K
[36] T. Yanagida, M. Sato, K. Kamada, Y. Fujimoto, Y. Yokota, A. Yoshikawa, V. Chani, *Optics Mat.* **33** (2011) 413
[37] V. Babin, V. Gobrbenko, A. Krasnikov, A. Makhov, M. Nikl, S. Zazubovich and Yu. Zorenko, *Radiation Meas.* **45** (2010) 415
[38] Y. Shi, X.Q. Feng, Y.B. Pan, J. Zhou, Y. Huang, Z.H. Gao, *Radiation Meas.* **45** (2010) 457
[39] A.B. Munoz-Garcia, J.P. Pascual, Z. Barandiaran, L. Seijo, *Phys. Rev B* **82** (2010) 064114
[40] H. Ogino, A. Yoshikawa, M. Nikl, A. Krasnikov, K. Kamada, T. Fukuda, *J. Crystal Growth* **287** (2006) 335
[41] J. Pejchal, M. Nikl, E. Mihokova, J.A. Mares, A. Yoshikawa, H. Ogino, K.M. Schillemat, A. Krasnikov, A. Vedda, K. Nejezchleb, V. Mucka, *J. Phys.: Appl. Phys* **42** (2009) 055117
[42] T. Yanagida, K. Kamada, Y. Fujimoto, M. Sugiyama, Y. Furuya, A. Yamaji, Y. Yokota, A. Yoshikawa, *Nucl. Instr. Meth. Phys. Res. A* **523** (2010) 1020
[43] G. Blasse, J.P.M. van Vliet, J.W.M. Verwey, R. Hoogendam, M. Wiegel, *J. Phys. Chem. Solids* **50** (1989) 583-585
[44] G. Blasse, G.J. Dieksen, *J. Inorg. Chim. Acta* **145** (1988) 303-308
[45] A.M. Srivastava, M.T. Sobieraj, S.K. Ruan, E. Banks, *Mat. Res. Bull.* **21** (1986) 1455-1463
[46] A. Wolfert, E.W.J.L. Oomen, G. Blasse, *J. Lumin.* **31** (1984) 308
[47] Y. Wu, D. Ding, Sh. Pan, F. Yang, G. Ren, *J. Alloys Compd.* **509** (2011) 7139-7142

[48] R.T. Wegh, W. van Klinken, A. Meijerink, *Phys. Rev. B* **64** (2001) 045115
[49] L. van Pieterson, M.F. Reid, R.T. Wegh, S. Soverna, A. Meijerink, *Phys. Rev. B* **65** (2002) 045113
[50] L. van Pieterson, M.F. Reid, G.W. Burdick, A. Meijerink, *Phys. Rev. B* **65** (2002) 045114
[51] P.S. Peijzel, P. Vergeer, A. Meijerink, M.F. Reid, L.A. Boatner, G.W. Burdick, *Phys. Rev. B* **71** (2005) 045116
[52] M. Nikl, A. Yoshikawa, A. Vedda, T. Fukuda, *J. Cryst. Growth* **292** (2006) 416
[53] M. Laroche, S. Girard, J. Margerie, R. Moncorge, M. Bettinelli, E. Cavalli, *J. Phys.: Condens. Matter* **13** (2001) 765
[54] A.M. Srivastava, A.A. Setlur, H.A. Comanzo, W.W. Beers, U. Happek, P. Schmidt, *Opt. Mater.* **33** (2011) 292
[55] E. Nakazawa, F. Shiga, *Jpn. J. Appl. Phys.* **42** (2003) 1642
[56] M. Nikl, H. Ogino, A. Yoshikawa, E. Mihokova, J. Pejchal, A. Beitlerova, A. Novoselov, T. Fukuda, *Chem. Phys. Lett.* **410** (2005) 218
[57] K. Yang, M.A. Spurrier, H. Rothfuss, L. Eriksson, C.L. Melcher, *IEEE Trans. Nucl. Science* **56** (2009) 968
[58] A. Novoselov, H. Ogino, A. Yoshikawa, M. Nikl, J. Pejchal, J.A. Mares, A. Beitlerova, C.D. Ambrosio, T. Fukuda, *J. Cryst. Growth* **287** (2006) 309
[59] P. Dorenbos, M. Marsman, C.W.E. van Eijk, M.V. Korzhik, B.I. Minkov, *Rad. Effects and Defects in Solids* **135** (1995) 823
[60] L. van Pieterson, M.F. Reid, R.T. Wegh, A. Meijerink, *J. Chem Phys.* **115** (2001) 9382
[61] Th. Troster, W.B. Holzapfel, *Phys. Rev. B* **66** (2002) 075114

7

Analysis of the shift of zero-phonon lines for *f-d* luminescence of lanthanides in the relation to the Dorenbos model

ABSTRACT

The Dorenbos relation is an empirical model that relates the position of the lowest *fd* level of any lanthanide ion with that of Ce^{3+} in the same host lattice. The relation is widely used to estimate the energy of *fd* levels of trivalent lanthanide ions in a given host lattice based on the peak position of the lowest *fd* level of at least one of the lanthanide ions in that host. The energy of *fd* levels is determined from peak maxima in excitation and emission spectra. In this chapter we use the position of zero-phonon lines (ZPLs) as input to investigate the accuracy of the Dorenbos relation. To this end, the ZPL positions of the *fd* bands for trivalent lanthanide ions in four different host lattices (CaF_2, $Y_3Al_5O_{12}$, $LiYF_4$, and YPO_4) were obtained and used as input in the Dorenbos relation. The results are compared to those obtained through the standard procedure using band maxima. The data indicate that the ZPL approach gives more accurate estimates for the position of the lowest *fd* level with standard deviations that are 2-3 times smaller than those obtained for band maxima. The results confirm the concept of the Dorenbos model (constant energy difference between the *fd* levels of lanthanides) and show that the accuracy is even better than previously reported. The main cause for the larger deviation from positions of band maxima is related to a larger inaccuracy in determining band maxima compared to ZPLs.

7.1. INTRODUCTION

The knowledge of the position of the lowest *fd* level of a lanthanide (Ln) ion in a host lattice with respect to the $4f^n$ energy levels and the conduction and valence bands makes it possible to predict luminescence properties of Ln-doped compounds such as the position of excitation and emission bands, quenching of *d-f* luminescence via photoionization or multi-phonon relaxation and trapping and de-trapping of charge carriers from the valence and conduction band [1-8]. The position of the lowest *fd* level of any trivalent Ln ion in an inorganic host lattice can be estimated using an empirical relation proposed by Dorenbos [1-3], which is expressed as

$$E(Ln, A) = 49340 \text{ cm}^{-1} - D(A) + \Delta E^{Ln,Ce} \quad (1)$$

where *E(Ln, A)* is the peak position of the lowest *fd* band of a Ln ion in a given host lattice A. The term *D(A)* represents the crystal-field depression for the host lattice A, which is the lowering of the energy of the *fd* state of Ce^{3+} ion in the host lattice with respect to the free ion value. $\Delta E^{Ln,Ce}$ is the energy difference between the lowest *fd* states of a Ln^{3+} ion and Ce^{3+} ion, which is taken as a host lattice independent constant. It was realized already by Blasse that the energy difference between the *fd* states of different of lanthanide ions, specifically Ce, Pr and Tb, is the same in different host lattices. Systematic studies were carried out by Dorenbos and resulted in a better understanding and a more accurate determination of the energy differences for all lanthanides. The values of $\Delta E^{Ln,Ce}$ and *D(A)* are known, based on analysis of data for a large number of materials [1-3], allowing *E(Ln, A)* for any Ln^{3+} ion in these materials to be estimated. The position of the maximum of the lowest *fd* band of a Ln^{3+} ion in a given host lattice can also be estimated if *D(A)* is unknown, provided *E(Ln, A)* for another Ln^{3+} ion in the same host are known.

Based on the positions of *fd* levels in a wide variety of host lattices, it is clear that the Dorenbos model works well. There is however an uncertainty in the correlation between the positions of *fd* levels. The accuracy of estimates made for the positions of *fd* band using the Dorenbos relation shows that the position can be predicted on average within ~ 600 cm^{-1} but for some lanthanides the uncertainty is larger than 1000 cm^{-1} [1-3]. It is interesting to investigate the origin of the variation. A possible contribution may arise from the procedure of estimating the energies of *fd* states from band maxima. The band maxima do not represent the electronic origin of the lowest *fd* states. The position of the maximum for the vibronic *fd* bands is influenced by the electron-phonon coupling strength, concentration (through re-absorption and energy transfer), transitions to higher energy states (both in emission and excitation) and by competing absorptions which may distort excitation and emission bands. Zero phonon lines (ZPLs) however give the actual electronic energy of *fd* states, and by comparing the energies of zero-phonon lines for

different lanthanides in the same host, insight is obtained in the energy differences between the pure electronic states. Further, since ZPLs in the excitation spectra are located at lower energies than the band maxima, they can be observed even if the *fd* band is partially obscured by overlapping host lattice absorption bands, charge transfer bands or absorption bands related to defect states. The spectral position of the ZPL can also be accurately measured when the dopant Ln^{3+} ions occupy multiple crystallographic sites, since ZPLs are spectrally narrow, in contrast to *fd* bands. These characteristics make ZPLs potentially more reliable to estimate the lowest *fd* level position. A higher accuracy is desirable because, as mentioned above, the position of the *fd* excited state can be used to understand and predict luminescence properties of lanthanide doped materials [4-8]. For example, the knowledge of the location of the *4f* ground state and the *fd* excited state with respect to the valence and conduction bands of the host material is required to describe phenomena such as charge carrier trapping by the dopant Ln^{3+} ion and luminescence quenching, both of which are important in the development of materials suitable for detection of high energy photons (*i.e.* scintillators).

Unfortunately, zero-phonon lines cannot often be observed in the *f-d* luminescence spectra. When the electron-phonon coupling is strong the vibrational fine and ZPLs structure disappears. In case of weak electron-phonon coupling, zero-phonon lines may be observed, however it does require low-temperature studies and relatively low doping concentrations (typically below 1 mole%) to measure ZPLs. For this study four different host lattices were selected, namely CaF_2, $Y_3Al_5O_{12}$ (YAG), $LiYF_4$ and YPO_4. These hosts were chosen as model systems because they are known to show zero-phonon lines in the *f-d* luminescence spectra of lanthanides and they represent four different classes of materials, allowing the generality of the ZPL approach to be tested. $LiYF_4$ and YPO_4 are wide bandgap host lattices in which the Ln^{3+} ion occupies a single crystallographic site. YPO_4 is a more covalent host than $LiYF_4$. A wide bandgap is important, since it allows for the observation of high lying *fd* levels of the lanthanide ions, which would otherwise be situated in the conduction band. Especially for lanthanide ions for which the *fd* states are at high energies (Eu^{3+}, Ho^{3+}, Er^{3+} and Tm^{3+}) an overlap with host lattice absorption can prevent the observation of the *fd* bands. CaF_2 is a wide bandgap material in which charge compensation leads to different sites when Ln^{3+} ions are doped into the host lattice [10]. Therefore, it allows testing the ZPL approach in case multiple sites are involved. YAG is a well-known host lattice that is widely applied in the field of lanthanide luminescence. It is more covalent than the other hosts and shows a strong crystal-field splitting which shifts the lowest *fd* state to low energies. The four different types of host lattices form a good variety to test the general applicability of using ZPLs to more accurately determine $\Delta E^{Ln,Ce}$.

7.2. EXPERIMENTAL

In this study the position of the ZPLs of the lowest energy *fd* transition of trivalent lanthanide ions doped into CaF_2, $Y_3Al_5O_{12}$ (YAG), $LiYF_4$ and YPO_4 were used as input [viz. *E(Ln, A)]* in the Dorenbos relation (eq. 1) to calculate $\Delta E^{Ln,Ce}$ [1-4]. Data for $CaF_2:Ln^{3+}$, $LiYF_4:Ln^{3+}$, and $YPO_4:Ln^{3+}$ have been collected from the literature [11-13]. Data for YAG:Ln^{3+} were obtained in the present work. Luminescence measurements were carried out at low temperatures (<10 K) and for low Ln^{3+} concentrations in order to allow the fine structure of the *fd* band to be observed. YAG:Ln^{3+} samples were obtained in powder form through a modified Pechini method [14]. Y_2O_3, $Al(NO_3)_3$ and Ln_2O_3 were used as starting materials. Citric acid was used as the polymerizing agent. The samples were fired at 1600°C for 6 h in either air or N_2 as a slightly reducing atmosphere, necessary to obtain Ce^{3+}, Pr^{3+} and Tb^{3+} in their trivalent state. The luminescence spectra were measured using synchrotron radiation at SUPERLUMI station (DESY, Hamburg). A detailed description of the instrumental set-up can be found elsewhere [15]. The spectra were measured in three time windows (integrated, fast and slow) making it possible to distinguish between fast and slow emissions. The excitation spectra (65-335 nm) were corrected for the intensity distribution using the excitation spectrum of sodium salicylate. The emission spectra (180-700 nm) were not corrected for detector response. The sample temperature could be varied between ~8 K and 320 K in a cold finger helium cryostat. The luminescence excitation spectra in the 250-800 nm spectral range were measured using an Edinburgh Instruments FLS920 spectrofluorometer, equipped with a 450 W Xenon lamp. The spectra were corrected for the instrumental response.

7.3. RESULTS

7.3.1 $LiYF_4:Ln^{3+}$

$LiYF_4$ is a suitable host lattice for the investigation of the ZPL positions of *fd* bands of lanthanide ions, due to the fact that the bandgap is very wide (*viz.* 117 nm) and the *fd* bands show clear and strong zero-phonon lines. Experimental values for the positions of the ZPLs were obtained from REFS. 12 and 13. For the heavier lanthanides, transitions to both high spin (HS) and low spin (LS) *fd* states are observed. In the present analysis, only the spin-allowed transitions to the LS *fd* states are considered. The results obtained for the experimental and calculated positions of the band maxima and the ZPLs are presented in

Table 1, all relative to the position observed for Ce^{3+}. The deviation between the experimental and calculated values for the band maxima of Sm^{3+}, Eu^{3+} and Dy^{3+} is larger than the standard deviation reported in the literature for the Dorenbos relation for these ions [1-3]. Note that the standard deviations vary for different ions, based on the variation resulting from the analysis by Dorenbos. The values for $\Delta E^{Ln,Ce}$ and the standard deviations as reported by Dorenbos are included in Table 5. The difference between the experimental and calculated values obtained for the ZPL position is larger than the standard deviation only in the case of Eu^{3+}. This indicates that for Ln^{3+} ions in $LiYF_4$ the ZPL approach gives more accurate estimates for the position of the lowest *fd* level.

Table 1. Experimental (exp) and calculated (calc) positions of the band maxima and the zero-phonon lines (Band and ZPL, respectively) of *f-d* excitation bands of trivalent lanthanide ions in $LiYF_4$. The values are given in nm. The experimental data were obtained from REFS. [12,13]. Values marked with an asterisk (*) show a deviation with respect to the calculated positions that is larger than the standard deviation reported in the literature for the Dorenbos relation for the specific lanthanide ions [1-3].

Ln^{3+}	$Band_{exp}$	$Band_{calc}$	ZPL_{exp}	ZPL_{calc}
Ce	294.0	294.0	299.1	299.1
Pr	214.0	216.2	215.7	218.9
Nd	175.6	176.3	178.0	178.1
Sm	163.5*	165.3	167.8	166.9
Eu	144.0*	143.0	146.4*	144.2
Gd	-	125.3	-	126.2
Tb	212.0	211.8	213.4	214.4
Dy	165.0*	169.2	170.1	170.8
Ho	155.0	151.9	156.0	153.3
Er	155.0	156.2	155.5	157.6
Tm	156.0	157.9	158.6	159.4
Yb	-	138.9	-	140.0

7.3.2. $YPO_4:Ln^{3+}$

Just as $LiYF_4$, the YPO_4 host lattice has served as a model system for studies of lanthanide luminescence. The bandgap is large for an oxide (*viz.* 148 nm) and the *fd* luminescence spectra are characterized by well-resolved zero-phonon lines and vibronic lines. The Huang-Rhys coupling parameter is ~2 which allows for the observation strong zero-phonon lines, both in excitation and emission spectra. The results obtained for the experimental and calculated values of the positions of the band maxima and the ZPLs are obtained from REFS. 12 and 13 and collected in Table 2. The deviation between the experimental and calculated band maxima is larger than the standard deviation reported by Dorenbos [1-3] for Sm^{3+}, Eu^{3+}, Tb^{3+}, Dy^{3+} and Er^{3+}. In the case of the ZPL positions, only the values for Dy^{3+} and Er^{3+} show a difference larger than the standard deviation.

Table 2. Experimental (exp) and calculated (calc) positions of the band maxima and the zero-phonon lines (Band and ZPL, respectively) of *f-d* excitation bands of trivalent lanthanide ions in YPO_4. The values are given in nm. The experimental data were obtained from REFS. [12,13]. Values marked with an asterisk (*) show a deviation with respect to the calculated positions that is larger than the standard deviation reported in the literature for the Dorenbos relation for the specific lanthanide ions [1-3].

Ln^{3+}	$Band_{exp}$	$Band_{calc}$	ZPL_{exp}	ZPL_{calc}
Ce	321.9	321.9	325.7	325.7
Pr	227.0	230.9	229.7	232.9
Nd	186.0	186.0	187.8	187.3
Sm	171.0*	173.7	175.7	174.8
Eu	152.0*	149.3	-	150.1
Gd	-	130.1	-	130.7
Tb	217.0*	225.9	224.3	227.8
Dy	170.0*	178.0	176.7*	179.2
Ho	-	159.1	-	160.0
Er	160.0*	163.8	160.8*	164.7
Tm	162.0	165.7	164.0	166.7
Yb	145.0	144.8	145.2	145.6

7.3.3. CaF_2:Ln^{3+}

Table 3. Experimental (exp) and calculated (calc) positions of the band maxima and the zero-phonon lines (Band and ZPL, respectively) of *f-d* excitation bands of trivalent lanthanide ions in CaF_2. The values are given in nm. The experimental data were obtained from REFS. [12,13]. Values marked with an asterisk (*) show a deviation with respect to the calculated positions that is larger than the standard deviation reported in the literature for the Dorenbos relation for the specific lanthanide ions [1-3].

Ln^{3+}	$Band_{exp}$	$Band_{calc}$	ZPL_{exp}	ZPL_{calc}
Ce	306.0	306.0	309.9	309.9
Pr	218.0*	222.6	223.5	224.7
Nd	179.0	180.6	181.7	181.9
Sm	165.5*	169.0	170.9	170.2
Eu	-	145.8	-	146.7
Gd	-	127.4	-	128.1
Tb	215.0	218.0	216.2	219.9
Dy	168.0*	173.1	172.3*	174.3
Ho	156.0	155.1	157.5	156.1
Er	155.0*	159.5	156.1*	160.6
Tm	156.0*	161.3	159.0*	162.4
Yb	-	141.5	142.0	142.3

Multiple Ln^{3+} sites have been identified in CaF_2:Ln^{3+} [10]. The presence of multiple sites complicates the analysis of the *fd* spectra, both for determining $\Delta E^{Ln,Ce}$ from band maxima and from ZPL positions. The observation of multiple ZPLs leads to the possibility of confusing a ZPL from a higher energy site with one of the vibronic replicas of a lower energy site. Therefore, the present investigation is limited to the lowest energy ZPLs as reported in REFS. 12 and 13. The experimental and calculated values of the positions of the band maxima and of the ZPLs are presented in Table 3. The deviation between experimental and calculated values is larger than the reported standard deviations [1-3] for Pr^{3+}, Sm^{3+}, Dy^{3+}, Er^{3+} and Tm^{3+}, in the case of the band maxima, whereas for the ZPLs this is the case only for Dy^{3+}, Er^{3+} and Tm^{3+}. The relatively large deviations may be caused by the presence of differently charge compensated sites and the

lowest energy site may not always have the same configuration for the light and heavy lanthanides. This may explain the observation that larger deviations are found for the heavy lanthanides. As a result, the observed energy differences may not only reflect a variation due to the difference in lanthanide ion but also be caused by a change in local symmetry.

7.3.4. $Y_3Al_5O_{12}:Ln^{3+}$

The results obtained for YAG:Ln^{3+} are presented in Table 4. The positions of the zero-phonon lines have been obtained from low temperature spectra where for low concentrations a weak zero-phonon line can be observed. The electron-phonon coupling for *fd* transitions in YAG is larger than for the other three host lattices investigated in this chapter. The Huang-Rhys factor has been determined for YAG:Ce^{3+} to be ~ 6 which is the limit for the observation of zero-phonon lines. Indeed, it is often difficult to observe zero-phonon lines and this explains the smaller number of experimentally observed ZPLs in Table 4. Some of the positions reported, for example for Tb^{3+}, are not based on the observation of a well-separated ZPL, but are obtained from a sharp onset of the *f-d* excitation band which makes the accuracy of the position slightly lower (~ 0.5 nm). A second problem is the smaller bandgap of YAG which is located at 180 nm. For lanthanide ions having high energy *fd* bands (Eu, Ho, Er, Tm and Yb) the onset of the bandgap absorption interferes with the observation of the ZPL and also the band maxima given in Table 4 for these ions are affected by the host lattice absorption. Still, it is worthwhile to include this host lattice in the analysis. Because of the high covalency, stronger electron-phonon coupling and strong crystal-field splitting, the lowest *fd* state is shifted to low energies in this lattice. To prevent a bias of the conclusions on the difference in and accuracy of $\Delta E^{Ln,Ce}$ parameters determined from band maxima and ZPLs it is important to compare the results of the more ionic host lattices with weak electron phonon coupling ($LiYF_4$, CaF_2 and YPO_4) with those for YAG, which is representative for more covalent compounds.

Table 4. Experimental (exp) and calculated (calc) positions of the band maxima and the zero-phonon lines (Band and ZPL, respectively) of *f-d* excitation bands of lanthanides in YAG. The values are given in nm. Values marked with an asterisk (*) show a deviation with respect to the calculated positions that is larger than the standard deviation reported in the literature for the Dorenbos relation for the specific lanthanide ions [1-3].

Ln^{3+}	$Band_{exp}$	$Band_{calc}$	ZPL_{exp}	ZPL_{calc}
Ce	457.7	457.7	488.8	488.8
Pr	288.0	293.4	300.8	305.8
Nd	227.5	224.5	235.0	231.7
Sm	206.0	206.8	214.3	213.0
Eu	-	173.2	-	177.4
Gd	-	147.8	-	150.9
Tb	274.0*	285.3	280.7*	297.1
Dy	218.5*	213.0	-	219.5
Ho	188.0	186.4	-	191.4
Er	190.0	192.9	-	198.2
Tm	189.0*	195.5	-	201.0
Yb	-	167.1	-	171.1

7.4. DISCUSSION

The results in Tables 1-4 show that the variation in the energy differences between the *fd* state for Ce^{3+} and the other lanthanides determined from band maxima show a larger deviation from $\Delta E^{Ln,Ce}$ in the Dorenbos relation than the energy differences determined from zero-phonon lines. The calculated positions for the ZPLs are generally within the limits for the standard deviation given in REFS. [1-3]. For the observed band maxima there is larger number of cases where the positions fall outside uncertainty range for the calculated positions for the band maxima. Note that the standard deviation $\Delta E^{Ln,Ce}$ varies between different lanthanide ions. Especially for the lanthanides Ho, Er and Tm the error margin given in REFS. [1-3] is large, over 1000 cm^{-1}. It may not be surprising that the accuracy for ZPLs is higher since the positions of ZPLs can be determined with much higher accuracy. It is insightful to further analyze the presently determined values for $\Delta E^{Ln,Ce}$ from ZPLs and compare these with the values determined from band maxima.

In Table 5 we have collected the values for $\Delta E^{Ln,Ce}$ determined from ZPLs. For comparison, the values for $\Delta E^{Ln,Ce}$ from REFS. [1-3] are included, both with the standard deviation determined from the data. A first observation is that the standard deviation for the values from the ZPLs is much smaller, generally a factor of 2-3. This indicates that the standard deviation in the values for $\Delta E^{Ln,Ce}$ results for a large part from inaccuracies related to the determination of band maxima and not from actual variations of $\Delta E^{Ln,Ce}$. Apart from the fact that it is harder to determine the exact position for a broad band than for a sharp line, there are other factors. Factors that contribute to inaccuracies in the experimentally determined band maxima include saturation of absorption for higher concentrations (shifting the maxima to longer wavelengths), transitions to higher electronic *fd* states just above lowest energy *fd* states (shifting the band maxima to shorter wavelengths, depending on relative oscillators strengths of the lower and higher energy *fd* transitions) and a shift of the excitation band maximum due to overlapping absorption bands related to defects or impurities. The values for $\Delta E^{Ln,Ce}$ determined from ZPLs reflect the true energy differences between the electronic *fd* states.

Table 5. Values of the $\Delta E^{Ln,Ce}$ parameter obtained by using either the band maxima (Band) [1-3] or the position of the zero-phonon lines (ZPL) in the Dorenbos relation (this chapter). Values are given in cm^{-1}. N gives the number of compounds used to determine the $\Delta E^{Ln,Ce}$ value. The difference between the $\Delta E^{Ln,Ce}$ values obtained by the two methods is given in the last column (Δ(ZPL-Band)).

Ln^{3+}	ZPL $\Delta E^{Ln,Ce}$	N_{ZPL}	Band $\Delta E^{Ln,Ce}$	N_{Band}	Δ(ZPL-Band)
Pr	12754 ± 196	4	12240 ± 750	65	514
Nd	22540 ± 312	4	22700 ± 650	18	-160
Sm	26210 ± 32	4	26500 ± 460	2	-290
Eu	34874	1	35900 ± 380	4	-1026
Gd	-	-	45800	1	-
Tb	14115 ± 742	4	13200 ± 920	30	915
Dy	25672 ± 281	3	25100 ± 610	4	572
Ho	30947 ± 392	2	31800 ± 1400	5	-853
Er	31385 ± 467	3	30000 ± 1300	8	1385
Tm	30172 ± 511	3	29300 ± 1100	9	873
Yb	38160 ± 9	2	38000 ± 570	3	160

Comparison of the values for $\Delta E^{Ln,Ce}$ from the analysis in this chapter with those determined in REFS [1-3] shows that for the light lanthanides $\Delta E^{Ln,Ce}$ is generally smaller, except for Pr, and for the heavy lanthanides the values are larger, except for Ho^{3+}. The value for Eu^{3+} shows a large deviation (over 1000 cm^{-1} to lower energy) which may be related to the difficulty to determine the maximum of the *f-d* excitation band maximum on top of the charge transfer band which is always at lower energies for Eu^{3+}. Probably the presently determined value from well-defined zero-phonon lines is more accurate. For Ho^{3+} the lower value for $\Delta E^{Ln,Ce}$ obtained from ZPLs can be understood by considering the electronic structure. The excitation spectra for Ho^{3+} in REF. [13] show strong transitions to several electronic states spread over up to 3000 cm^{-1} higher energies. As a result, the maximum of the broad excitation band is shifted to higher energies. The value for $\Delta E^{Ln,Ce}$ determined from ZPLs gives a better estimate for the position of the lowest *fd* state relative to that for Ce^{3+}. The problem of transitions to higher energy *fd* states is a general cause for a shift of the *fd* band maximum as discussed above.

The present analysis includes only four host lattices. The results show that the variation in $\Delta E^{Ln,Ce}$ values is much smaller than for the values determined from band maxima in a considerably larger number of host lattices. The smaller standard deviations indicate that the basic idea behind the Dorenbos model (constant energy difference between the lowest *fd* states of different lanthanide ions in the same host lattice) is more correct than suggested by the deviations observed for band maxima. The variations in experimentally observed energies are for a large part not related to actual differences between the energies of the lowest *fd* states but result from problems related the procedure used (relying on band maxima). The presently observed deviations (up to ~ 500 cm^{-1}) for ZPLs correspond to wavelength shifts of 1 nm or less for the ZPLs and this suggests that the positions of ZPLs can be predicted with a 1 nm accuracy. In addition to smaller standard deviations, we also find different average values for $\Delta E^{Ln,Ce}$ which can be ~ 1000 cm^{-1} higher or lower than those in REFS. [1-3]. In studies in which the exact location of the lowest energy *fd* state with respect to the conduction band is important, the newly obtained values may give more accurate results. To confirm if the values for $\Delta E^{Ln,Ce}$ determined from ZPLs are more accurate, further studies are required, including an extension to a larger number of host lattices and investigations into which set of values for $\Delta E^{Ln,Ce}$ can better explain phenomena related to the position of the lowest energy *fd* state relative to the conduction band (e.g. photoionization quenching and charge trapping).

7.5. CONCLUSIONS

The Dorenbos relation allows for an accurate estimate of the position of the lowest *fd* state of trivalent lanthanide ions once the energy of one ion is known. The model has been derived using band maxima for *fd* band. In this chapter we have shown that the Dorenbos relation also applies to *fd* zero-phonon lines (ZPLs). The agreement between calculated and experimentally observed positions is better when using the ZPLs instead of the band maxima. Advantages of the ZPL approach are that the position ZPLs can be determined more accurately and, unlike band maxima, it is not influenced by effects like saturation of absorption, competing absorption bands and transitions to nearby higher energy electronic *fd* states. Based on the analysis of the positions of the ZPLs for the lowest energy *fd* states refined and possibly more accurate values of the $\Delta E^{Ln,Ce}$ parameters have been determined with standard deviations that are 2-3 times smaller than for the values derived from band maxima.

REFERENCES

[1] P. Dorenbos, *J. Lumin.* **87-89** (2000) 970-972
[2] P. Dorenbos, *J. Lumin.* **91** (2000) 91-106
[3] P. Dorenbos, *J. Lumin.* **91** (2000) 155-176
[4] P. Dorenbos, *J. Lumin.* **108** (2004) 301-305
[5] L. Pidol, B. Viana, A. Galtayries, P. Dorenbos, *Phys. Rev. B* **72** (2005) 125110
[6] P. Dorenbos, *J. Lumin.* **122-123** (2007) 315-317
[7] P. Dorenbos, A.J.J. Bos, *Radiat. Meas.* **43** (2008) 139-145
[8] A.J.J. Bos, P. Dorenbos, A. Bessière, B. Viana, *Radiat. Meas.* **43** (2008) 222-226
[9] A. F. Campos, A. Meijerink, C. de Mello Donegá, O.L. Malta, *J. Phys. Chem. Solids* **61** (2000) 1489
[10] K.D. Oskam, A.J. Houtepen, A. Meijerink, *J. Lumin.* **97** (2002) 107-114
[11] M.F. Reid, L. van Pieterson, R.T. Wegh, A. Meijerink, *Phys. Rev. B* **62** (2000) 14744
[12] L. van Pieterson, M.F. Reid, R.T. Wegh, S. Soverna, A. Meijerink, *Phys. Rev. B* **65** (2002) 045113
[13] L. van Pieterson, M.F. Reid, G.W. Burdick, A. Meijerink, *Phys. Rev. B* **65** (2002) 045114
[14] M.P. Pechini, *US Patent no. 3.330.697* July 1 (1967)
[15] G. Zimmerer, *Nucl. Instrum. Methods A* **308** (1991) 178-186

Samenvatting in het Nederlands

Het proefschrift dat u in uw handen heeft geeft de lezer een kijkje in de fascinerende wereld van luminescentie, scintillatie en scintillatormaterialen die gebruikt worden voor medische beeldvorming. Een aantal beeldvormende technieken wordt uitgelegd en er wordt ingegaan op de cruciale eigenschappen die de materialen voor die toepassing moeten bezitten, waaronder efficiënte radioluminescentie. Luminescentie is het verschijnsel van het uitzenden van licht, mogelijk van verschillende golflengten en daarmee verschillende kleuren, wanneer een materiaal, een fosfor genoemd, wordt gestimuleerd. De stimulatie kan op diverse manieren plaatsvinden. Het licht kan worden opgewekt door UV-straling (fotoluminescentie) maar bijvoorbeeld ook mechanisch (triboluminescentie), snelle elektronen (kathodeluminescentie), verwarming (thermoluminescentie), chemische reactie (chemoluminescentie) of ioniserende straling (radioluminescentie of scintillatie).

In het geval van medische beeldvorming waar scintillatoren worden gebruikt, is de ioniserende straling röntgenstraling of γ-straling. Deze vorm van straling heeft een hoog doordringend vermogen dat verschillend is voor weefsel met een verschillende dichtheid. Botten absorberen röntgenstraling sterker dan spieren of organen door de hogere dichtheid als gevolg van de aanwezigheid van zwaardere elementen zoals calcium (Ca) en fosfor (P). Met behulp van medische beeldvormingtechnieken op basis van röntgen- en γ-straling is het mogelijk voor doktoren om in het lichaam van de patiënt te kijken zonder operatie. Er is een grote verscheidenheid aan medische beeldvormingtechnieken op basis van ioniserende straling. Bekende voorbeelden zijn Röntgenfotografie, Computationele Tomografie (CT), Enkel Foton Emissie Computationele Tomografie (SPECT) en Positron Emissie Tomografie (PET). Bij al deze technieken vormen scintillatoren het hart van de machine waarbij er verschillende eisen worden gesteld aan de scintillator. Dit proefschrift richt zich op scintillatormaterialen voor PET-scanners.

De geschiedenis van scintillatoren begint in 1895. Wilhelm Conrad Röntgen ontdekt in dat jaar een nieuw soort straling die hij X-stralen noemt. De nieuwe straling heeft de bijzondere eigenschap dat ze doordringt in objecten en, afhankelijk van de dichtheid en dikte van het object, een barium platinacyanide plaat aan de andere kant ervan kan doen oplichten. Röntgen realiseert zich al snel het belang van deze ontdekking en

publiceert een serie artikelen over deze straling, waaronder het artikel met de beroemde foto van de hand van mevrouw Röntgen waarin de botten en de trouwring zichtbaar zijn. Het is de ontdekker van de straling ook onmiddellijk duidelijk dat de straling niet goed geabsorbeerd wordt door fotografische film waarop het beeld wordt vastgelegd. Er is een materiaal nodig dat in staat is de ioniserende straling om te zetten in straling met een golflengte die beter geabsorbeerd wordt door de film. Een uitgebreide zoektocht binnen de wetenschappelijke gemeenschap resulteert al snel in de ontwikkeling van een röntgenversterkingsscherm. Op het scherm is een dunne laag van een scintillatormateriaal aangebracht waarin de ioniserende straling wordt omgezet in zichtbaar licht. Dit licht valt op de fotografische film die zeer gevoelig is voor zichtbaar licht en direct achter het scherm is geplaatst waardoor er met een veel lagere dosis van röntgenstraling een foto gemaakt kan worden. In de tijd van Röntgen waren de schadelijke effecten van de straling nog niet bekend en was het belangrijkste voordeel een kortere belichtingstijd en daardoor scherpere foto's. Bij de huidige ontwikkeling van scintillatoren is het verlagen van de stralingsdosis om de belasting voor de patiënt te verminderen een belangrijk aspect in de ontwikkeling van nieuwe materialen. De meest bekende scintillator werd al een jaar na de ontdekking van röntgenstraling ontdekt door Pupin. Dit was $CaWO_4$. Dit materiaal was zo succesvol dat het meer dan 80 jaar is gebruikt voor het maken van röntgenfoto's en nog steeds wordt het, vanwege de lage prijs, toegepast. In de afgelopen decennia zijn er veel nieuwe scintillatoren ontwikkeld maar de noodzaak voor betere scintillatoren met specifieke eigenschappen blijft onderzoek naar nieuwe materialen stimuleren, zoals blijkt uit dit proefschrift.

Het scintillatieproces omvat drie stappen: absorptie van de opvallende straling, energie-overdracht van het grondrooster naar het luminescerende ion en tenslotte het uitzenden van licht door dit ion. Wil een scintillatormateriaal effectief zijn, dan moeten alle drie stappen met hoge efficiëntie plaatsvinden. Als dat niet het geval is, is het materiaal niet geschikt voor toepassing. Het onderzoek in dit proefschrift is gericht op betere scintillatoren voor PET-scanners. Een belangrijke voorwaarde bij deze toepassing is dat de responstijd van de scintillator extreem kort is, nanoseconden. Een beter fundamenteel begrip van het scintillatieproces is daarbij belangrijk en helpt bij de ontwikkeling van betere materialen. Lanthanide-ionen zijn in de meeste scintillatoren verantwoordelijk voor het uitzenden van licht en de geschiedenis en luminescentie-eigenschappen van lanthaniden worden daarom beschreven. Lanthanide-ionen kunnen zowel luminescentie vertonen als gevolg van overgangen binnen de *4f* configuratie als van overgangen tussen de *4f* en *5d* schil. Deze laatste vorm van luminescentie, *d-f* emissie, heeft een korte levensduur en het is dit type emissie dat zeer geschikt is voor toepassing in PET-scintillatoren. In dit proefschrift wordt *d-f* luminescentie voor een drietal lanthaniden, Ce^{3+}, Pr^{3+} en Nd^{3+}, bestudeerd. Bij dit onderzoek is veelvuldig gebruik gemaakt van de faciliteiten van HASYLAB van het DESY synchrotron in Hamburg. De SUPERLUMI bundellijn bij dit

synchrotron is uitermate geschikt voor experimenten in het (vacuum) ultraviolette spectrale gebied en heeft ook de gewenste hoge tijdsresolutie om snelle responstijden te kunnen meten.

In hoofdstuk 2 wordt een zeer eenvoudig materiaal gebruikt als grondrooster voor het verkrijgen van snelle luminescentie: keukenzout. De *f-f* en *d-f* luminescentie van Ce^{3+}, Pr^{3+} en Nd^{3+} in NaCl worden beschreven. De materialen zijn gemaakt door NaCl met de gewenste lanthanide dotering te smelten en zeer snel af te koelen. Dit is nodig om de lanthanide-ionen in te bouwen. Door het verschil in lading (3+ vs. 1+) bouwt het lanthanide-ion niet in bij langzaam afkoelen. Er wordt aangetoond dat er zowel *f-f* als *d-f* emissie wordt waargenomen voor de lanthanide-ionen in NaCl. De emissie voor Ce^{3+} ligt bij 360 nm en heeft een vervaltijd van 21 ns. Voor Pr^{3+} is er geen *d-f* emissie, waarschijnlijk door energie-overdracht naar defecten. Er wordt wel *f-f* emissie waargenomen. Voor NaCl gedoteerd met Nd^{3+} wordt geen karakteristieke Nd-emissie gemeten. De waarnemingen geven aan dat simpele alkali-halogeniden gedoteerd kunnen worden met luminescerende lanthanide-ionen en interessant zijn als grondrooster voor nieuwe scintillatoren.

Eerder onderzoek naar nieuwe scintillatoren heeft laten zien dat chlorides gedoteerd met Ce^{3+} een veelbelovende klasse van scintillatormaterialen zijn waarin een korte levensduur en een hoge efficiëntie gecombineerd worden. Nog kortere responstijden kunnen bereikt worden als Ce^{3+} vervangen wordt door Pr^{3+} of Nd^{3+} omdat de levensduur van de *d-f* emissie voor deze ionen nog korter is. In hoofdstuk 3 worden de luminescentie-eigenschappen van Ce^{3+}, Pr^{3+} en Nd^{3+} in RbCl beschreven en worden de mogelijkheden van deze eenvoudige chemische verbinding voor toepassing als scintillatormateriaal besproken. Onder UV-excitatie geeft Ce^{3+} *d-f* emissie tussen 325 en 425 nm. De emissie is afkomstig van verschillende Ce^{3+} sites die ontstaan doordat er ladingscompensatie nodig is voor het driewaardige Ce-ion op een Rb^{+} site. De levensduur van de *d-f* emissie varieert als functie van de emissiegolflengte en is ~ 40 ns voor de langgolvige emissie. Voor RbCl:Pr^{3+} worden er drie *d-f* emissiebanden waargenomen tussen 250 en 350 nm. De emissie wordt toegekend aan *d-f* emissie vanuit de laagstenergetische *fd* toestand naar verschillende ^3H_J (J=4-6) toestanden van de $4f^2$ configuratie van Pr^{3+}. De levensduur van de emissie is ~ 17 ns. Voor het Nd^{3+}-gedoteerde RbCl wordt een zwakke emissieband rond 220 nm waargenomen bij lage temperatuur (8 K). De levensduur is erg kort, ~ 4 ns, en is sneller dan de verwachte stralende levensduur. Dit geeft aan dat er al bij 8 K doving plaatsvindt van de *d-f* emissie, ofwel door niet-stralend verval naar lager gelegen toestanden binnen de $4f^3$ configuratie van Nd^{3+} ofwel door foto-ionisatie. Onder VUV-excitatie bij golflengten korter dan 175 nm, de bandgap van RbCl, is *d-f* emissie zwak of afwezig en de emissiespectra worden gedomineerd door defect-gerelateerde emissies. Dit duidt erop dat de energie-overdracht van het grondrooster naar de *fd* toestanden niet efficiënt is en dit beperkt de mogelijkheden voor toepassing als scintillatormateriaal.

De fotoluminescentie en radioluminescentie van Ce^{3+}, Pr^{3+} en Nd^{3+} in $SrCl_2$ en $BaCl_2$ worden beschreven in hoofdstuk 4. In het Ce^{3+} gedoteerde materiaal wordt de karakteristieke snelle *d-f* emissie van waargenomen (358 en 382 nm in $SrCl_2$ en 350 en 375 nm in $BaCl_2$) zowel onder excitatie met (V)UV straling bij het synchrotron als onder ioniserende bestraling. Na beëindiging van de hoogenergetische bestraling licht het sample na. Voor Pr^{3+} in deze grondroosters wordt eveneens *d-f* emissie waargenomen, bij 250, 263, 300 en 328 nm in $SrCl_2$ en bij 260, 288 en 315 nm in $BaCl_2$. De levensduur van de emissie is kort: 13 ns voor Pr^{3+} in $SrCl_2$ en 10 ns voor Pr^{3+} in $BaCl_2$. De *d-f* emissie wordt alleen waargenomen voor directe excitatie in de *fd* toestanden. Voor excitatie van het grondrooster met VUV-straling of röntgenstraling wordt geen *d-f* emissie gemeten. De afwezigheid van *d-f* emissie wordt verklaard door de lage energie van de grondroosteremissie. Deze is te laag voor energie-overdracht naar de hoogenergetische *fd* toestanden van Pr^{3+} in $SrCl_2$ en $BaCl_2$.

$Lu_3Al_5O_{12}$ (LuAG) gedoteerd met Ce^{3+} is een veelbelovend scintillatormateriaal. Het heeft een hoge dichtheid en een snelle responstijd. De efficiëntie onder röntgen- of γ-bestraling is echter aanzienlijk lager dan de theoretisch berekende maximale efficiëntie. Een mogelijke verklaring voor de lagere efficiëntie is dat er naast energie-overdracht van het grondrooster naar Ce^{3+} ook energie wordt overgedragen naar roosterdefecten waar de energie vervolgens stralingsloos verloren gaat. Verhogen van de Ce^{3+} concentratie is een mogelijkheid om de efficiëntie te verbeteren, maar voor hogere Ce-concentraties treedt er concentratiedoving op. Een alternatief is co-doteren met een ander lanthanide-ion dat in staat is de excitatie-energie van het grondrooster in te vangen en vervolgens efficiënt over te dragen naar Ce^{3+}. In hoofdstuk 5 wordt daartoe LuAG:Ce, Tb^{3+} onderzocht. Eerst worden hoge resolutiespectra van LuAG:Tb en LuAG:Ce gemeten bij lage temperaturen om inzicht te krijgen in de exacte ligging van de energieniveaus van Ce^{3+} en Tb^{3+} in LuAG. Voor Ce^{3+} worden zero-fonon lijnen en vibratiestructuur waargenomen voor de twee laagstenergetische *fd* banden. Uit de metingen worden de Stokes shift (2350 cm^{-1}) en de Huang-Rhys koppelingsparameter (S=9) bepaald. De spectra voor Tb^{3+} laten *f-d* overgangen naar hoge spin (HS) en lage spin (LS) *fd* toestanden zien, opnieuw met vibronische fijnstructuur. De HS-LS splitsing is 5400 cm^{-1} en is lager dan de waarde die gemiddeld wordt waargenomen voor deze splitsing. De verklaring hiervoor is een kleinere *5d-4f* exchange koppelingsparameter J als gevolg van de hoge covalentie. Wanneer bij de co-dotering met Tb^{3+} het kleinere Lu^{3+} ion vervangen wordt door het grotere Tb^{3+}, neemt de kristalveldsplitsing voor de 5*d* toestand van Ce^{3+} toe en schuift de laagste *fd* toestand van Ce^{3+} naar een energie net onder het $^5D_4$ nivo van Tb^{3+} waardoor energie-overdracht van Tb^{3+} naar Ce^{3+} zelfs bij lage temperaturen efficiënt is. Levensduurmetingen van de luminescentie van zowel Ce^{3+} als Tb^{3+} bevestigen de efficiëntie van energie-overdracht en geven een kwalitatief begrip van de verschillende energie-overdrachtsprocessen. Co-doteren met Tb^{3+} resulteert echter niet in een verhoging van de lichtopbrengst onder

röntgenexcitatie. Een verklaring wordt gegeven op basis van de rol van invangen van elektronen door defecten.

In hoofdstuk 6 wordt het verband tussen emissiegolflengte en stralende levensduur onderzocht voor *d-f* emssie van Pr^{3+}. De stralende levensduur van emissie wordt beschreven door Fermi's Golden Rule die aangeeft hoe de emissie sneller wordt voor een kortere emissiegolflengte en hogere brekingsindex. Een beter begrip van de stralende levensduur is van belang bij het ontwerpen van nieuwe materialen met specifieke toepassingen, zoals scintillatoren, waarvoor een korte levensduur van de emissie vereist is. Door de toenemende belangstelling voor scintillatoren op basis van de *d-f* emissie van Pr^{3+} is onderzoek naar de stralende levensduur van Pr^{3+} niet alleen fundamenteel interessant, maar ook belangrijk bij de ontwikkeling van nieuwe scintillatoren. Systematisch onderzoek naar de levensduur van de *d-f* emissie van Pr^{3+} is niet eerder verricht, in tegenstelling tot Eu^{2+} en Ce^{3+}. Voor de nauwkeurige bepaling van de levensduur, zijn er metingen verricht voor de *d-f* emissie van Pr^{3+} in een groot aantal grondroosters bij lage temperatuur en voor lage Pr-concentraties. De metingen laten zien dat er, zoals verwacht, een duidelijke afname is van de levensduur als de emissie bij kortere golflengten ligt. De experimentele data zijn gefit aan het door Fermi's Golden Rule voorspelde verband met verschillende modellen voor de correctie voor locale veld effecten en voor een kwadratische en derdemacht afhankelijkheid van de emissiegolflengte. De overeenstemming met de theorie is het best voor een derdemachtafhankelijkheid. De spreiding van de data rond de lijn van het theoretische verband is echter groot. Dit wordt deels verklaard doordat precieze waarden voor brekingsindices in het UV vaak niet bekend zijn terwijl ook niet duidelijk is welk model gebruikt moet worden om te corrigeren voor locale veld effecten. Daarnaast is er een variatie van het overgangsdipoolmoment voor de *d-f* overgangen voor Pr^{3+} in verschillende roosters die een verschil in levensduur geeft. Op basis van de resultaten kan de kortste levensduur die mogelijk is voor *d-f* emissie van Pr^{3+} geschat worden op ~ 6 ns voor emissie bij 220 nm en een brekingsindex van 1.8. Deze waarde geeft de limiet voor een stralende levensduur voor een scintillator gebaseerd op *d-f* emissie van Pr^{3+}.

Het laatste hoofdstuk is gewijd aan de zgn. Dorenbosrelatie die de positie van *fd* toestanden van lanthaniden in eenzelfde grondrooster aan elkaar relateert. Als de positie van de *fd* band voor een lanthanide-ion in een grondrooster bekend is, kan met de relatie de positie van de *fd* band voor alle andere lanthaniden voorspeld worden. In hoofdstuk 7 wordt de nauwkeurigheid van dit model getest door de posities van zero-fononlijnen van *fd* overgangen te bepalen en de gemeten energieverschillen tussen de zero-fononlijnen voor verschillende lanthaniden in hetzelfde grondrooster te vergelijken met de waarden uit het Dorenbosmodel. Het voordeel van het gebruik van zero-fononlijnen in plaats van bandmaxima is dat een zero-fononlijn de zuivere elektronische energie weergeeft en de positie ervan wordt niet beïnvloed door elektron-fonon koppeling. Daarnaast kan de positie van het gemeten bandmaximum beïnvloed worden door de concentratie (verschuiving naar

langere golflengte voor hogere concentraties) en door overgangen naar dichtbijgelegen hogere elektronische aangeslagen toestanden. Er is echter maar een beperkt aantal grondroosters waarin zero-fononlijnen voor *f-d* overgangen worden waargenomen. In dit hoofdstuk zijn de resultaten voor lanthanide-ionen in vier grondroosters gebruikt: $LiYF_4$, CaF_2, YPO_4 en $Y_3Al_5O_{12}$. De positie van zero-fononlijnen voor *fd* overgangen worden vergeleken met die voor de bandmaxima en laten zien dat het Dorenbosmodel ook voor zero-fononlijnen voldoet. De afwijking is kleiner dan voor de bandmaxima en dit laat zien dat gebruik van zero-fononlijnen een nauwkeuriger schatting geeft van de energieverschillen tussen *fd* niveaus voor lanthaniden in eenzelfde grondrooster.

Streszczenie po polsku

Niniejszy doktorat wprowadza czytelnika w ekscytujący świat luminescencji, scyntylacji i materiałów scyntylacyjnych, wykorzystywanych w obrazowaniu medycznym. Różne metody obrazowania są przedstawione z uwzględnieniem istotnych własności materiałów w nich wykorzystywanych. Proces luminescencji jest emisją światła o różnych długościach fali, stąd też o różnych barwach, który następuje w wyniku stymulacji materiału zwanego luminoforem. Stymulacja może mieć różną naturę. Gdy zachodzi ona poprzez wystawienie materiału na działanie światła, mówimy o fotoluminescencji. W przypadu mechanicznej stymulacji, proces emisji nazywamy triboluminescencją. Ciekawy przykład triboluminescencji zachodzi w cukrze. Gdy cukier jest mielony bądź potrząsany, zachodzi emisja światła o niebieskiej barwie, na skutek uwolnienia energii zmagazynowanej w jego molekulach. Emisja światła w wyniku napromieniowania energetycznymi cząstkami bądź promieniowaniem jonizujacym nazywana jest radioluminescencją lub scyntylacją.

W przypadku obrazowania medycznego, gdzie mamy do czynienia z materiałami scyntylującymi, promieniowanie jonizujące to promieniowanie rentgenowskie, bądz pronieniowanie gamma. Oba rodzaje promieniowania mają negatywny wpływ na żywe organizmy, lecz są niezbędne w przypadku obrazowania kości bądź tkanek wewnętrznych, z uwagi na fakt iż penetrują one żywą tkankę, a ich absorpcja przez różne tkanki jest różna. Przykładowo kości absorbuja promieniowanie rentgenowskie lepiej niż mięśnie lub organy, gdyż zawierają w swej strukturze cięższe pierwiastki chemiczne, takie jak wapń (Ca) czy fosfor (P). Metody obrazowania medycznego wykorzystują to zjawisko, by umożliwić lekarzom wgląd w głąb ciala pacjenta bez konieczności stosowania metod inwazyjnych. Spośród systemow obrazowania medycznego wykorzystujących promieniowanie jonizujące można wyróżnić rentgenografię planarną, tomografię komputerową (CT), emisyjną tomografię komputerową pojedynczych fotonów (SPECT), mammografię oraz pozytonową emisyjną tomografię komputerową (PET). W przypadku każdej w wymienionych technik obrazowania, sercem aparatury są scyntylatory. Różne wymagania stawiane są scyntylatorom w zależności o tego, w której metodzie będą wykorzystywane. Niniejsza

praca doktorska oparta jest na badaniach nad scyntylatorami do zastosowania w skanerach PET.

Historia scyntylacji i scyntylatorów rozpoczęła się w roku 1895, kiedy to Wilhlem Conrad Röntgen odkrył nowy rodzaj promieniowania, który nazwał promieniowaniem X. Nowe promieniowanie miało niezwykłą własność przenikania przez obiekty o różnej gęstości i kreowania luminescencji platynocyjanianu baru, znajdującego się po ich przeciwnej stronie. Röntgen szybko doszedł do wniosku, iż nowe odkrycie jest znaczące i opublikował serię artykułów, w których opisal nowo odkryte promieniowanie. W pracach tych prezentował on słynne zdjęcie ręki kobiety z pierścieniem na jednych z palców. Było to zdjęcie pierwszego żywego obiektu jego badań, mianowicie pani Röntgen. Odkrywca promieniowania X rychło zorientował się, iż nowe promieniowanie nie jest efektywnie absorbowane przez film fotograficzny, na którym wywoływane były obrazy kości. Koniecznym było wykorzystanie materiałów, które konwertowałyby promieniowanie rentgenowskie na światło widzialne o długości fali, która byłaby efektywnie absorbowana przez kliszę fotograficzną. W środowisku naukowym rozpoczęły się intensywne badania nad nowymi materiałami, które spełniałyby te wymagania. Rozpoczęto prace nad tak zwanymi ekranami intensyfikującymi. Ekrany te zawierały scyntylator, który konwertował promieniowanie X do promieniowania o długości fali mogącej być zaabsorbowaną przez kliszę fotograficzną. Najlepiej znanym materiałem, odkrytym zaledwie rok po odkryciu Röntgena w 1896, był $CaWO_4$. Jego wynalazcą był Pupin. Materiał ten odniósł tak wielki sukces, że był używany przez ponad 80 lat. W niektórych miejscach na świecie używany jest do dziś. Nowe scyntylatory posiadające ulepszone własności były odkrywane i badane przez kolejne dekady. Także starsze materiały były badane, a ich wlasności ulepszane, sprawiając iż stawały się one glównymi kandydatami do zastosowań w przemyśle. Poszukiwania nowych, ulepszonych scyntylatorów są kontynuowane do dziś dnia, dzięki czemu szanse na powstanie miała ta praca doktorska.

Proces scyntylacji składa się z trzech etapów: absorpcja wysoko energetycznego promieniowania jonizującego przez matrycę, transfer energii od matrycy do jonu aktywnego i emisja światła na jonie aktywnym. Aby scyntylator emitował światło z dużą wydajnością, wydajności cząstkowe każdego z etapów scyntylacji także muszą być wysokie. Jeśli materiał posiada słabe własności na którymkolwiek z etapów, nie jest on odpowiedni do zastosowań w scyntylacji.

Motywacją do powstania niniejszej pracy była potrzeba odkrycia i udoskonalenia nowych materialów dla zastosowań w pozytonowej emisyjnej tomografii komputerowej. W zastosowanium tym konieczne jest, aby materiał wykazywał jak najkrótszą emisję światła (rzędu kilku nanosekund). Także lepsze poznanie mechanizmów scyntylacji jest konieczne, aby umożliwić rozwój i ulepszanie scyntylatorów, jak i z pukntu widzenia poszerzania wiedzy fundamentalnej.

Jako że lantanowce są z reguły wykorzystywane jako jony aktywne w scyntylatorach, ich własności i historia ich odkrycia są przedstawione, aby zapoznać czytelnika z ich własnościami oraz korzyściami płynącymi z ich zastosowania. Różne rodzaje emisji mogące zachodzić w przypadku jonów lantanowców są przedstawione z uwzględnieniem ich wykorzystania w technikach wymagających szybkiego czasu odpowiedzi systemu.

Jedyny w swoim rodzaju ośrodek badawczy synchrotronu w HASYLABie, DESY w Hamburgu w Niemczech został szczegółowo opisany. Ośrodek dał możliwość zarejestrowania większości z przedstawionych w niniejszej pracy doktorskiej widm luminescencji, wzbudzenia luminescencji i kinetyki emisji.

Powyższe tematy cząstkowe zostały zebrane we wstępie do nieniejszego doktoratu, będącym rozdziałem pierwszym.

Rozdział drugi pokazuje, jak bardzo prosty związek chemiczny może być wykorzystany w celu uzyskania bardzo szybkiej emisji. W rozdziale tym luminescencja *f-f* oraz *d-f* jonów ceru (Ce^{3+}), prazeodymu (Pr^{3+}) i neodymu (Nd^{3+}) w chlorku sodu (NaCl), czyli zwykłej soli kuchennej, jest opisana. Próbki zostały przygotowane poprzez gwałtowne schłodzenie stopionych soli NaCl oraz lantanowców. Postępowanie takie było konieczne z uwagi na fakt iż w materiale tym występuje znaczna różnica ładunku i promieni jonowych pomiędzy jonami Na^{+} oraz lantanowców (Ln^{3+}). Zostało wykazane, że zarówno emisja *f-f*, jak i *d-f* z jonów lantanowców została zaobserwowana w chlorku sodu. Widma emisyjne i wzbudzenia emisji zostały przeanalizowane. Emisja NaCl aktywowanego Ce^{3+} ma swoje maksimum przy 360 nm i czas życia tejże emisji wynosi okolo 21 ns. W przypadku materiału aktywowanego Pr^{3+} nie zaobserwowano emisji *d-f* z uwagi na transfer energii do stanów energetycznych defektów znajdujących się w sieci krystalicznej materiału. Aktywowanie NaCl jonami Nd^{3+} nie spowodowalo pojawienia sie emisjii charakterystycznej dla neodymu w obszarze spektralnym, w którym prowadzono badania. Wyniki badań przeprowadzonych na chlorku sodu domieszkowanego jonami lantanowców są interesujace nie tylko z punktu widzenia wiedzy fundamentalnej, ale pokazują także, iż możliwe jest uzyskanie nowych scyntylatorów w oparciu o bardzo proste układy halogenkowe, aktywowane jonami trójdodatnich lantanowców.

W poszukiwaniach nowych materialów scyntylacyjnych jony Ce^{3+} wbudowane w sieć krystaliczną układów chlorkowych są bardzo obiecujące, gdyż układy takie łączą w sobie zarówno wysoką wydajność scyntylacji, jak i krótkie czasy życia luminescencji. Jeszcze krótsze czasy życia emisji można uzyskać zastępując jony Ce^{3+} jonami Pr^{3+} bądz Nd^{3+}, jako iż czas życia emisji *d-f* w przypadku tych jonów jest znacznie krótszy. Rozdział trzeci opisuje własności luminescencyjne jonów Ce^{3+}, Pr^{3+} oraz Nd^{3+} w sieci krystalicznej RbCl. Możliwości wykorzystania tego prostego z chemicznego punktu widzenia materiału jako scyntylatora są przedyskutowane. Po wzbudzeniu Ce^{3+} promieniowaniem UV,

obserwuje się emisję *d-f*, zlokalizowaną pomiędzy 325 nm i 425 nm. Emisja pochodzi z jonów Ce^{3+} o różnym lokalnym otoczeniu, wynikajacym z konieczności zbalansowania ładunku. Czas życia emisji jest różny dla różnych jonów ceru i wynosi ~ 40 ns dla ceru emitującego przy długich falach. W przypadku RbCl:Pr^{3+} trzy pasma emisyjne należące do przejść *d-f* zostały zaobserwowane pomiędzy 250 nm a 350 nm, które to pasma zostały przypisane do przejść między najniższym energetycznie stanem *fd* a różnymi poziomami energetycznymi ^3H_J (J=4-6) konfiguracji $4f^2$ Pr^{3+}. Czas życia luminescencji wynosi ~ 17 ns. W przypadku próbek aktywowanych Nd^{3+} emisja o bardzo niskiej intensywności położona przy okolo 220 nm była zaobserwowana jedynie w temperaturze 8 K i została przypisana do przejscia *d-f*. Bardzo krótki czas życia (4 ns) tej emisji jest krótszy niż radiacyjny czas życia, wskazując na to, iż emisja *d-f* jest w tym przypadku wygaszana poprzez relaksację do niżej leżących poziomów w obrębie konfiguracji $4f^3$ bądz też poprzez proces fotojonizacji. Przy wzbudzeniu materiałów światłem o fali krótszej niż 175 nm (odpowiadającej przerwie energetycznej RbCl), emisja *d-f* jest bardzo słaba dla Ce^{3+}, Pr^{3+} oraz Nd^{3+}, a widma luminescencji zdominowane są przez emisję defektów w sieci krystalicznej. Wskazuje to na brak efektywnego przekazania energii pomiędzy matrycą a poziomami *fd* lantanowców wbudowanych w sieć krystaliczną RbCl, co uniemożliwia wykorzystanie chlorku rubidu jako scyntylatora.

Fotoluminescencencja i radioluminescencencja Ce^{3+}, Pr^{3+} i Nd^{3+} w sieciach krystalicznych $SrCl_2$ oraz $BaCl_2$ jest przedstawiona i przeanalizowana w rozdziale czwartym, w odniesieniu do zastosowania tych materiałów jako (szybkich) scyntylatorów. Materiały domieszkowane Ce^{3+} wykazują typową szybką emisję *d-f* ceru (358 nm, 382 nm w przypadku $SrCl_2$ oraz 350 nm i 375 nm w przypadku $BaCl_2$) zarówno przy wzbudzeniu promieniowaniem synchrotronowym, jak i jonizacyjnym. Słaba przewlekła emisja była zaobserwowana. W przypadku Pr^{3+} bardzo szybka emisja *d-f* została zarejestrowana w przypadku $SrCl_2$ (250 nm, 363 nm, 300 nm i 328 nm z czasem życia wynoszącym 13 ns) oraz w przypadku $BaCl_2$ (260 nm, 288 nm i 315 nm z czasem życia wynoszącym 10 ns), jednak jedynie przy wzbudzeniu bezpośrednio w poziomy *fd*. Nie zaobserwowano emisji *d-f* wzbudzając materiały domieszkowane Pr^{3+} używając promieniowania rentgenowskiego. Brak emisji *d-f* wyjaśniony jest brakiem przekazu energii między matrycą a poziomami *fd* prazeodymu, z uwagi na fakt, że emisja matrycy jest przy niższych energiach niż poziomy *fd* Pr^{3+} (230 nm dla $SrCl_2$ oraz 235 nm dla $BaCl_2$). Materiały domiwszkowane neodymem nie wykazywały emisji *d-f*.

W rozdziale piątym własności luminescencyjne bardzo obiecującego luminoforu rentgenowskiego $Lu_3Al_5O_{12}$ (LuAG) domieszkowanego jonami Ce^{3+} zostały opisane. Mimo wielu zalet, materiał ten wykazuje wydajność emisji pod wzbudzeniem promieniowaniem X bądź γ, która jest znacznie poniżej wartości obliczonych. Wpływ współdomieszkowania tego materiału jonami Tb^{3+} została zbadana w celu zwiększenia wydajności luminoforu. Widma wysokorozdzielcze LuAG'u domieszkowanego jedynie

Ce^{3+} lub Tb^{3+} zostały zmierzone i dostarczyły informacji o strukturze energetycznej tych jonów w matrycy LuAG'u. Dla Ce^{3+} linia zerofononowa i struktura wibronowa zostały zaobserwowane dla dwóch najniższych poziomów *5d* oraz wartości przesunięcia stokesowskiego (2350 cm^{-1}) i parametru Huang'a-Rhys'a (*S*=9) zostały policzone. Przejście *4f-5d* dla Tb^{3+} dla stanów wysoko (HS) i nisko spinowego (LS), a także linia zerofononowa i struktura wibronowa dla przejscia HS zostały zarejestrowane. Rozszczepienie pomiedzy HS-LS wynosi 5400 cm^{-1} i jest mniejsze niż zwykle obserowane, co tłumaczone jest zmniejszeniem wartości parametru wymiany *5d-4f* w wyniku dużej kowalencyjności. Przy stopniowym zastępowaniu mniejszego jonu Lu^{3+} większym jonem Tb^{3+} rozszczepienie pola krystalicznego zmniejsza się, powodując przesunięcie najniższego poziomu *5d* poniżej poziomu $^5D_4$ Tb^{3+} co pozwala na wydajny przekaz energii pomiędzy jonami Tb^{3+} i Ce^{3+} nawet w niskich temperaturach. Pomiary czasu życia luminescencji potwierdzają wydajny przekaz energii od Tb^{3+} do Ce^{3+} i dostarczają jakościowej wiedzy o mechanizmie przekazania energii. Współdomieszkowanie materiału Tb^{3+} nie skutkuje jednak w zwiększeniu wydajności materialu i tłumaczone jest udziałem stanów energetycznych defektów w pułapkowaniu elektronów.

W rozdziale szóstym opisana jest zależność pomiędzy radiacyjnym czasem życia emisji a długością fali emisyjnej. Czas życia emisji *d-f* lantanowców podlega tak zwanej Złotej Zasadzie Fermie'ego, gdzie czas życia emisji staje sie krótszy dla zwiększających się energii emisji. Znajomość radiacyjnego czasu życia jest niezwykle istotna w przypadku projektowania nowych materiałów dla określonych zastosowań, takich jak na przykład materiały scyntylacyjne, gdzie emisje o bardzo krótkich czasach życia są konieczne. Z uwagi na fakt, iż nastąpił wzrost zainteresowaniem badaniami nad scyntylatorami opartymi o emisję *d-f* Pr^{3+}, bardzo istotnym jest zarówno z puktu widzenia teorii, jak i zastosowań, by znać radiacyjny czas życia emisji *d-f* Pr^{3+}. Dotychczas nie przeprowadzono analizy ilościowej danych eksperymentalnych, jak i nie przeprowadzono porównania z danymi dotyczącymi radiacyjnego czasu życia emisji *d-f* dla Ce^{3+} oraz Eu^{2+} celem sprawdzenia jak mocna jest zaleznosc (kwadratowa czy sześcienna). Dane eksperymentalne zostały zfitowane używając różnych poprawek pola lokalnego dla zależności kwadratowej oraz sześciennej. Pomimo, iż zależność czasu życia w fukcji długości fali emisyjnej wydaje się być sześcienna ($\tau \propto \lambda^3$), niepewność danych jest nadal znacząca. Także poprawka pola lokalnego dostarcza problemów i nie jest jednoznaczne, który model powinien być stosowany. Niemniej jednak znajomość dokładnej wartości współczynnika załamania światła danego materiału przy długości fali emisyjnej Pr^{3+} w tymże materiale jest niezwykle istotna w celu otrzymania poprawnych rezultatów i wartość ta nie może być wzięta jako stała dla wszystkich matryc, jak to ma miejsce w danych literaturowych. Wiedza na temat dokladnych wartości współczynników załamania światła nie jest szeroko dostępna w literaturze i fakt ten stwarza znaczące problemy w badanej metodzie. Najkrótszy radiacyjny czas życia dla emisji *d-f* Pr^{3+} przy długości fali emisyjnej 220 nm w matrycy o

założonym współczynniku załamania światła wynoszącym 1.8 w oparciu o obliczenia wynosi okolo 6 ns.

Rozdział siódmy przybliża zależność Dorenbos'a. Zależność ta jest empirycznie wyprowadzonym modelem, który koreluje położenie najniższego poziomu *fd* każdego lantanowca z położeniem odpowiadającego mu najniższego poziomu *fd* ceru w tej samej matrycy. Zależność ta jest użyteczna w celu oszacowania położenia poziomów *fd* trójdodatnich jonów lantanowców w dowolnej matrycy, znając położenie maksimum odpowiadającego najniższemu poziomowi *fd* jakiegokolwiek lantanowca. Sprawdzono, czy zależność Dorenbos'a jest także prawdziwa, gdy bierze się pod uwagę linie zerofononowe (ZPL) zamiast położeń maksimów, jak to ma miejsce w tradycyjnej metodzie. Położenia linii zerofononowych wszystkich lantanowców w czterech różnych matrycach (CaF_2, $Y_3Al_5O_{12}$, $LiYF_4$ oraz YPO_4) zostały uzyskane i wartości te zostały użyte jako wkładowe do równania Dorenbos'a. Rezultaty zostały porównane z tymi otrzymanymi używając standardowego podejścia. Otrzymane dane podtrzymują założenie, iż używając położenia linii ZPL można otrzymać wartości dokładniejsze, niż w przypadku użycia położeń maksimów, zwłaszcza w przypadku materiałów posiadających dużą przerwę energetyczną. Związane jest to z faktem, iż położenie linii zerofononowych można określić znacznie dokładniej niż położenie maksimów pasm.

List of publications

This Thesis

"Luminescent salt"; Aleksander Zych, Celso de Mello Donegá, Andries Meijerink; *Journal of Luminescence* **129** (2009) 1535-1537 (Chapter 2)

"Luminescence properties of lanthanide doped alkaline earth chlorides under (V)UV and X-ray excitation", Aleksander Zych, Anke Leferink op Reinink, Koen van der Eerden, Celso de Mello Donegá, Andries Meijerink, *Journal of Alloys and Compounds* **509** (2011) 4445-4451 (Chapter 4)

"Fast *d–f* emission in Ce^{3+}, Pr^{3+} and Nd^{3+} activated RbCl", Aleksander Zych, Celso de Mello Donegá, Andries Meijerink, *Optical Materials* **33** (2011) 347-354 (Chapter 3)

"Luminescence and energy transfer in $Lu_3Al_5O_{12}$ scintillators co-doped with Ce^{3+} and Tb^{3+}", Joanna Gondek, Aleksander Zych, Konstantin Ivanovskikh, Thomas Justel, Cees Ronda, Andries Meijerink, submitted to Physical Review B (Chapter 5)

"Analysis of the radiative lifetime of Pr^{3+} *d-f* emission", Aleksander Zych, Matthijs de Lange, Celso de Mello Donegá, Andries Meijerink, to be submitted (Chapter 6)

"Analysis of the shift of zero-phonon lines for *f-d* luminescence of lanthanides in the relation to the Dorenbos model", Aleksander Zych, Joanna Ogiegło, Cees Ronda, Celso de Mello Donegá, Andries Meijerink, to be submitted (Chapter 7)

Other

"New fabrication procedure of Y_2SiO_5:Ce and its structural and spectroscopic characterization"; Eugeniusz Zych, Aleksander Zych, Jian Zhang, Shiwei Wang; *Journal of Alloys and Compounds* **451** (2008) 286–289

"Luminescence properties of Eu^{3+}:$KGd(WO_4)_2$ nanocrystallites"; R. Pazik, A. Zych, W. Strek; *Materials Chemistry and Physics* **115** (2009) 536-540

"Ultrafast excitation and relaxation dynamics in Pr^{3+} doped $Lu_3(Al,Ga)_5O_{12}$", K. Ivanovskikh, A. Meijerink, A. Zych, C. Ronda, to be submitted

"Luminescence and energy transfer in $Lu_3Al_5O_{12}$ scintillators co-doped with Ce^{3+} and Tm^{3+}", .M. Ogiegło, A. Katelnikovas, A. Zych, T. Juestel, A. Meijerink, C.R. Ronda, to be submitted

"Luminescence and energy transfer in $Lu_3Al_5O_{12}$ scintillators co-doped with Ce^{3+} and Pr^{3+}", J.M. Ogiegło, A. Zych, T. Juestel, A. Meijerink, C.R. Ronda, to be submitted

Dankwoord

I would like to use this opportunity to thank a few people who have contributed to the development of this thesis in one way or another. My acknowledgements go to my mentors, my colleagues and friends at CMI.

First of all, I would like to express my gratitude towards my supervisor and promotor, Professor Andries Meijerink. Thank you for inviting me to join CMI and giving me the opportunity to participate in the exciting work within the STRING project. I appreciate the numerous discussions we had and your valuable time that you have sacrificed in order to conduct them. Also during the endless hours at the Superlumi station, where you were willing to discuss scientific, as well as everyday matters. I have learned a lot from you. I would also like to thank you for all the help you have provided to me and my family during our stay in Utrecht. Your kindness shall never be forgotten. It is also highly appreciated that you have found time to translate the summary of this thesis from English to Dutch. ***Haartelijk dank!***

My thanks also go to Dr Celso de Mello Donegá. Celso, I appreciate your help at the beginning, translating all the documents from Dutch to English and for all your advice. Your insights into luminescence that you have shared with me are appreciated as well. ***Obrigado!***

Professor John Kelly could not be forgotten in this 'dankwoord'. You have provided my family with great support and helped us find housing at the beginning of our Dutch experience. And when there seemed to be no hope of finding any, you even offered the warmness of your own home. We thank you for that. ***Go raibh maith agat!***

I would also like to thank Professor Cees Ronda for very interesting lectures and discussions outside the classroom. Thank you for your advice and tips.

Hans Ligthart and Stephan Zevenhuizen. You have helped a lot during the measurements performed at CMI and with the set-up breakdowns. Hans, your help during moving from one place to another and bringing our furniture from IKEA to our apartment was great. And you never wanted anything in return. Stephan, you always found time to

help out with the computer trouble. Also with my home computers when such help was needed.

I need to acknowledge Dr Gregory Stryganyuk and Dr Aleksei Kotlov for their assistance and prompt problem solving even at latest hours at night at the Superlumi experimental station at HASYLAB, DESY. Without you, none of this could have been made possible. I apologize to you and your wives for waking you up at night and disturbing your weekends during breakdowns. But you were always ready to come and help when things went wrong at DESY. You have also taught me a lot about the synchrotron itself and the methodology of the measurements performed there.

Esther, Joasia, Danusia (thanks for the photo of me on the back of the thesis), Janne, Dawai, Konstantin, Rolf, Rianne, Linda, Bryan, Zhixiang, Yiming, Dominika, Darek, Francesca, Marianna, Heng Yu, Vladimir, Zachar, Wiel, Joren, Mark, Rosa, and all of you I might have forgotten, thank you for all the fun we had over the past four years. With some of you I have become really close and I am proud to call you my friends and not only colleagues. I will miss you.

A kind thank you goes towards Anke, Koen and Matthijs for their contribution to the work presented in my thesis. Anke and Koen have greatly contributed to chapter 4, while Matthijs has done extensive research presented in chapter 6. Also the other students I have worked with and others with whom we had a lot of fun together in the lab and outside of it: Janne-Mieke, Marleen, Sander, Sonja, Bob, Sander (a different one), Suzanne, Matti, Ward, Nico, Nick. The fun during our table soccer games was great and this is one of those things that I will miss a lot.

Special kind of thank you goes to my family. To my Parents for having me. To my Sister for coping with me when we were younger. Special kind of thank you to my Father for introducing me to the field of chemistry and the exciting world of lanthanide luminescence.

Last but not least, I want to thank my Wife, Justynka, for accepting the proposal and being with me through good and bad times. For all the encouragement You have given me and the support not only in the scientific matters. And our firstborn, our lovely Daughter Ania, who besides the sleepless nights gave us a lot of happiness and who brought a smile to our faces every day. We love to watch you grow and we love you. **Dziękuję.**

Curriculum Vitae

The author of this thesis was born on March 13th 1983 in Wroclaw, Poland. Between 1998 and 2002 he attended the Aleksander Fredro High School in Wrocław Poland, where he obtained his maturity diploma in 2002. The same year he started his studies in the University of Wrocław at the Faculty of Chemistry with the specialization Computer Aided Chemistry. In his final year of studies in 2007 he performed his Masters research in the Department of Spectroscopy of Excited States in the Institute of Low Temperature and Structure Research of the Polish Academy of Sciences in Wrocław, Poland, under the supervision of Professor Wiesław Stręk. He graduated in 2007 from the University of Wrocław with the mark "very good" (5.0 in a 2.0-5.0 scale).

After the completion of his studies at the University of Wrocław, the author got married to Justyna Kozak-Zych in August 2007 and left Poland to start his PhD research at the Utrecht University in the Faculty of Science in the group Condensed Matter and Interfaces (CMI), under the supervision of Professor Andries Meijerink and Dr Celso de Mello Donegá. During the course of the PhD studies the author has performed teaching duties within the Analytical Chemistry course for two years, teaching the 1st year students and supervising their research projects for two years at CMI. He also supervised two Bachelor students and three Master students in the course of their projects.

During the PhD research the author attended numerous international conferences and workshops, where he presented results of his research in the form of posters and oral presentations. The international meetings included Physics@FOM symposia in Veldhoven, The Netherlands (2008-2011), Debye Spring School and the DO!-days (2008-2010), International Conference on Luminescence 2008 (ICL '08) in Lyon, France, where the author received a prize for best poster presentation, 7th International Conference on Luminescent Detectors and Transformers of Ionizing Radiation 2009 (LUMDETR 2009) in Kraków, Poland, Excited States of Transition Elements and Workshop on Luminescence 2010 (ESTE 2010) in Piechowice-Wrocław, Poland and the Materials Research Society (MRS) Spring Meeting 2011 in San Francisco, United States.

In 2008 the author served in the Debye AIO Committee (DAC), where in 2009 he became the secretary of DAC. During his participation in the Committee he has organized the "Debye Sports Day and BBQ" in 2010. In 2011 he has been a co-editor of the "Debye Postgraduate Research Projects" booklet.

During the PhD, the author became a proud father to a Daughter, Anna Else Zych, who was born on 18th March 2010 in Woerden, The Netherlands. As of September 2011 Justyna, Ania and Alek are awaiting a new member of the family.